Graduate School of the

SCHOOL OF OCEAN AND EARTH SCIENCE

UNIVERSITY OF SOUTHAMPTON

SOUTHAMPTON OCEANOGRAPHY CENTRE

TEMPORAL VARIABILITY OF THE GRAVITATIONAL CIRCULATION IN A PARTIALLY MIXED ESTUARY

CESAR HENRIQUE DE ASSIS RIBEIRO

OCTOBER 2004

Graduate School of the

School of Ocean and Earth Science

This PhD dissertation by

Cesar Henrique de Assis Ribeiro

has been produced under the supervision of the following persons

Supervisor

Dr. Jonathan Sharples

Chair of Advisory Panel

Prof. Peter Killworth

Member of Advisory Panel

Prof. Carl Amos

Declaration

This thesis is the result of work done wholly while under registered postgraduate candidature.

Abstract

The ecology of estuarine systems depends on the water exchange with the coastal region, and net mean, non-tidal, circulation driven by the longitudinal density gradient plays an important role in this exchange. This project investigated the responses of the gravitational flow to changes in vertical mixing on different time-scales. Three long term deployments of seabed-mounted Acoustic Doppler Current Meter and surface and seabed salinity-temperature loggers collected current profiles and surface and bottom density time series for a total of 268 days, between March 2001 and April 2002. Additionally, a vertical 1-D numerical model with a turbulence closure scheme was used to provide further insight into the mixing effects on the gravitational circulation. Analysis of the tidally averaged velocities suggested that the spring-neap fluctuation of the tidal mixing modulates the gravitational circulation. Mean velocities increased to 0.05 $\mathrm{m\,s^{-1}}$ at the bottom and 0.07 $\mathrm{m\,s^{-1}}$ at the surface during a typical weak neap tide. A critical bottom current of 0.4 $\mathrm{m\,s^{-1}}$ was found for the typical longitudinal density gradient of 2.5×10^{-4} $\mathrm{kg\,m^{-4}}$, above which tidal mixing appeared to prevent this increased gravitational flow. This observed critical velocity agreed with the Hansen-Rattray solution for Southampton Water. Results also suggested that for weaker/stronger density gradients the critical velocity is lower/higher. Intra- and inter-annual fluctuations of precipitation also affect the gravitational flow by altering the longitudinal density gradient. No clear evidence of a modulation of the gravitational circulation on semi-diurnal time scales was found, although the mean flow did vary within a tidal cycle. The harmonic method may have removed possible semi-diurnal signal present on the gravitational ciirculation time series. It seems that the full development of a gravitational flow takes longer (1-2 days) than the semi-diurnal variability of the tidal mixing. Although inclconcusively, it seems that barotropic mechanisms do not control gravitational circulation in Southampton Water, contrarily to San Francisco Bay (Stacey et al., 2001). This may be caused by the weaker tidal straning and stronger longitudinal density gradient found in Southampton Water. Wind speed, direction and persistence all seemed to affect the gravitational flow. Onshore wind speed of 8 $\mathrm{m\,s^{-1}}$ was found to be sufficient to prevent the neap tide pulse of gravitational flow. Besides the surface stress, onshore winds can cause mixing by inducing vertical instability. Offshore winds aid seaward flow of the surface component of the gravitational circulation. No significant effects of transversal winds on the density-driven flow were found, probably due to the limited fetch. Data showed that local winds stress can not explain significant changes on the barotropic balance. However, it seems that sea surface and slope variability, driven by remote wind or by atmospheric pressure variation, can rapidly alter the density-driven flow by introducing a barotropic gradient into the balance of forces. Numerical simulation reproduced the spring-neap modulation of the gravitational circulation and agreed with the critical near-bed tidal velocity observed, although a weak signal of the gravitational flow persisted as a background value. the Model overestimated the observed gravitational velocities and significantly underestimated stratification, suggesting that turbulence closure scheme possibly does not work well in shallow partially mixed estuaries. Generally, the effects of different speed and direction of the wind on the gravitational flow were well reproduced by the model. The observed modulation of the net flow controls the time scales of the transport of nutrients, organisms, sediments and pollutants through the water into and out of the estuary, which is important for studies on estuarine ecology and environmental management and also for policy makers concerning estuary areas.

to Vitor
born in the Princess Anne Hospital on 24 November 2003

NAE MAN CAN TETHER TIME OR TIDE
Robert Burns, from Tam O'Shanter

VALE O QUE ESTÁ ESCRITO
The unexpressed is worthless
Barão de Drummond (free translation)

Acknowledgments

To the Conselho Nacional de Desenvolvimento Científico e Tecnólogico - CNPq (proc. no. 200817/98-1 GDE).

To the Natural Environment Research Council - NERC (grant no. GR3/12736).

To Andy Roberts and Bethan Davies from the Hampshire & Isle of Wight Area Office of The Environmental Agency, for the River Test flow data.

To William Heaps from the Association of British Ports (ABP), for the tide data sets of two tidal gauges in Southampton Water.

To the crew of *R.V. Bill Conway* and *Prince II*. SOES staff Graham Etheridge, Bob Wilkie, Gary Fisher, Stephen Hayward, Gramme Leggatt, Mike Crowford (*in memorium*), Ray Collins, Dave Spanner + the wonderful team of volunteers Ana Paula Teles, Sinhué 'Pèrron' Torres, Susanne Ufferman, Juan Larasoaña, Steffen 'Passa a bola viado!' Dransfeld, Oliver Ross, Judith Homewood, Uli 'Daba' Riemenschneider, Dave Lambkin, Dan Mayor, David Goldsmith, Andy Taylor + Jenny Mallison and the SOC dive group, for their invaluable support during the fieldwork.

To Erik Muxagata and Sinhué Torres, for the salinity sampling kindly taken during their surveys in the Southampton Water.

To Chico, Gil, Milton, Martinho, Marisa, Cássia, Carlinhos, Caetano, Gonzagão, Gonzaguinha, Aragão, Pixinguinha, Tom, Djavan, Zeca, Zelia, Alceu, Melodia, Lenine, Beth, Rappa, Farofa, Paralamas and many others, for some of the sweetest Brazilian fragments to my ears now and then.

To the wonderful mates in the 564/12 (Olli, James, Deb and Pascale) + the step-families Bastos, Pezzi, Caltabiano, Maggioni, Souza, Fache-Teles and Lucato + my dearest Patrícios + la Mafia Italiana + Laura + the volleyball gang + the ludic backgammon fellows + everyone else who shared their heart, for the finest moments in the UK.

To Peter Killworth and Carl Amos, for the fruitful advisory panel meetings.

To Joanna Waniek, for sharing the hard work before, during and after the field trips. Nine paces to the left.

To Jonathan Sharples, for his uncountable hours of patience and supporting, from English language and culture to astrophysics and British history, but mainly coastal physical oceanography. Nine paces to the right.

And special thanks to Silvia, for her unconditional love.

Contents

List of Figures

List of Tables

Chapter 1

Introduction

Estuaries are fragile systems at the land-sea boundary where the fluxes of fresh and salt water control a large number of biogeochemical and ecological processes. The ecosystem of any tidally controlled estuary strongly depends on the exchange of water with the adjacent coastal region, which regulates fluxes of organisms, nutrients, sediments and pollutants in and out of the estuary. Although the tide generally governs those fluxes on the flood and ebb time scales, it is the long-term residual circulation which determines the net fluxes.

Residual circulation in an estuary generally has a density-driven component as consequence of the density difference between the saltier denser and the fresher less dense waters. This circulation is characterised as a two-layer, bi-directional flow, the gravitational circulation, with the denser salt water flowing landward underneath the less dense water moving to the sea.

Hansen and Rattray (1965) suggested that the strength of the gravitational circulation is given by the balance between forces of the horizontal pressure density gradient (set up by the density gradient) and the vertical mixing (which acts to vertically re-distribute the momentum of the gravitational flow). Considering that the friction generated by tidal currents is a strong source of vertical mixing, the time variability of the tidal mixing may cause a modulation on the mean flow and, consequently, on the net fluxes in and out of the estuary. It is this potential for time-dependent rates of gravitational circulation in response to varying mixing that is the subject of this thesis.

1.1 The structure of the thesis

This chapter presents an introduction to the physical processes which control the gravitational circulation in an estuary, with related theoretical and laboratory work and relevant examples. The objectives of this study are presented at the end of this chapter. Chapter 2 describes Southampton Water as an ideal location for this study. The sampling strategy of the fieldwork and general methods applied to the data analysis are also presented. Chapters 3 and 4 focus on the field observations, describing specific methods and the results of the analysis of the spring-neap and semi-diurnal modulation of the non-tidal circulation, respectively. The description of a simple numerical model and the results from the experiments with the model are presented in chapter 5. Final conclusions and suggestions for further works are listed in chapter 6.

1.2 Gravitational circulation in estuaries

In contrast to the ocean or lakes, where stratification over large horizontal scales is driven by the approximately uniformly distributed solar heating, in estuaries the dominant buoyancy source is the localised input of a less dense freshwater at the mouth of the river. Therefore estuaries are distinguished by not only vertical but also strong longitudinal density gradients. Since the pioneering works of Donald Pritchard in the Chesapeake Bay, U.S.A. (e. g., Pritchard, 1952, 1956, 1958) the physical processes involved in the dilution of the incoming freshwater into the surrounding denser seawater have been the subject of extensive studies.

Gravitational relaxation of the longitudinal density gradient drives a two-layer circulation, with the lower density water flowing seaward on the top of the denser water, which flows into the estuary at the bottom. This circulation is normally called gravitational, estuarine or baroclinic circulation and is an important source of stratification in estuaries.

A diagram of the two-fluid, lock-exchange, experiment in a tank illustrates the formation of the gravitational circulation caused by a longitudinal density gradient (Fig. 1.1). The initial position of the experiment is with a volume of denser water (ρ_1) separated by a vertical barrier from another volume of less dense water (ρ_2), setting up a strong longitudinal density gradient but with vertically homogeneous compartments (Fig. 1.1a). As soon as the barrier is removed the system becomes gravitationally unstable. To reach a new stable condition the denser water flows to the right hand side of the diagram at the bottom of the tank while its centre of gravity migrates down to a deeper position. Meanwhile an increase on the surface level on the right hand side of the tank is caused by this bottom gravity flow, inducing an inclination of the surface of the tank down towards the left hand side. This surface slope ultimately induces the less dense water to flow above the denser water toward the opposite direction, forming the bi-directional pattern of the gravitational circulation and creating stratification (Fig. 1.1b). Thus the system has reduced its potential energy to the lowest available and sharpened the vertical density gradient. In the absence of any other process, any longitudinal density gradient will undergo this.

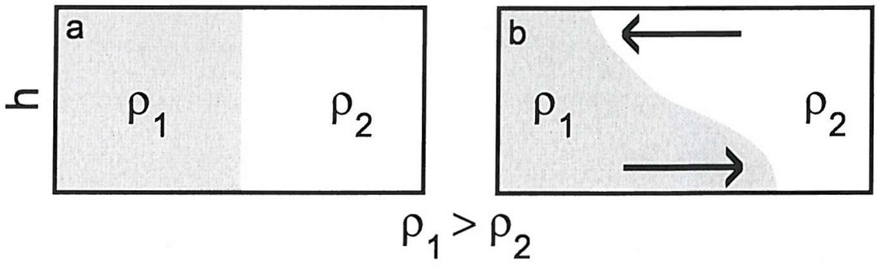

Figure 1.1: **Transition from (a) an initially vertically mixed but unstable longitudinal density gradient to (b) a more stable position. The relaxation of the density gradient induces stratification and gravitational circulation.**

Although this bi-directional pattern of the longitudinal circulation is a typical characteristic of the gravitational circulation in estuaries, some other factors can also drive this shear flow (e.g. wind-driven flow).

1.2.1 The Hansen-Rattray profile

Turbulent mixing acts vertically re-distributing momentum by transferring it from the surface and bottom boundaries, where friction is greater, towards the inner parts of the water column, thereby reducing total shear. The link between the gravitational circulation and turbulent mixing was firstly inferred by Hansen and Rattray (1965) in their classic steady-state solution for the vertical profile of the velocity produced by the longitudinal density gradient. This solution can be detailed following the derivation described by Officer (1976) (p. 116-121) and Lewis (1997) (p. 65-68). Assuming steady-state flow and constant atmospheric pressure, and neglecting lateral friction and the advective term, the depth-dependent equation of motion balances the generation of turbulence by the action of the vertical shear with the horizontal pressure gradient. Considering only the x-direction of the vertical section through the main axis of an estuary (Fig. 1.2) the equation of motion can be formulated as

$$\rho N_z \frac{d^2u}{dz^2} = -\rho g \frac{\partial \zeta}{\partial x} + g \frac{\partial \rho}{\partial x} z \qquad [\mathrm{N\ m^{-3}}] \tag{1.1}$$

where ρ is the density ($\mathrm{kg\,m^{-3}}$), g is the gravitational acceleration ($\mathrm{m\,s^{-2}}$), ζ is the non-tidal surface height (m), N_z is the vertical eddy viscosity coefficient ($\mathrm{m^2\,s^{-1}}$) and u is the x-axis velocity ($\mathrm{m\,s^{-1}}$). The longitudinal pressure gradient is the sum of the barotropic surface slope ($\partial\zeta/\partial x$) and the baroclinic density gradient ($\partial\rho/\partial x$).

Equation 1.1 can be solved for $u(z)$ as

$$u_{(z)} = \frac{1}{2}\frac{g}{N_z}\frac{\partial \zeta}{\partial x} z^2 + \frac{1}{6}\frac{g}{\rho N_z}\frac{\partial \rho}{\partial x} z^3 + C_1 z + C_2 \qquad [\mathrm{m\ s^{-1}}] \tag{1.2}$$

where C_1 and C_2 are constants. By assuming the boundary conditions as no wind stress at the surface ($du/dz = 0$ at $z = 0$) and no current at the bottom (u=0 at $z = h$) equation 1.2 can be written as

$$u_{(z)} = -\frac{1}{2}\frac{g}{N_z}\frac{\partial \zeta}{\partial x}(h^2 - z^2) + \frac{1}{6}\frac{g}{\rho N_z}(h^3 - z^3)\frac{\partial \rho}{\partial x} \qquad [\mathrm{m\ s^{-1}}] \tag{1.3}$$

A relation between the surface slope and the longitudinal density gradient can be found by expressing the continuity equation for the flow as

$$R = \int_0^h u_{(z)}\, dz = \frac{1}{3}\frac{g}{N_z}\frac{\partial \zeta}{\partial x} h^3 - \frac{1}{8}\frac{g\lambda}{\rho N_z} h^4 \qquad [\mathrm{m\ s^{-1}}] \tag{1.4}$$

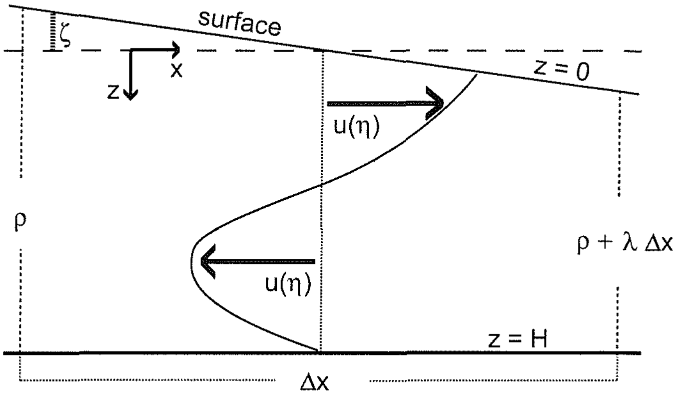

Figure 1.2: **Schematic representation of the vertical profile of the main axis velocity $u(\eta)$, for η being the normalised depth z/h, showing the longitudinal density gradient $\Delta\rho/\Delta x$ and the surface elevation ζ. Modified from Lewis (1997), Fig. 3.4.**

where R is the river flow passing through a section across the estuary and λ is the longitudinal density gradient $\partial\rho/\partial x$ (kg m^{-4}).

Taking a typical river discharge of 16 m^3 s^{-1} (Fig. 2.10 for the river discharge dataset) divided by a cross sectional area of the order of 10^4 m^2, the resulting flow associated with the river input is of the order of 10^{-3} m s^{-1}. This is one to two orders of magnitude less than the gravitational flow calculated in this study (sections 3.2 and 4.2).

Thus the river flow can be neglected and the surface slope can be described in terms of the longitudinal density gradient by rearranging equation 1.4 as

$$\frac{\partial\zeta}{\partial x} = \frac{3}{8}\frac{h}{\rho}\lambda \tag{1.5}$$

It is worth noting that the equilibrium between the barotropic gradient caused by the non-tidal surface slope, $\partial\zeta/\partial$x, and the baroclinic gradient induced by the longitudinal density gradient, λ, is reached for Southampton Water at a ratio of

$$\frac{\partial\zeta}{\partial x} = 0.0052\lambda \tag{1.6}$$

for an averaged depth of 15 metres in the main navigation channel. For example, the barotropic forcing generated by a surface slope of 0.05 metres along the 10 km length of Southampton Water would be able to couterbalance a gravitational circulation driven by a longitudinal density gradient equal to 10^{-3} kg m^{-4}.

Substituting equation 1.5 into equation 1.3, and making $\eta = z/h$, the formulation for the velocity profile can be written as

$$u_{(\eta)} = \frac{1}{48}\frac{g\lambda h^3}{\rho N_z}(8\eta^3 - 9\eta^2 + 1) \qquad [\mathrm{m\,s^{-1}}] \tag{1.7}$$

where $u_{(\eta)}$ is the vertical profile of the flow parallel to the longitudinal density gradient λ. Alternatively, by applying a frictionless condition at the bottom boundary (du/dz=0 at $z = h$) in equation 1.2, the relation between the surface slope and the longitudinal density gradient becomes

$$\frac{\partial\zeta}{\partial x} = \frac{1}{2}\frac{h}{\rho}\lambda \tag{1.8}$$

and the velocity profile for the depth η is

$$u_{(\eta)} = \frac{1}{24}\frac{g\lambda h^3}{\rho N_z}(4\eta^3 - 6\eta^2 + 1) \qquad [\mathrm{m\,s^{-1}}] \tag{1.9}$$

Equations 1.5 and 1.8 state that the difference between the non-slip and the frictionless bottom boundary conditions is simply the fraction on the right-hand side of both equations, which is the surface slope coefficient γ. It implies that the zero net flow balance between the longitudinal density gradient and surface slope is held with $\gamma = 3/8$ for non-slip bottom condition and $\gamma = 1/2$ for frictionless bottom condition. Results of both the zero bottom velocity and the zero bottom stress conditions show the characteristic bi-directional velocity profile of the gravitational circulation as a result of the longitudinal density gradient λ (Fig. 1.3).

1.3 Tidal straining

Tidal straining is a stratifying process caused by the difference in the vertical advective field between flood and ebb tides. During the ebb, bed friction causes the near-bed water to flow seaward slower than the near-surface water. Thus surface water

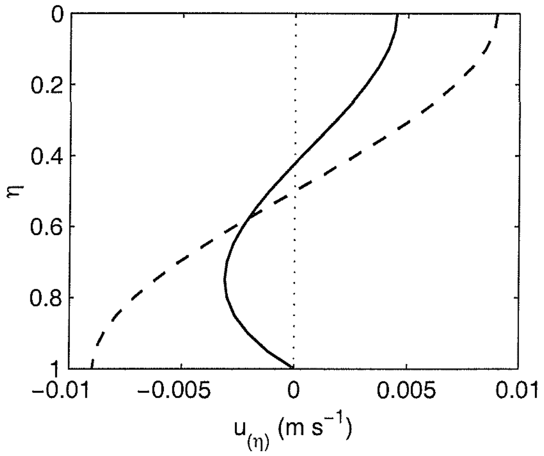

Figure 1.3: **Vertical velocity profile of the density-driven flow in a estuary for a non-slip (bold line) and frictionless (dashed line) bottom boundary condition, calculated from equations 1.7 and 1.9 for $h = 15$ metres, $\lambda = 2 \times 10^{-4}$ kg m^{-4} and $N_z = 0.03$ m^{2}s^{-1}. η is the non-dimensional depth z/h.**

of gradually lower density from further up the estuary is pulled on top of the slower-moving bottom water, creating a vertical density gradient (Fig. 1.4). The reverse process occurs during the flood, with the denser seawater being pushed up the estuary faster at the surface, removing the stratification induced on the ebb and then allowing convective overturning. This semi-diurnal strain-induced periodic stratification was observed by Simpson et al. (1990) in Liverpool Bay, with maximum stratification at the end of the ebb followed by fully mixed water column before the end of the flood, except at neap tide when lower tidal mixing allows a more permanent stratification.

This mechanism of semi-diurnal, strain-induced, stratification led to the concept of tidal asymmetry generating residual currents suggested by Jay (1991). This asymmetry is created through the superimposition of a baroclinic velocity profile on the barotropic tides. The density-driven flow acts in the same direction as the ebb tide but in oppposite direction on the flood, causing a stronger seaward residual current at ebb tides.

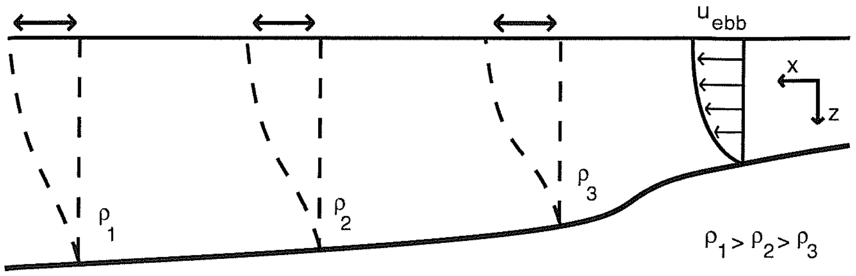

Figure 1.4: **Schematic representation of the stratification induced by the tidal straining. The dashed profiles illustrate the vertical density gradient in both the high (straight line) and the low water (curve). The total stratification at low water (thick arrows) develops as a consequence of bed friction slowing the near-bed current, relative to the surface current, during the ebb tide. The horizontal displacement of the isopycnal (thick arrows) on the surface is caused by the ebb current u_{ebb} moving faster the less dense water on the top of the bottom denser water. The flood current reverses the process.**

1.4 Sources of mixing in estuaries

Mixing in estuarine water can be generally induced by two main mechanisms: friction at the boundary interfaces and internal fluid instabilities. Boundary mixing is driven by the tidal current friction at the bottom of the estuary and by the wind stress at the sea-air interface. This boundary friction produces turbulent motion due to the small-scale velocity shear. The resulting vertical mixing is related to the intensity of the dissipation of the turbulence generated by this boundary shear.

Internal mixing processes, such as internal waves or current shear instability, are caused by instabilities at the interface between layers of the fluid. The relative contribution of boundary and internal processes to the mixing may vary according to the degree of stratification in the estuary. Under weak stratification the boundary generated turbulence should dominate the mixing process, while under strongly stratified conditions the internal source of mixing should be more important (New and Dyer, 1988).

1.4.1 Reynolds stress and eddy viscosity

Turbulence is characterised by a three dimensional, rotational, highly irregular and unpredictable motion. Assuming equilibrium in the production-dissipation process, all the produced turbulent energy is dissipated locally by the smaller eddies. This enables estimation of the total amount of energy expended in the mixing due to the dissipation process by quantifying the production of the turbulent kinetic energy.

The chaotic pattern of turbulent motion makes deterministic analyses impossible and indirect measurements on the nature of turbulence have been possible with the free-falling probes for micro-scale measurements of shear velocity (Dewey et al., 1987, Simpson et al., 1996, Burchard et al., 2002, Fisher et al., 2002) and more recently with profiling casts of micro-structure temperature (MacIntyre et al., 1999, Sharples et al., 2001).

By taking the descriptions of the turbulence by Officer (1976) and Pedlosky (1987), turbulence is represented by Reynolds decomposition indicating the instantaneous fluctuations of velocity or scalars. Considering only the x-component of velocity, u,

$$u = \langle u \rangle + u' \qquad [\mathrm{m\,s^{-1}}] \tag{1.10}$$

$\langle u \rangle$ is the large-scale velocity and u' is its turbulent fluctuation. The small-scale fluctuation of the x-axis velocity, u', acts in three different axes generating turbulent stresses in one normal and two tangential directions. The normal stress is the pressure caused by u' in the x-direction ($\rho\overline{u'^2}$) and the tangential stresses act in the y- and z-direction, respectively $\rho\overline{u'v'}$ and $\rho\overline{u'w'}$. These stresses are called the Reynolds stress, σ, and can be written in the general form of

$$\sigma_{ji} = -\rho\overline{u_i'u_j'} \qquad [\mathrm{N\,m^{-2}}] \tag{1.11}$$

for the i-direction stress acting in the j-direction.

Net transport of momentum is generated by any imbalance in these stresses between two points in the water column. The total turbulent force in the x-direction, F_{Tx}, due to the three-dimensional gradients of the Reynolds stress is

$$F_{Tx} = -\frac{\partial \sigma_{xx}}{\partial x} - \frac{\partial \sigma_{yx}}{\partial y} - \frac{\partial \sigma_{zx}}{\partial z} \qquad [\mathrm{N}] \tag{1.12}$$

These turbulent fluctuations in velocity are very difficult to measure, so an alternative description of the stress force is based on the macro-scale properties of the flow:

$$\frac{\sigma_{ji}}{\rho} = N_j \frac{\partial u_i}{\partial x_j} \qquad [\mathrm{m\,s^{-1}}] \tag{1.13}$$

where the coefficient of eddy viscosity, N_j ($\mathrm{m^2\,s^{-1}}$), represents the parameterisation of the Reynolds stress in terms of a much more treatable large-scale velocity, u_i.

The coefficient of vertical eddy viscosity, N_z, quantifies the vertical transfer of momentum in a turbulent flow.

1.4.2 Boundary mixing

Interactions between the water in motion and the boundaries are an important source of turbulent mixing in estuaries. Gradients of velocity are present in both the sea-bed and sea-air interfaces, and are related to the current friction at both the bottom and wind stress in the surface, respectively.

Tidal mixing

Tidal currents affect the fluid stability through the friction produced by water flowing over a static bed. Velocity has to be zero at the closest point to the bed, inducing a logarithmical profile of velocity near the bottom. This shear generates turbulent motion. The rate of production of kinetic turbulent energy associated with the bottom friction is proportional to the bottom velocity to the cubic power and the strength of the mixing may extend through the whole water column in shallow estuaries with strong tidal currents (Lewis, 1997).

Tidal modulation of the stratification has been associated with the variation of the tidal-induced mixing in partially mixed estuaries (Geyer and Smith, 1987, Sharples et al., 1994, Nepf and Geyer, 1996) and regions of freshwater influence - ROFI (Simpson et al., 1990, Sharples and Simpson, 1995). Experiments done in the Hudson River estuary have yielded a comprehensive picture of the effects of tidal mixing in estuarine dynamics (Peters, 1997, 1999, Peters and Bokhorst, 2000). There the temporal variability of the turbulent mixing generated by the bottom friction was observed in detail through both spring-neap and semi-diurnal tidal cycles. The main findings were: (1) the strong relation between the local bottom-generated turbulence and stratification; and (2) the effect of stable conditions in suppressing vertical mixing.

Similar results were also shown by Stacey et al. (1999) in their observational and modelling study of the tidal fluctuation of the bottom-induced turbulent mixing in the San Francisco Bay. Zhou (1998) associated the modulation of a bottom gravity current flowing into the estuary with fluctuations of the tidal mixing by using both analytical and numerical solutions. Stronger mean flows were related to more stable stratification during periods of lower bottom friction. Stacey et al. (2001) observed that the strength of the tidal straining mechanism is important in determining whether the ebb-flood asymmetry of the stratification affects vertical mixing.

Wind mixing

The effect of the wind acting on the surface waters is analogous to the logarithmic profile of the velocity shear in the bottom boundary. Values of the wind-induced current can vary from 1 to 4 % of the wind speed (Lewis, 1997) in a thin layer immediately below the surface, and decaying logarithmically towards greater depth. Wind can also locally generate a fetch-dependent wave field, which may enhance turbulent motion downward from the surface and contribute to the overall vertical mixing.

The effects of mixing generated by wind stress on the stratification have been observed in different systems, such as Spencer Gulf (Nunes and Lennon, 1987), Volkerak estuary (Kreeke and Robaczewska, 1989), the Rhine ROFI (Simpson et al., 1993) and Liverpool Bay (Sharples and Simpson, 1995). Simpson et al. (1993) observed that the addition of the wind stress at the surface reinforced the reduction of the stratification caused by the bottom tidal stirring in the Rhine ROFI. However wind can at the same time induce two opposing processes as observed by (Kreeke and Robaczewska, 1989). By increasing vertical mixing wind works to reduce stratification. In addition to the direct effect of wind-driven mixing, the wind-driven surface current can itself affect stratification, depending on the wind direction. Thus the resulting stratification will depend on the wind characteristics (intensity, direction and persistence) as well as on the tidal state in both the semi-diurnal and spring-neap cycles. The direction of the wind in relation to the coast can also affect stratification by locally inducing upwelling or downwelling (Munchow and Garvine, 1993).

1.4.3 Internal mixing

The presence and persistence of some internal hydraulic phenomena may produce mixing and therefore alter the vertical water column structure. Internal mixing promotes the vertical transfer of mass and momentum and is driven by the some disturbance on the vertical structure of density or velocity. The two different processes that can carry out internal mixing are instabilities at the density interface generated by the velocity shear, called *shear instability*, and the breaking of the internal waves generated by stratification and flow interactions with the bathymetry. As a ratio between the stratification and the current shear, the dimensionless gradient Richardson number, Ri, can be used as an indicator of which internal mixing processes may dominate. Ri is formulated as

$$Ri = \frac{N^2}{S^2} \tag{1.14}$$

where the buoyancy frequency, N (s^{-1}), describes the maximum frequency of oscillation of the pycnocline and is written as

$$N = \sqrt{-\frac{g}{\rho}\frac{\partial \rho}{\partial z}} \qquad [\mathrm{s}^{-1}] \tag{1.15}$$

and the vertical shear, S^2 (s^{-2}), for the main axis is

$$S^2 = \left(\frac{\partial \bar{U}}{\partial z}\right)^2 \qquad [\mathrm{s}^{-2}] \tag{1.16}$$

where g ($\mathrm{m\,s^{-2}}$) is the gravitational acceleration, ρ ($\mathrm{kg\,m^{-3}}$) the density of the water, z (m) the depth and U ($\mathrm{m\,s^{-1}}$) the x-axis current speed. The critical value of $Ri = 0.25$ has been used as a stability threshold for internal mixing mechanisms (Baines and

Mitsudera, 1994). Mixing by internal wave breaking is more likely in well-stratified flows for Ri higher than 0.25, while instability produced by the vertical shear is better achieved in relatively weaker stratified conditions. These internal mixing mechanisms have been observed in the ocean thermocline (Wang and Müller, 2002, St.Laurent and Garrett, 2002), and less extensively in tidally-dominated coastal waters (New, 1988, Largier, 1994, Sharples et al., 2001) and estuaries (Stigebrandt, 1976, New et al., 1986, Nunes and Lennon, 1987, Geyer and Smith, 1987), and can be an important mixing mechanism in partially mixed estuaries (Bourgault and Kelley, 2003). The challenge in the numerical modelling of internal waves and mixing in estuaries lies in the difficulty of scaling the mixing at the pycnocline and parameterising the turbulence generated by internal processes.

Shear instability

Shear induced instability in a stable fluid develops at the interface between different density layers, due to the relative movement between them. A local intensification of shear can be expected during early stages of the ebb or flood, just after slack waters. The increase in shear at these tidal stages drives interfacial instability. If the stratification is not strong enough to suppress it, these instabilities can grow and create two-dimensional billows, known as Kelvin-Helmholtz instability.

Mixing by entrainment, following the formation of the billows by shear instability, has been observed by laboratory experiment (Thorpe, 1973, Koop and Browand, 1979). This entrainment thickens the interface, dissipates the turbulent kinetic energy contained in the eddies, and establishes a weaker vertical stability with a density gradient smoother than the original vertical density gradient (Fig. 1.5).

Shear instability can be created by any perturbation which leads to an increase of the shear in the flow. Goodrich et al. (1987) observed that the relaxation of a surface slope driven by longitudinal wind in Chesapeake Bay can induce shear across the pycnocline and generate internal mixing. This process is likely only if relatively weak stratification keeps a low Ri.

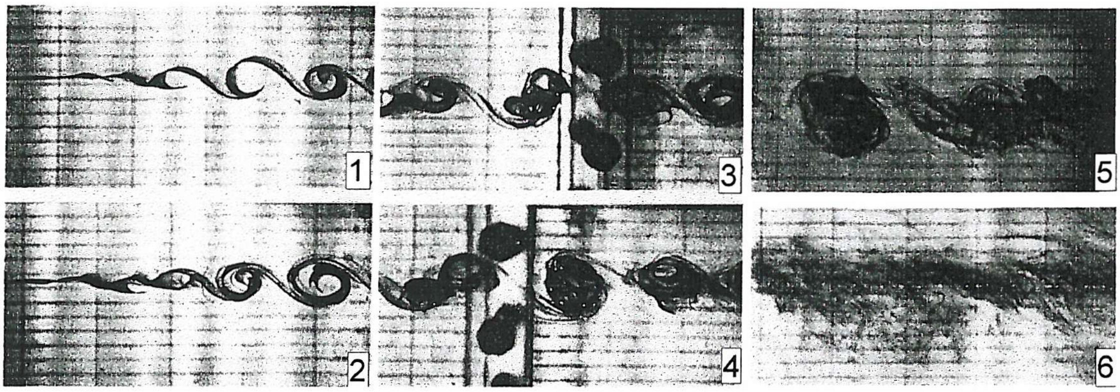

Figure 1.5: **Sequence of photos from a laboratory experiment showing shear instability development and the final weakening of the vertical density gradient. Reproduced from Koop and Browand (1979), Figure 6.**

Internal waves

Internal waves in estuaries are often produced by the interaction of stratified flow with topography, such as steps and shoals, and variations in the estuary width, with gravity providing the restoring force to the vertically displaced fluid (Farmer and Smith, 1980). A sequence of the basic mechanisms of formation and propagation of internal waves in estuaries was described in modelling experiments by Maxworthy (1979). Strong currents over a topographic feature can produce perturbations in the density field. These perturbations can propagate upstream and evolve as internal waves. Instabilities on the wave propagation, caused by an increase in the surrounding currents (Dyer, 1988), or by interaction with physical obstacles, such as the bed of the estuary (Stigebrandt, 1976) or the pillars of a bridge (New et al., 1987), can induce breaking of the waves and produce internal mixing.

Dyer (1988) showed, by high frequency echo sounding, a sequence of internal waves at the upper end of Southampton Water travelling upstream towards the River Test. The perturbation on the pycnocline was formed by the strong ebb tide flowing over a steep shelf where the depth changes from 15 to 2 metres (Fig. 1.6a). As the ebb currents decreased, the train of waves travelled upstream (Fig. 1.6b), and broke in the shallow water causing vertical mixing half a kilometre from the sill (Fig. 1.6c). Bourgault and

Kelley (2003) observed the lateral propagation of internal waves in St. Lawrence estuary, suggesting that the mixing induced by the breaking of the packet of internal waves may account for a significant part of the mixing averaged over a tidal cycle in wide, partially mixed, estuaries.

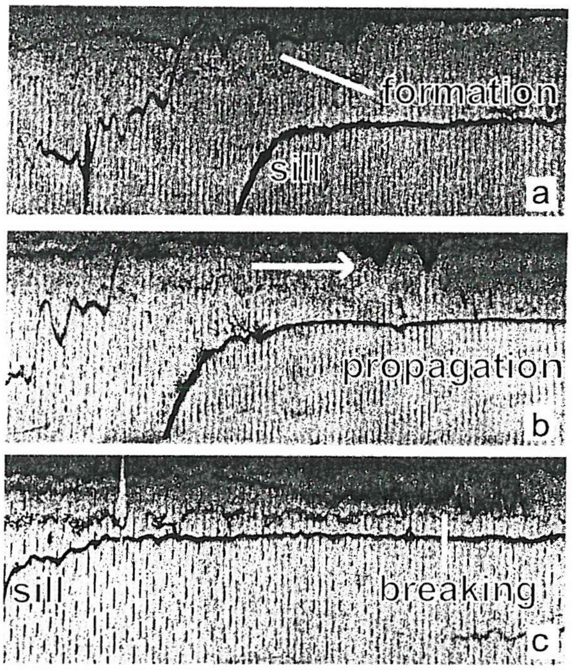

Figure 1.6: **Sequence of 1.2 MHz echo soundings showing (a) formation, (b) propagation and (c) breaking of a train of internal waves associated with a steep sill in the estuary bed. Modified from Dyer (1988), Figure 7.**

1.5 Interactions between gravitational circulation and mixing

Mixing and buoyancy processes occur simultaneously in estuaries, and the competition between the stratifying and the mixing processes determines the density structure of the water column. Nunes-Vaz et al. (1989) described a number of these mechanisms which can be present in estuaries.

A simple way to visualise the dependence of the gravitational circulation on the intensity of the turbulent mixing can be seen by noting the role of N_z in the Hansen-Rattray solution. Equations 1.7 and 1.9 describe the control of the vertical profile of the density-driven velocity, $u_{(\eta)}$, as inversely dependent on vertical mixing, expressed by N_z. Although some limitations on the Hansen-Rattray profile cannot be dismissed, such as the constant N_z through the whole water column and during the tidal cycle, results from those simple equations clearly show the role of the vertical turbulent mixing in controlling the gravitational circulation (Fig. 1.7). Thus, as well as directly eroding stratification, increased mixing could also inhibit the development of stratification by diminishing the strength of the stratifying gravitational circulation.

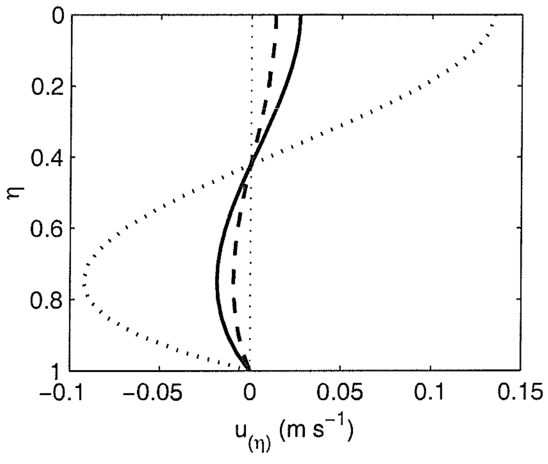

Figure 1.7: **Vertical profiles of the density-driven velocity for different intensities of mixing, $N_z = 0.001$ m^2 s^{-1} (dotted line), $N_z = 0.005$ m^2 s^{-1} (bold line), $N_z = 0.01$ m^2 s^{-1} (dashed line). The longitudinal density gradient, λ, is 2×10^{-4} kg m^{-4} and the depth, h, is 15 m.**

1.5.1 The Linden-Simpson experiments

The effects of turbulent mixing in controlling the gravitational circulation has been clearly shown by Linden and Simpson (1986) in a series of laboratory experiments. First a bi-directional flow driven by longitudinal density gradient was formed in a tank by a typical lock exchange experiment (Fig. 1.8a). Then a source of turbulent mixing, air bubbles passing through through a manifold at the bottom of the tank, was switched on and off to simulate modulation of mixing. The mixing generated by the air bubbles very rapidly reduced the vertical density gradient, leading to vertically homogeneous conditions (Fig. 1.8b). The density-driven flow was drastically reduced as a consequence of the reduced longitudinal density gradient and by the increase of the vertical mixing. They also showed the effect of the period of the modulation of mixing on the net horizontal transport, i.e. longer period oscillations lead to greater transport as the system spends more time under low mixing conditions, allowing the development of the gravitational circulation. These experiments provide a good observational insight into the link between the gravitational circulation and the turbulent mixing, analogous to the effect of the eddy viscosity, N_z, on the mean velocity profile, described by Hansen and Rattray (1965).

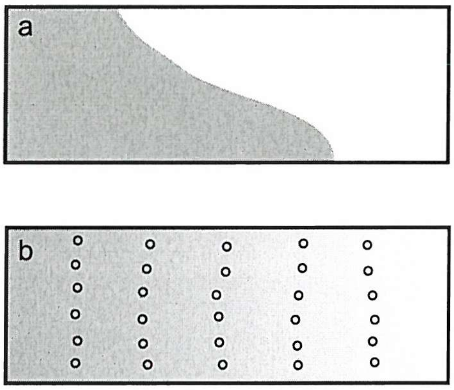

Figure 1.8: **Schematic representation of the tank experiment carried out by Linden and Simpson (1986). Lock-exchange gravitational circulation is formed under no mixing conditions (a). The presence of turbulent mixing smoothes the longitudinal density gradient and interrupts gravitational circulation (b). Circles in (b) are the air bubbles used as source of turbulence.**

1.6 Objectives

This chapter has described the mechanisms which control the occurrence of gravitational circulation in estuaries. This mechanism has its origin in the longitudinal density gradient, formed by the freshwater input from rivers, that generates a net residual transport which governs the net exchange of material along the main axis of the estuary.

Vertical mixing, induced by tidal and wind friction and by internal mixing processes, can overcome the stratification driven by the longitudinal density gradient and arrest the circulation. Although the link between vertical mixing, either induced by tidal and wind friction or by internal mixing processes, and stratification is well established in observations of estuaries, the effects of mixing on the strength of the gravitational circulation is less well understood.

The aim of this study is to investigate the density-driven flow observed in a partially mixed estuary, Southampton Water, and the influence of the variation on the strength of the vertical mixing on the gravitational circulation. Although internal waves and shear instabilities are potential sources of mixing, this study focused only on the boundary mechanisms of turbulence generation. The onset, persistence and destruction of the gravitational circulation may respond to the modulation of the tidally-induced mixing on both spring-neap and semi-diurnal time scales. The peculiar tide in Southampton Water, with different durations of low tidal current periods within a semi-diurnal cycle, provides an excellent opportunity to observe some of the processes involved in the modulation of the circulation. The importance of the wind in generating mixing and inducing currents upon surface water was also investigated. A one-dimensional numerical model is also used to provide further insight into the influences of the tidal- and wind-induced mixing on the gravitational circulation in a more controlled artificial environment.

Chapter 2

Southampton Water experiments

A series of field measurements was carried out in Southampton Water in order to to investigate any temporal fluctuations of the gravitational circulation associated with the variability of the mixing induced by both tides and wind. The simple bathymetry and the unusual tidal regime in particular, with the duration of the low turbulent slack waters varying from half to more than two hours within a semi-diurnal cycle, make Southampton Water an ideal place to study the responses of the stratification and the gravitational flow to the vertical mixing on different time-scales. This chapter will first explain the strategies used during the fieldwork, and then describe some of the general methods used to process and analyse the acquired data.

2.1 Field work

Southampton Water is a partially mixed estuary located in southern England (Fig. 2.1). It has a fairly uniform rectangular channel orientated in the northwest-southeast direction for approximately 10 km, from its mouth in the Solent to the confluence of the rivers Test and Itchen. It is approximately 1.5 km wide with large shoals extending for 500 metres on most of the the southwestern margin. It has a U-shaped main channel, 750 metres wide and regularly dredged to 12.6 metres below chart datum (Admiralty Chart no. 1905 scale 1:20000, 1994). The Solent is a well-mixed body of

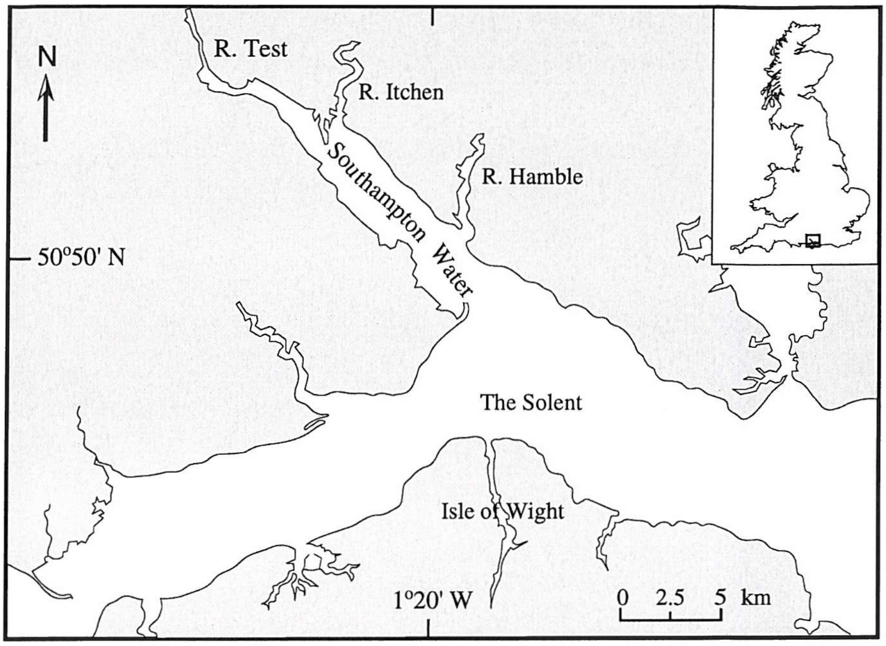

Figure 2.1: **Southampton Water, with the major tributaries at the head of the estuary, the River Test and the River Itchen, and the small tributary River Hamble near to the mouth. The Solent connects the estuary to the English Channel either side of the Isle of Wight.**

water which connects Southampton Water to the English Channel through two broad channels running on each side of the Isle of Wight. By modelling the mean M_2 induced Lagrangian residual current, Shi and Purdie (2000) found a westward net tidal flow in the Solent and a residual gyre near the mouth of the Southampton Water. Their findings suggested that this recirculation results in a residual current entering Southampton Water from the west with mean velocity around 0.05 $\mathrm{m\,s^{-1}}$ and leaving by a narrow band in the east with mean velocity up to 0.1 $\mathrm{m\,s^{-1}}$. They thus suggested this local recirculation cell at the mouth of the estuary possibly enhances the exchange rate between the Southampton Water and the Solent.

The historical averages of freshwater input into the Southampton Water from the rivers Test, Itchen and Hamble measured by the Environmental Agency are 11.0 $\mathrm{m^3\,s^{-1}}$, 5.3 $\mathrm{m^3\,s^{-1}}$and 0.5 $\mathrm{m^3\,s^{-1}}$, respectively. The total discharge has a strong seasonal component, ranging from 11.1 $\mathrm{m^3\,s^{-1}}$ in early and mid summer to 23.9 $\mathrm{m^3\,s^{-1}}$ in late winter.

Tidal current amplitudes in Southampton Water range from approximately 1.0 $\mathrm{m\,s^{-1}}$ at spring ebb tides to 0.2 $\mathrm{m\,s^{-1}}$ at neap flood tides and are characterised by unusually strong shallow water tidal harmonics. The combination of the strength of these shallow water tidal constituents with the relatively weak semi-diurnal harmonics makes the semi-diurnal tidal cycle highly distorted (Fig. 2.2). As the tidal wave propagates into the English Channel these shallow water harmonics arise mainly from bottom friction but also from other less important physical processes, such as the effect of the Earth's rotation or wave reflection along the coast (Parker, 1991). Shallow water tidal constituents are expressed in terms of a combination of higher harmonics of the astronomical constituents (Pugh, 1987). A list of the main tidal constituents and their respective amplitudes and phases is presented in section 2.2.1 of this chapter .

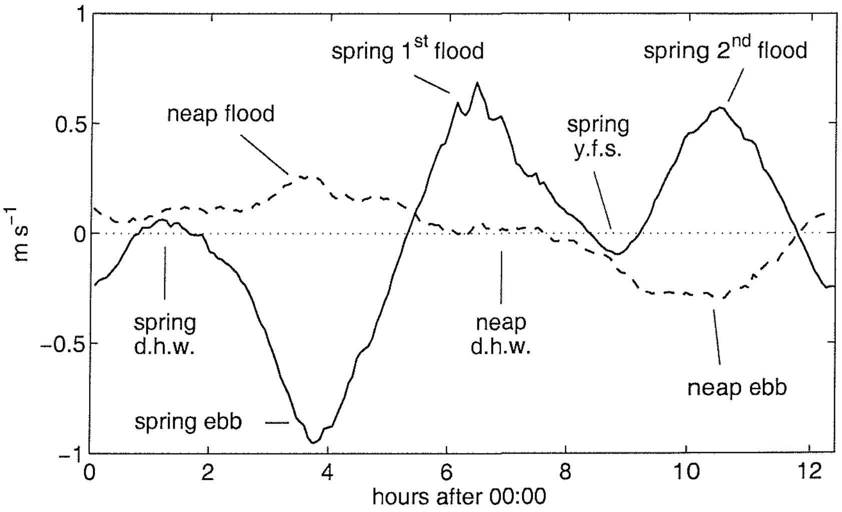

Figure 2.2: **Depth-averaged 4-min ADCP velocities for a typical spring (bold line) and neap (dashed lines) tide indicating the spring-neap difference and the unusual extended periods of low current in Southampton Water during the double high water (d.h.w.) and the young flood stand (y.f.s.) period.**

The unusual semi-diurnal cycle (Fig. 2.2) has an extended double high water that can last more than two hours, and a reduced ebb period with ebb currents higher than those found during the flood. There is also a young flood stand, which can reduce the flood current strength for approximately one hour. Occasionally currents can reach zero velocity or briefly reverse the flow to a short weak ebb-like pulse during the young flood stand periods. These characteristics are more distinguishable at spring than at neap tides. Periods of low tidal current velocities range from less than 30 minutes during the low water slack to around 1 hour during the young flood stand, and more than 2 hours during the double high water. The interaction between a weak M_2 and a relatively strong N_2 tidal components also produces a monthly modulation of the tides (Fig. 2.3) which can result in differences larger than 1 metre between the tidal range of consecutive springs (e.g., from day 25 to day 40) or consecutive neaps (e.g., from day 328 to day 343).

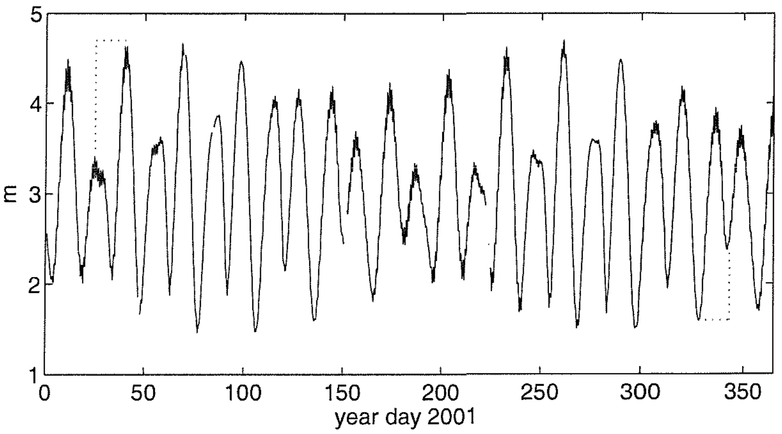

Figure 2.3: **Semi-diurnal tidal range of the surface height from the Dockland gauge station at the head of the estuary over 2001 showing the monthly variation of the tidal height for consecutive springs and neaps. Dotted lines show the large difference between consecutive springs (on the left) and between consecutive neaps (on the right).**

In order to investigate the response of the gravitational flow to the variability of the turbulent mixing three long-term moorings were deployed at a position in the middle of the estuary, for a total of 268 days of measurement from March 2001 to April 2002 (Fig. 2.4). These deployments are described in the following section.

2.1.1 Long term deployments

Three long term deployments were carried out between March 2001 and April 2002, acquiring data over a total of 268 days (Fig. 2.4). All moorings were deployed at the

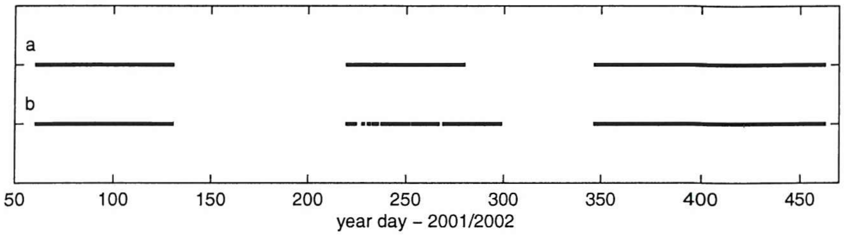

Figure 2.4: **Days of sampling for the (a) c-t loggers time-series and (b) ADCP time-series. Year day starts counting at 0.0 at 00:00, 1 January 2001.**

same site and consisted of one upward looking ADCP anchored at the bed of the estuary and two conductivity-temperature (C-T) probes, one at the surface and the other on the ADCP frame close to the seabed (Fig. 2.5).

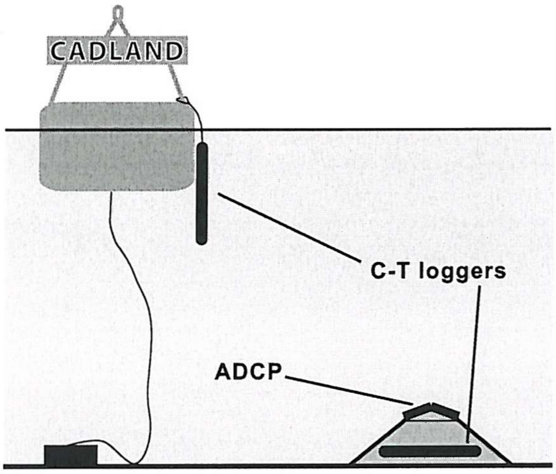

Figure 2.5: **Schematic diagram of the configuration of the three moorings deployed in the Southampton Water at Cadland navigation buoy. The ADCP was anchored at the bed of the estuary facing upward and had a C-T logger attached to its frame. The surface CT-logger was fastened on the Cadland buoy.**

The choice of the mooring site was made based on several considerations: local depth, bathymetry, navigation safety issues, and trawler avoidance. The aim was to site the mooring approximately halfway along the length of Southampton Water, far enough from the head and the mouth of the estuary to minimise any disturbances of both the rivers confluence and the well-mixed waters of the Solent. Bearing in mind these preconditions the selected site was located in the vicinity of the Cadland Buoy

(50° 51' N; 1° 20.5' W) (Fig. 2.6). This navigation buoy is moored at a depth of 10 metres below the Ordnance Survey chart datum at the edge of the main navigation channel. It is located 4 km from the mouth of the estuary and 5.5 km from the head. Due to the heavy traffic of big container vessels to and from the port of Southampton in the upper estuary, the mooring was placed out of the deeper main channel in water 6 to 8 metres deep below chart datum inshore of the Cadland buoy. This is also a region with no fishery activities. Prior to the first deployment a simple bathymetric survey was done to select the most uniform part of this area to avoid bottom irregularities.

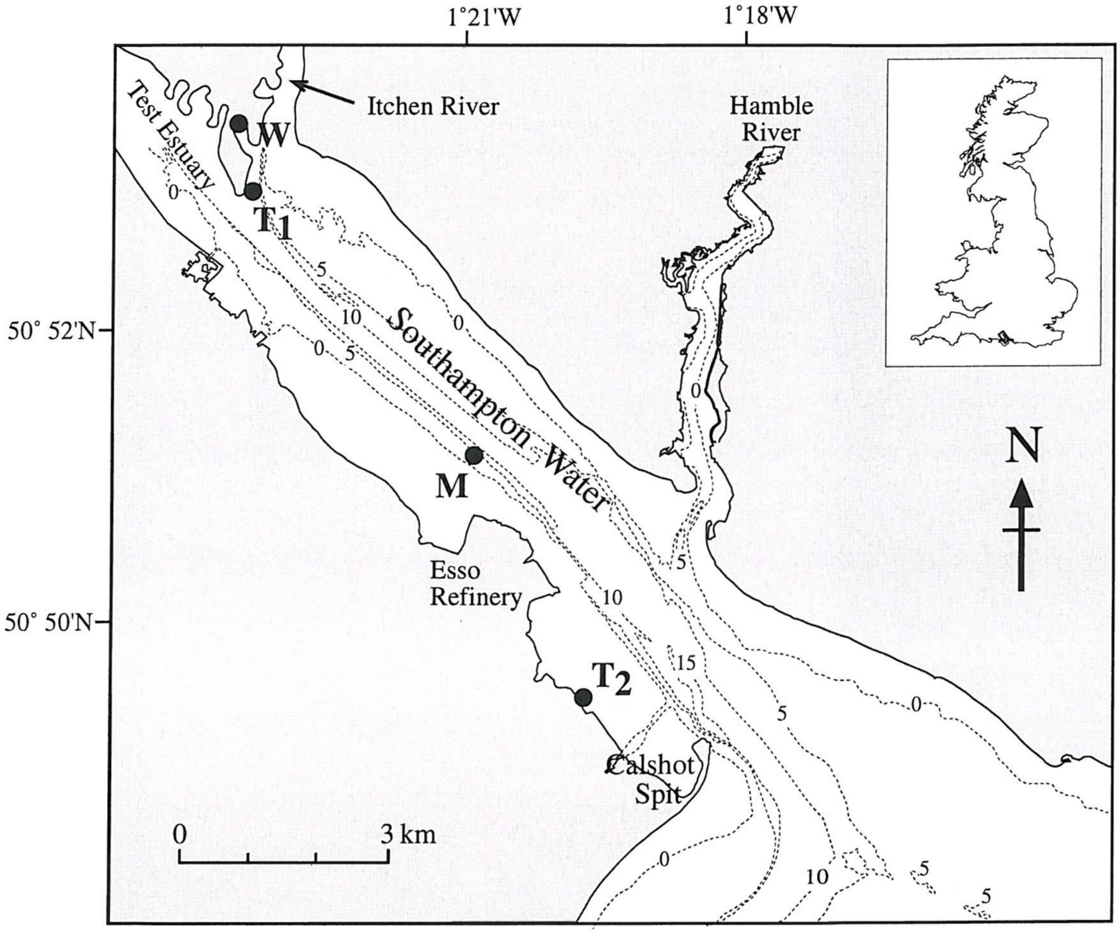

Figure 2.6: **Southampton Water, indicating the mooring site (M) at Cadland buoy, the meteorological station W on the SOC building and the tidal gauges T_1 at Dockhead and T_2 at Calshot, respectively at the head and the mouth of the estuary. Dotted lines are isobaths below Ordnance Survey chart datum.**

In spite of the bathymetric influence on mean flow has been observed in wider

Table 2.1: **Duration and ADCP sampling and averaging-rate for each of the long-term deployments.**

deployment	*starting date*	*ending date*	*duration*	*sampling rate*	*averaged pings*
spring	01 Mar 2001	11 May 2001	71 days	4 min	120
summer	07 Aug 2001	26 Oct 2001	80 days	4 min	120
winter	12 Dec 2001	08 Apr 2002	117 days	5 min	45

estuaries (e. g. Chesapeake Bay, Valle-Levinson and Lwisa, 1995, 1997), according to these authors the dimensions of Southampton Water (i.e. length, width, depth and the ratio between the shoal and the channel depths) are less favorable for a lateral variation of the residual circulation. Li and O'Donnel (1997) showed in their 2-D model results of a 4 km wide estuary that the residual vertical velocity for a ratio between the shoal and the channel depths of the Southampton Water (≈ 0.6) is 0.01 $\mathrm{m\,s^{-1}}$. This is at the same order of magnitude of the ADCP standard deviation (see below the Data Quality section).

A four beam, 1200 kHz, RD Instruments ADCP was moored facing upwards, mounted in a pyramidal frame anchored on the bed of the estuary. The vertical resolution of the ADCP profiles was 25 cm in all three deployments. After accounting for the height above the seabed of the ADCP head and the blank data layer immediately on the top of the instrument, the deepest current measurement was taken at 1.5 m above the bed. The near-surface current was located at 0.75 m below the surface, at 92 % of the water column due to the sidelobe effect of the 20° inclination of the ADCP beams relative to the vertical. Deployment start and end days, duration, sampling rate, and number of averaged pings are listed for each deployment in Table 2.1. The differences between numbers of pings averaged and sampling rates for different deployments were due to the planned length of each deployment combined with the limit of data storage and with the battery power available.

Surface and bottom time-series of temperature and conductivity were measured by Brancker XL-210 C-T probes in the three deployments. The surface probe was attached to the Cadland Buoy with sensors at 1 m below the surface. At the bottom the probe was fixed to the ADCP frame, placed at 0.5 m above the estuary bed. A 10-minute sampling interval was set at both depths for the three deployments. Due to an error in the configuration of the loggers, data acquisition stopped on the second deployment 19 days before the recovery of the mooring after day 280. Density was calculated combining temperature and salinity by using the equation of state (Millero and Poisson, 1981) neglecting the effect of pressure on the calculation.

Data quality

The estimated standard deviation of the current measurement was 0.01 $\mathrm{m\,s^{-1}}$ on the first and second deployment and 0.04 $\mathrm{m\,s^{-1}}$ on the third (RDInstruments, 1993). The different standard deviation is related to the set up of the number of pings for each deployments (Table 2.1). The angle between the ADCP transducer and the horizontal plane given by the pitch-roll inclination was less than 2 ° in all deployments.

The most serious data problem was a series of intermittent failures which occurred in the ADCP dataset during three weeks at the beginning of the second deployment, between days 223 and 244, without any relation to the semi-diurnal tidal cycle. Low values of echo intensity and correlation, mainly in two of the four ADCP beams, were present in most of the water column for periods varying from 4 minutes to 3 hours (Fig. 2.7a), resulting in velocity errors of the same order of magnitude of the horizontal velocities. The reason for these errors is unknown, but giving the intermittent pattern it could be caused by some neutral floating debris that had been entangled on the ADCP frame and covered the affected transducers. The absence of poor quality data after day 244, when the source of disturbance was probably removed by tidal currents, reinforces the 'plastic bag theory'. Apart from these significant failures during the summer deployment, short gaps occasionally occurred in the rest of this dataset and in the other ADCP series.

Discrete, 250 ml, water samples were collected approximately every hour in both surface and bottom layers using a Niskin bottle during six semi-diurnal tidal cycle sampling surveys carried out during the mooring deployments. Additional opportunistic water samples were taken by other PhD students on their own research field work in the Southampton Water during the mooring deployments. Salinity samples were analysed

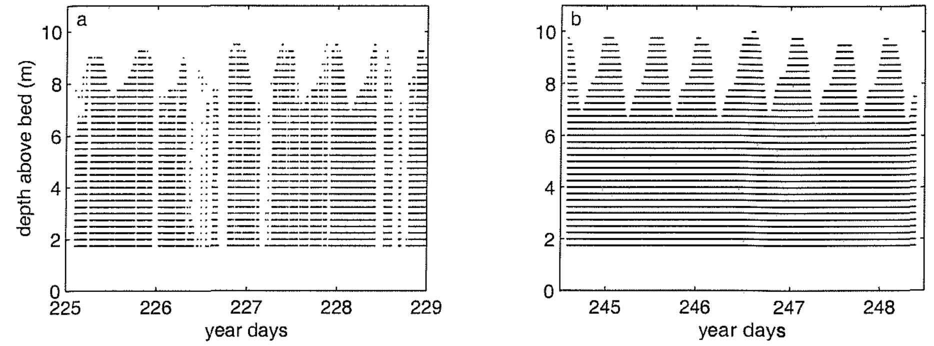

Figure 2.7: **Comparison between two 4-day sequences of ADCP profiles with (a) poor and (b) good data quality. Both datasets were collected at spring tides on the second deployment. Each dot shows a good quality measurement after the removal of the poor quality data.**

on a Guildline Autosal salinometer and the results were used to calibrate the Brancker loggers measurements to ± 0.05 on the Practical Salinity Scale, 1978. Conductivity time-series were successfully calibrated, apart from some highly irregular bottom measurements acquired during both the second and the third deployments (Fig. 2.8).

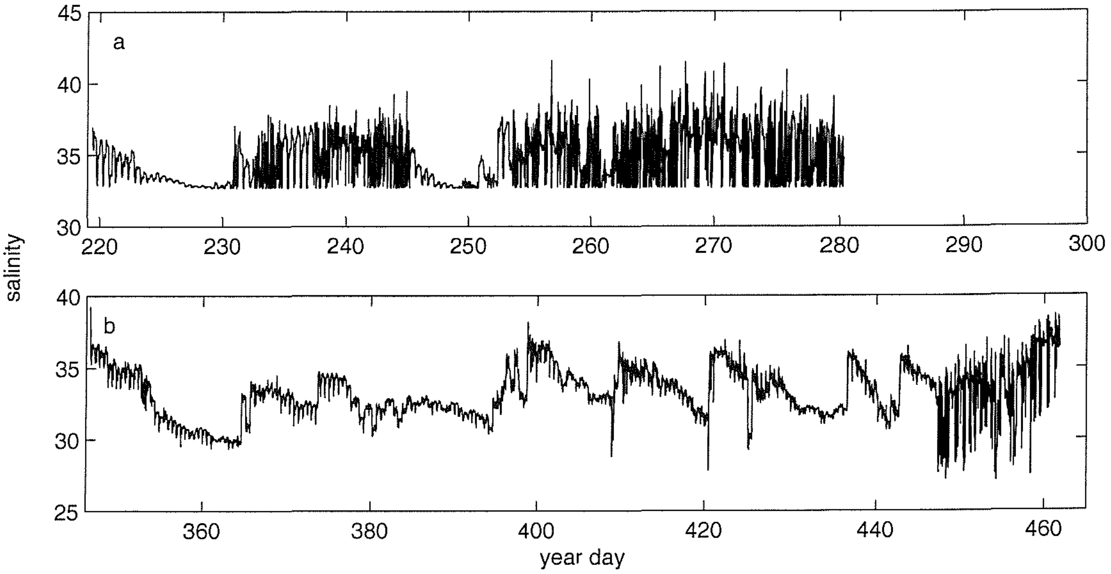

Figure 2.8: **Time-series of the poor quality salinity measurements from the bottom C-T logger, showing (a) the scatter pattern on the second deployment, and (b) a series of gentle decreases followed by steep increases of the salinity in third deployment.**

Salinity values obtained from the second conductivity measurements were very scattered throughout the whole time-series (Fig. 2.8a), changing more than 5 units within the 10 minutes of the sampling rate. Although it is difficult to speculate about the possible reasons for this odd behaviour, it seemed to be caused by an internal electronic failure on the C-T logger. During the third deployment the bottom salinity time-series presented periods of low values (Fig. 2.8b) followed by abrupt increases. Those low salinity readings reached unrealistic values, lower than the salinity at the surface. A reason for the seesaw pattern observed in this salinity time-series could be the accumulation of fine sediments in the conductivity cell tube. Tidal currents could flush the sediment out from the tube and promote the quick return of the conductivity to a more typical value. Towards the end of this deployment a highly scattered signal similar to that observed in the summer 2001 became present, probably caused by the same reason. Due to the poor quality of those time-series and the lack of confidence in the calibration it was decided not to use them.

2.1.2 Additional environmental data

In addition to the data acquired by the long-term deployments additional environmental data were collected to include other forces that could affect the temporal variability of the gravitational circulation.

Meteorological data

Meteorological data, including air temperature, solar radiation, and velocity and direction of the wind, were sampled hourly by the meteorological station on the roof of the Southampton Oceanography Centre building (Fig. 2.6) at 25 metres above the Ordinance Survey British datum. In order to calculate the wind stress wind data had to be adjusted from the measurement height to the common reference height of 10 metres (Smith, 1988). For this adjustment a simplified expression of the wind profile dependence on the sea roughness for stable atmospheric conditions (Mahrt et al., 2003) can be used

$$\frac{W_H}{W_{10}} = \frac{\ln(H/z_0)}{\ln(10/z_0)} \tag{2.1}$$

where W_H is the wind speed ($\mathrm{m\,s^{-1}}$) measured at a height of H metres above the surface, W_{10} is the wind speed ($\mathrm{m\,s^{-1}}$) at 10 metres, and z_0 is the height above the sea surface where the wind speed reaches zero, the aerodynamic roughness. Neglecting the limitations applied to this relation for $W_{10} < 4\ \mathrm{m\,s^{-1}}$ (Mahrt et al., 2003) and considering a constant z_0 of 10^{-5} m for a small wind fetch (Kitaigorodskii, 2003), the ratio $\mathrm{W_{25}/W_{10}}$ is 1.06.

The horizontal components of wind stress, $\tau_{W(x,y)}$, can be calculated based on the quadratic drag law as

$$\tau_{W(x)} = C_d \rho_{air} u_{w10} (u_{w10}^2 + v_{w10}^2)^{1/2}\ (\mathrm{N\,m^{-2}}) \tag{2.2}$$

and

$$\tau_{W(y)} = C_d \rho_{air} v_{w10} (u_{w10}^2 + v_{w10}^2)^{1/2}\ (\mathrm{N\,m^{-2}}) \tag{2.3}$$

where C_d is the dimensionless drag coefficient, ρ_{air} is the air density ($\sim 1.29\ \mathrm{kg\,m^{-3}}$) and u_{w10} and v_{w10} are the east and north components of wind speed at 10 m height in $\mathrm{m\,s^{-1}}$, respectively.

Changes of the water surface roughness induced by the wind velocity variability may affect stress on the sea surface boundary, resulting in changes in the drag coefficient. Wind speed adjustment of C_d using the empirical relation proposed by Smith (1988), formulated as

$$\begin{aligned} C_d &= 1.7 \times 10^{-3} + 2.1 \times 10^{-5} \ln W_{10} \quad &&\text{for } W_{10} < 5\ \mathrm{m\,s^{-1}}, \text{ and} &(2.4)\\ C_d &= 1.48 \times 10^{-3} + 4 \times 10^{-5} W_{10} \quad &&\text{for } W_{10} \geq 5\ \mathrm{m\,s^{-1}}. &(2.5) \end{aligned}$$

with W_{10} the wind speed magnitude ($\mathrm{m\,s^{-1}}$) at 10 metres above the surface (Fig. 2.9), considering a constant air temperature of 14°C. The daily mean of the air temperature measured at the meteorological station site during the period of this study ranged from 5°C in the winter to 22°C in the summer. Effects of this seasonal variation of temperature on the results of the drag coefficient are less than 5% and were neglected.

As the SOC meteorological station does not have a pressure sensor it was decided to use an hourly mean sea level atmospheric pressure dataset from the Solent station

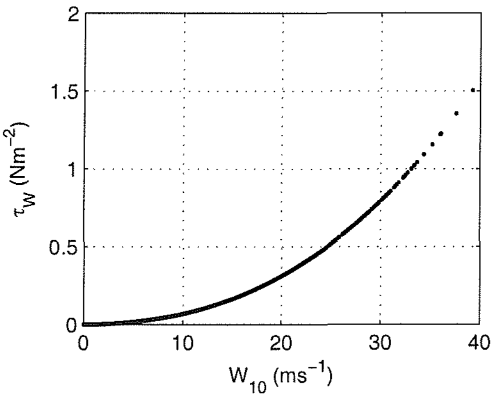

Figure 2.9: **Data points of wind speed adjusted to 10 metres height, W_{10}, plotted against wind stress, τ_W. Data are based on the hourly measurements during the winter deployment.**

(part of the national meteorological surface stations network managed by the Met Office). This station is located nearby the mouth of the Southampton Water in Lee-on-Solent (50° 48' N; 1° 13' W).

Tidal height data

Data from two tide gauges in Southampton Water were provided by Associated British Ports (ABP) over the period of the fieldwork. These tidal stations are located at Calshot at the mouth of the estuary, and at Dockhead at the head of the estuary (Fig. 2.6). Tidal height data are levelled to Ordinance Survey datum. The sampling frequency was 12 minutes for both gauges but the gauges do not sample at the same times. Each data set was then interpolated onto a common 10-minute time base. Due to the tidal dynamics in Southampton Water, with rapid changes of the water height, gaps in the time series longer than 1 hour were not interpolated.

The sea surface and the mouth-to-head surface slope were estimated by using these tide gauges. Due to the accuracy of the gauges measurements of 0.02 m, slopes lower than 0.04 m were neglected in the analysis. The non-tidal fluctuation of the sea surface was calculated for the two sites by subtracting the tidally predicted height (also supplied by ABP) from the gauge measurement. The non-tidal sea surface slope between the head and the mouth of the estuary was obtained by difference between the non-tidal level at the two stations.

River flow data

The freshwater input to Southampton Water during the period of the three longer deployments (March 2001 to April 2002) was assessed by using the river flow measurements of the major freshwater supplier to the estuary, the River Test (Fig. 2.10). The mouth of the Test is formed by different channels and the total freshwater inflow can be calculated by summing the discharge at four different stations operated by the Environmental Agency (Testwood, Conagar Bridge, Ower and Test back carrier). The relative contribution of each of these stations to the total discharge during the period of the available data was 76, 17, 6 and 1 %, respectively. An additional flow from a fish farm bypass located near the mouth of the river is not gauged but represents less than 1 % of the overall discharge (Bethan Davies, Environmental Agency, pers. com.). River flow data from the River Itchen was available only for 2001, with discharge approximately half of the River Test (7.0 $m^3 s^{-1}$ compared to 14.2 $m^3 s^{-1}$ for the period). As both catchment areas are in the same region and have similar geological characteristics, the observed variation on the discharge in the Test River was considered the same for the River Itchen.

2.2 General methods

The more general methods used in the data analyses will be described here. Detailed methods developed for specific analyses will be described in the relevant parts of the results and discussion sections in the Chapters 3 and 4.

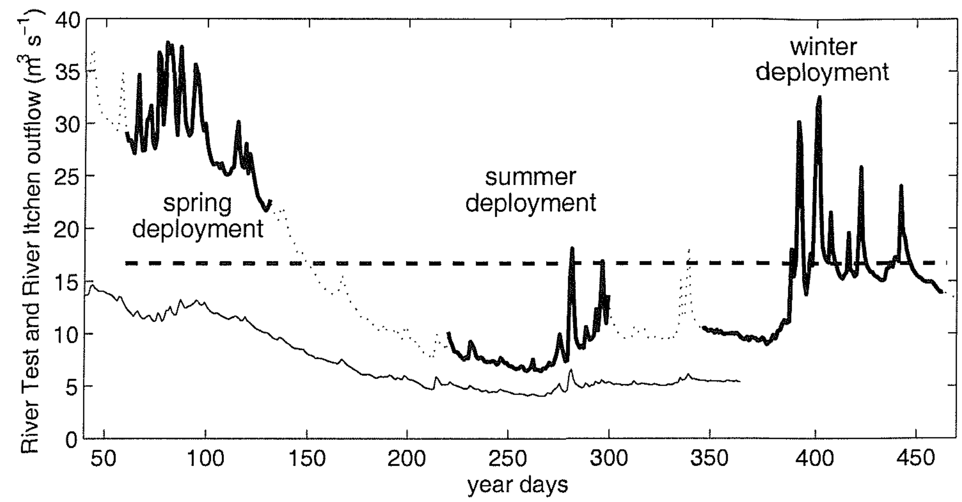

Figure 2.10: **Discharges of the River Test and River Itchen into Southampton Water. The thick/dotted line shows the River Test discharge, highlighting the periods of the deployments. The thin gray line is the River Itchen discharge for 2001. The thick dashed line shows the overall mean flow for the River Test for the period. Year day starts counting at 0.0 at 00:00, 1 January 2001.**

2.2.1 Tidal analyses

Knowledge of the harmonic structure of both the tidal currents and the tidal sea level is essential for tide-related analysis of the data collected in the Southampton Water. The procedures used to extract the harmonic constituents from the ADCP tidal current are described in the following subsection.

Tidal current

ADCP current direction was initially referenced to the magnetic north (4° W from true N) in all deployments. A 45° counterclockwise rotation was applied to juxtapose the y-axis of the ADCP current measurements on the main estuarine axis. Hereinafter the coordinate system has the x-axis in the cross estuary direction, where u is the transversal current, positive towards the NE, and the y-axis along the main estuary axis with the current component v positive into the estuary towards the NW. The vertical z-axis is positive upwards.

To identify which are the important harmonics a spectral analysis, using a Fast Fourier Transform (FFT), was applied to the depth-averaged velocity of each ADCP time series. The spectra have been smoothed to increase the confidence in the spectral peaks by using a cosine bell filter with 16 degrees of freedom (Emery and Thomson, 1997). The results (Fig. 2.11) illustrate the main tidal characteristics of Southampton Water (see section 2.1), showing the strong presence of the shallow water constituent, the relatively weak M_2, and the negligible presence of any diurnal harmonic.

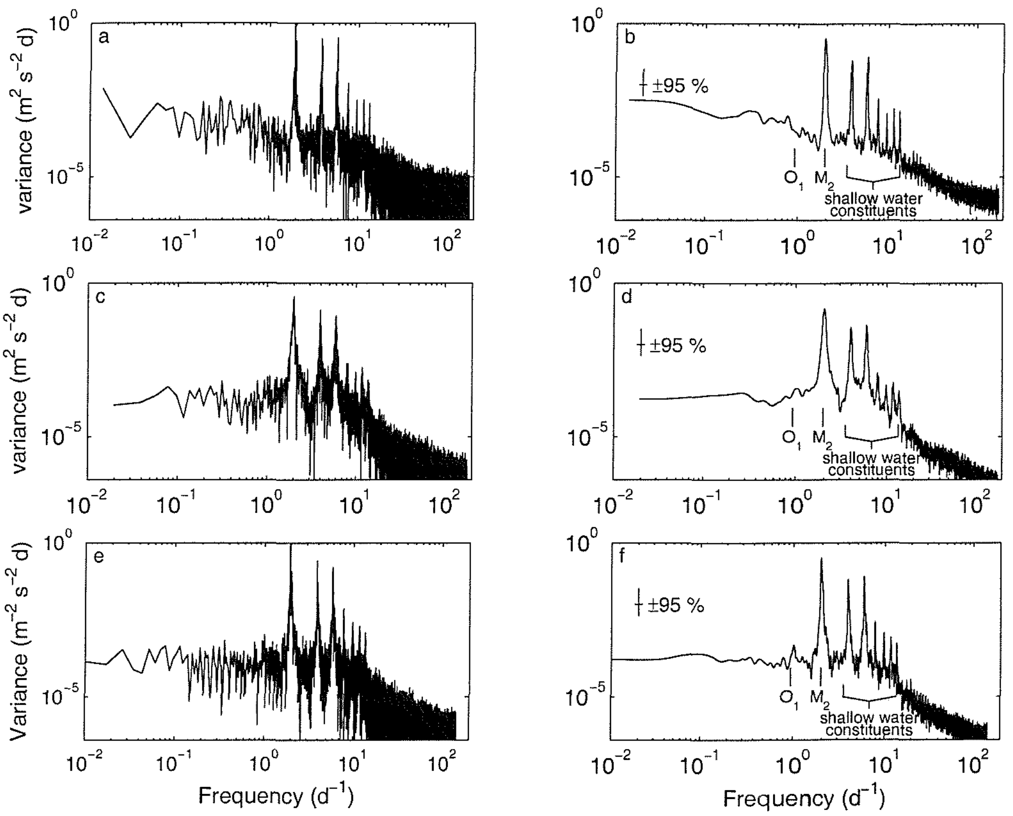

Figure 2.11: **Power spectrum density of the depth-averaged along-estuary current for the (a and b) spring, (c and d) summer and (e and f) winter deployments. The semi-diurnal characteristics of the tide in Southampton Water is illustrated by the peaks in the semi-diurnal (M_2) and shallow water tidal harmonics associated with bottom friction. It also shows the weakness of the diurnal tidal constituents (O_1). The raw spectra (a, c and e) were smoothed with a cosine bell filter, with 16 d. o. f. (b, d and f).**

In order to achieve a satisfactory separation of the tidal harmonics within a narrow frequency band (e.g. the semi-diurnal constituents S_2, M_2 and N_2) the Rayleigh condition must be applied. It states that two neighbouring constituents must be separated by at least a complete period from each other over the length of the available data. Its formulation is

$$T > \frac{1}{|f_{C1} - f_{C2}|} \quad [\mathrm{s}] \tag{2.6}$$

with f_{C1} and f_{C2} the tidal constituents frequencies and T the length of the time series. The multiplication of the length of the time series by a factor lower than the unity on the left hand side of the equation 2.6 increases the confidence in the analyses. Taking the smallest frequency difference found between the more important tidal harmonics in Southampton Water (4.1×10^{-7} s^{-1} between M$_6$ and 2MN$_6$) the length of the time series must be larger than 29 days in order to resolve the harmonics. A list of the harmonics and their frequency, amplitude and phase is shown in Table 2.2.

Table 2.2: **Amplitude and phase of the tidal harmonic constituents found in the harmonic analyses of the depth-mean velocity in Southampton Water and used in the calculations of the residual currents.**

		spring	*summer*	*winter*
harmonic	*frequency (cpd)*	$v_c(m\ s^{-1})/\Phi_c(^\circ)$	$v_c(m\ s^{-1})/\Phi_c(^\circ)$	$v_c(m\ s^{-1})/\Phi_c(^\circ)$
M$_f$	0.0720	0.009/314	0.001/127	0.005/318
O$_1$	0.9295	0.003/102	0.002/291	0.005/40
P$_1$	0.9973	0.003/312	0.004/88	0.005/256
K$_1$	1.0027	0.005/267	0.008/28	0.007/198
N$_2$	1.8960	0.081/119	0.068/201	0.053/214
M$_2$	1.9323	0.278/21	0.283/34	0.279/248
S$_2$	2.0000	0.095/143	0.104/339	0.085/129
MN$_4$	3.8285	0.048/241	0.044/312	0.043/186
M$_4$	3.8645	0.112/123	0.119/136	0.118/226
MS$_4$	3.9323	0.097/212	0.110/71	0.087/99
2MN$_6$	5.7613	0.076/287	0.067/11	0.073/90
M$_6$	5.7968	0.118/157	0.112/172	0.128/126
2MS$_6$	5.8645	0.166/266	0.156/126	0.149/346
M$_8$	7.7291	0.021/96	0.017/13	0.020/189
M$_{10}$	9.6614	0.007/144	0.005/255	0.008/337
M$_{12}$	11.5936	0.014/47	0.013/108	0.010/63
M$_{14}$	13.5259	0.014/91	0.010/183	0.009/27

Having identified the important tidal frequencies in the depth-averaged velocity time series, their amplitudes and phases were obtained by harmonic tidal analysis. The least square fitting method was applied to the depth-averaged main-axis v velocity time series for the three deployments, following the set of equations described by Emery and Thomson (1997) (p. 393-396). It describes the time series as a sum of sinusoidal curves, one for each tidal constituent, as

$$v(t) = v_o + \sum_{c=1}^{n} v_c \sin(\omega_c t + \phi_c) \qquad [\mathrm{m\,s^{-1}}] \tag{2.7}$$

where $v(t)$ is the tidal velocity, v_o is the mean velocity, and v_c, ω_c and ϕ_c are the velocity amplitude, the angular frequency (rad s^{-1}) and the phase (rad) of each of the n tidal constituents c, respectively. Phases are relative to the time of the beginning of each ADCP time series (1st March 2001 at 1040 UTC for the first deployment; 7th August 2001 at 0844 UTC for the second deployment; and 12th December 2001 at 1040 UTC for the third deployment).

Interactions between the N_2 and S_2 harmonics and the relatively weak M_2 in Southampton Water lead to two groups of strong tidal constituents with similar frequency, the forth-diurnal harmonics MN_4, M_4 and MS_4 ($\approx$ 3.9 cycles per day) and the sixth-diurnal harmonics $2MN_6$, M_6 and $2MS_6$ ($\approx$ 5.8 cpd). Separately, the amplitudes of these shallow water constituents are 15-60 % of the M_2 amplitude.

Once the tidal current was separated from the ADCP dataset by the harmonic analyses, the non-tidal or residual current could be calculated by subtracting the tidal velocity, $v(t)$, from the measurements (Fig. 2.12).

Residuals were obtained for surface, bottom and depth-mean velocities in all three deployments. Mean square errors were very similar in the three deployments and slightly larger on the surface, possibly due to the wind-stress influence on the surface currents (Table 2.3).

Tidal surface level

The predicted tidal surface level has been calculated by the United Kingdom Hydrographic Office (UKHO) in Taunton for ABP but the details of the phase and ampli-

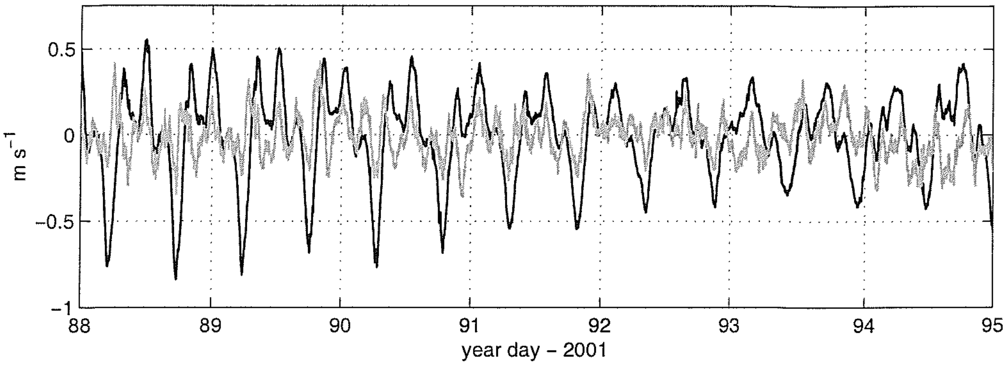

Figure 2.12: **Spring-to-neap transition of the depth-mean ADCP velocity (black line) and calculated depth-mean residual velocity (gray line) between year days 88 (29 March) and 94 (4 April). Year day starts counting at 0.0 at 00:00, 1 January 2001.**

Table 2.3: **Mean square error of the residual currents calculation for the three deployments in m^2 s^{-2}.**

	spring (m^2s^{-2})	*summer* (m^2s^{-2})	*winter* (m^2s^{-2})
surface	0.0140	0.0158	0.0168
depth-mean	0.0099	0.0091	0.0090
bottom	0.0104	0.0082	0.0076

tude of the harmonic constituents could not be made available. However the accuracy of the applied method in removing the tidal signal out of the tidal gauge measurements can be tested by applying a spectral analysis, using a FFT, in both the measured and non-tidal sea surface height time series (Fig. 2.13). Spectra have been smoothed by using a cosine bell filter, with 16 degrees of freedom (Emery and Thomson, 1997). The root mean square (rms) error of the non-tidal sea surface height is 0.04 m for the Dockhead gauge and 0.05 for the Calshot gauge time series.

2.2.2 The longitudinal density gradient

Although there was no direct measurement of temperature and salinity along the estuary during the period of the mooring deployments, the longitudinal density gradient can be estimated by using the C-T logger density measurements and the ADCP along-

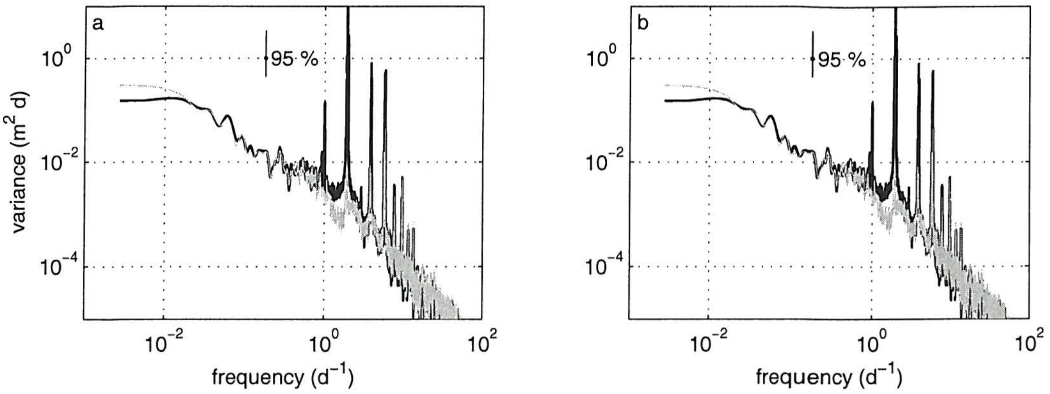

Figure 2.13: **Power spectra density of the measured (black line) and non-tidal sea surface height (gray line) at (a) Dockhead and (b) Calshot. The spectra were averaged with cosine bell filter, with 16 d. o. f.**

estuary velocities. By assuming the temporal variability of surface density at a certain point in the estuary is dominated by advection, and neglecting any cross-estuary density gradient, which is justified based on independent measurements of the cross-estuary density gradient (not shown), the density advection equation can be written as

$$\frac{d\bar{\rho}}{dt} = -\bar{u}\frac{d\rho}{dx} \qquad [\mathrm{kg\,m^{-3}s^{-1}}] \tag{2.8}$$

(Uncles and Radford, 1980, Simpson et al., 1990). Applying it to Southampton Water conditions the longitudinal density gradient can be estimated as

$$\lambda = \frac{d\rho}{dy} = -\frac{1}{v_s}\frac{d\rho_s}{dt} \simeq -\frac{1}{\overline{v_s}}\frac{\Delta\rho_s}{\Delta t} \qquad [\mathrm{kg\,m^{-4}}] \tag{2.9}$$

where v_s is the surface along-estuary velocity from the ADCP data set and ρ_s is the surface density from the C-T loggers. $\overline{v_s}$ is the mean surface velocity and $\Delta\rho_s$ the surface density difference over Δt. The use of the surface values of density and velocity instead of depth-averaged quantities was necessary due to the bad data recorded by the bottom conductivity sensor on both the second and the third deployments. Linear interpolation was used to fill data gaps in both the surface density and the ADCP time series at any time that the length of the data gap was shorter than one hour. Gaps longer than 1 hour were left blank, avoiding the possibility of poorly interpolated data due to rapid tidal variability.

The longitudinal density gradient was first calculated for every hour (Δt = 1 hour). The results for the hourly λ were very noisy, with very high isolated values due to occasionally very low hourly averaged velocity, mainly associated with the extended slack water periods at double high water. Instead of using the spiky hourly λ it was decided to calculate it for every ebb period when the flow and density are better defined. This procedure would give the displacement of the less dense water at the surface during each of the ebb tides, with the ebb average surface velocity $\overline{v_{ebb}}$ and the surface C-T logger density difference $\Delta\rho_{ebb}$ / Δt_{ebb} replacing $\overline{v_s}$ and $\Delta\rho_s$ / Δt in equation 2.9. $\Delta\rho_{ebb}$ is the variation of the surface density over the ebb tide and Δt_{ebb} is the time length on the ebb tide. Negative λ occurred due to small increases in density on a few occasions. To avoid these negative values of λ, density was averaged over a one-hour window centred at the start and at the end of the ebb time length, instead of using isolated measurements.

Chapter 3

Spring-neap modulation

This chapter is focused on the long-term fluctuation of the sub-tidal currents in Southampton Water and the potential for the modulation of the gravitational circulation as a result of the spring-neap variability of tidal mixing. Firstly the calculation of the tidally-averaged velocity is described and then the results of the three deployments are presented and discussed. These results show the variability of the gravitational circulation over 268 days during the deployments in Southampton Water. The effects of the wind on the gravitational circulation by generating mixing and inducing the movement of surface water windward are also discussed, as is the influence of the sub-tidal variations of the sea surface level.

3.1 The tidally-averaged velocity

This section describes the method used to obtain time series of tidally-averaged velocity from the three long-term ADCP data sets. Time, depth, and along estuary current velocity were extracted from the ADCP records after the pre-processing stage described in the Chapter 3. Bearing in mind the fixed vertical resolution of 0.25 m for the ADCP readings, the number of cells with valid measurements in each current profile varied according to the tidal variation of the water level, which ranged from a total depth of 7.5 metres at lowest low water to 12 metres at highest high water at the mooring site. Therefore the number of valid measurements in a raw ADCP profile could range from a minimum of 20 to a maximum of 38, considering the ADCP limitations in acquiring data near both the bottom and the surface (Fig. 3.1). In order to remove the tidal variability and achieve a common fixed vertical grid throughout the time series, depth was normalised in terms of the total depth H and the cell depth z. Profiles of the raw values of the along-estuary velocity were individually normalised by using linear interpolation with a fixed number of 30 cells for each profile. The normalised cell depth $\eta = z/H$ ranges from 0 at the estuary bottom to 1 at the surface.

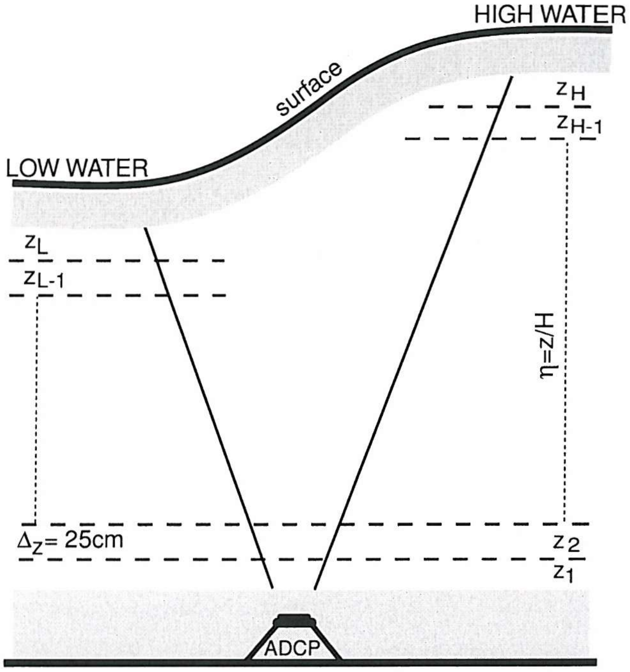

Figure 3.1: **Schematic of variability on the cell numbers recorded in the ADCP profiles within a semi-diurnal cycle. Normalised depth $\eta = z/H$ is used to transform the tidally-variable vertical grid of the raw ADCP measurements to a fixed coordinate. z_L and z_H are the upper cells at low and high water, respectively, and the shadow areas represent the regions with no ADCP readings near surface (side-lobe effect) and bed (transducer height and distance threshold for signal identification).**

The depth-normalised tidally-averaged along-estuary velocity was calculated using the least-squares harmonic analysis method as described in the section 2.2.1. This method method is used to express the vertically-interpolated velocities at each depth η

as a sum of harmonic constituents in the form of

$$v(\eta) \quad = \quad v_o(\eta) + \sum_{c=1}^{n} A_c(\eta)\ \cos(\omega_c\, t + \phi_c(\eta)) \qquad [\mathrm{m\,s^{-1}}] \qquad (3.1)$$

where $v(\eta)$ is the depth-normalised velocity time series, $v_o(\eta)$ is the tidally averaged velocity ($\mathrm{m\,s^{-1}}$), obtained from the harmonic analysis, A_c, ω_c and ϕ_c are the velocity amplitude ($\mathrm{m\,s^{-1}}$), the frequency ($\mathrm{s^{-1}}$) and the phase (rad) of the c^{th} tidal harmonic, respectively. The residual velocity, v_R, is the difference between $v(\eta)$ and the harmonic analysis results stated under squared brackets in equation 3.1. Hourly profiles of $v_o(\eta)$ were calculated by continuously shifting a 25-hour width window forward with a one-hour time step through the depth-normalised along-estuary velocity time series as illustrated in the figure 3.2.

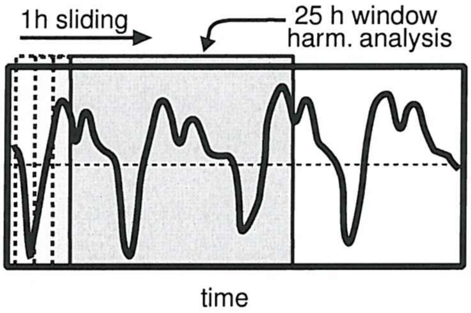

Figure 3.2: **25 hour width window sliding over the ADCP time series. Sliding time step is 1 hour. Analysis was carried out of the 25 hour time series at the 30 evenly-spaced positions on the normalised vertical grid.**

Harmonic analysis was applied to data for frequencies higher than the 25-h length of the sub-sampled data limited by the window width, i.e. M_2, M_4, M_6, M_8, M_{10}, M_{12} and M_{14}. The choice of these shallow water constituents was based on the FFT tidal analyses described in section 2.2.1 (Fig. 2.11). Diurnal tidal harmonics have a negligible presence in the tidal signal in Southampton Water. By choosing a window-length for the harmonic analysis twice the width of the lowest main harmonic frequency, i.e. semi-diurnal cycle, the undesirable deleterious effects of the use of conventional least squares method on short time series (Jay and Flinchen, 1999) can be avoided. At any level η, the root mean square (rms) of the observed currents about those predicted from equation 3.1

were typically 0.04-0.05 $\mathrm{m\,s^{-1}}$ around neap tides, increasing to 0.07-0.08 $\mathrm{m\,s^{-1}}$ at springs (Fig. 3.3). Greater errors at spring tides were dominated by underprediction of the peak current at floods and ebbs. Considering the low errors obtained by the least squares method, it was decided to use this much simpler method than the wavelet analysis, suggested by Jay and Flinchen (1999) as an alternative for tidal analysis on short time series.

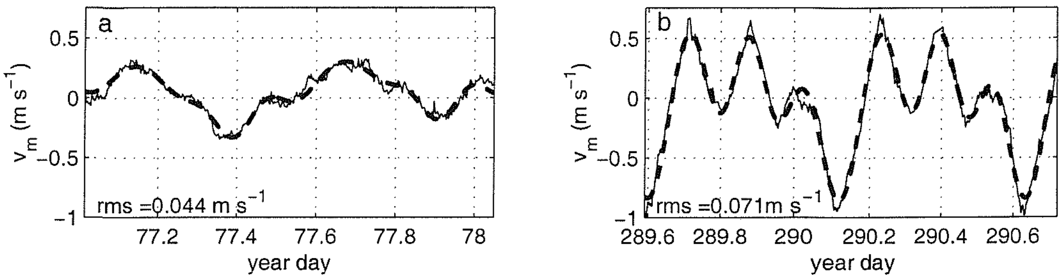

Figure 3.3: **Observed (bold line) and predicted (dashed line) mid-depth tidal current v_m for typical neap (a) and spring (b) 25 hour data set, with the respective root mean square (rms).**

To assess the ability of the stretched vertical coordinate to reproduce the currents recorded in the original grid, the velocity amplitudes v_c of the main tidal constituents M_2, M_4 and M_6 from the original and the normalised grid were compared. Results showed an agreement greater than 85% between original and stretched coordinate grids at three different depths for the three deployments (Table 3.1). The depth-normalised velocities overestimate the ADCP velocity near to the bottom. A possible cause for this local difference is that the deeper cell in the ADCP grid is closer to the bed than the one in the stretched grid, resulting in lower currents due to bottom friction.

3.2 Results

This section shows the results of the analyses carried out on the data sampled by the moored ADCP and C-T loggers on the three deployments: spring (1 Mar to 11 May 2001), summer (7 Aug to 26 Oct 2001) and winter (12 Dec 2001 to 8 Apr 2002).

Table 3.1: **M_2, M_4 and M_6 current amplitudes in ms^{-1} at three depths during the spring, summer and winter deployments. Bold numbers show amplitudes using data from the ADCP vertical coordinate and numbers in italic are from the depth-normalised grid data set. Proportional differences are shown in brackets.**

	M_2	M_4	M_6
spring			
surface	**0.336** *0.317* (5.6%)	**0.131** *0.121* (7.6%)	**0.113** *0.125* (10.6%)
mid-water	**0.274** *0.297* (8.4%)	**0.108** *0.115* (6.5%)	**0.117** *0.123* (7.9%)
bottom	**0.211** *0.229* (8.5%)	**0.093** *0.101* (8.6%)	**0.099** *0.110* (11.1%)
summer			
surface	**0.294** *0.310* (5.4%)	**0.120** *0.124* (3.3%)	**0.101** *0.113* (11.9%)
mid-water	**0.274** *0.298* (8.8%)	**0.116** *0.122* (3.4%)	**0.122** *0.115* (5.8%)
bottom	**0.237** *0.271* (14.4%)	**0.106** *0.115* (8.5%)	**0.107** *0.111* (3.7%)
winter			
surface	**0.311** *0.301* (9.7%)	**0.135** *0.119* (11.9%)	**0.135** *0.125* (7.4%)
mid-water	**0.283** *0.268* (5.3%)	**0.115** *0.110* (4.4%)	**0.124** *0.132* (6.5%)
bottom	**0.203** *0.214* (5.4%)	**0.100** *0.106* (6.0%)	**0.112** *0.120* (7.1%)

As well as the tidal variability, the gravitational circulation may also respond to wind stress, to changes in the longitudinal density gradient, and to remote forcing of the mean non-tidal surface slope in the estuary. Relevant meteorological data, longitudinal density gradient, sea surface slope and river discharge are therefore shown alongside. Initially the results from the deployments, in the context of spring-neap modulation of any apparent gravitational circulation, will be described. The possible cause-effect relationship behind relevant correlations with other physical parameters will be discussed further in section 3.3.

3.2.1 Spring mooring observations

The first deployment contained five spring-neap cycles shown in the time series of the near-bed tidal current velocity v_b (Fig. 3.4a), with three stronger neaps on days 64, 93 and 122 (maximum $v_b > 0.25$ m s^{-1}) and two weaker ones on days 78 and 107 (maximum $v_b < 0.15$ m s^{-1}). The variability of the near-surface $v_{o(s)}$ and near-bed $v_{o(b)}$ tidally-averaged currents (equation 3.1) shows sub-tidal bi-directional flow in three of the five neap tides (Fig. 3.4b) demonstrating the presence of mean current consistent with gravitational circulation (days 76-78, 92 and 105-110). Such enhanced gravitational circulation is not seen elsewhere in this data set. Intensification of the vertical density gradient was also recorded during the weaker current neap tides and a decrease of the stratification on spring tides (Fig. 3.4c). This spring-neap modulation of the bottom-surface density difference indicates the well-documented influence of the tidal mixing on the stratification (as in Nunes-Vaz et al. (1989), Peters (1997)). The wind stress was mainly towards the north quadrant during the deployment, with values below 0.2 $\mathrm{N\,m^{-2}}$, except for strong wind events around days 90-96 with surface stress up to 0.6 $\mathrm{N\,m^{-2}}$(Fig. 3.4d). The sub-tidal surface slope between the head and the mouth of the estuary varied between ± 0.05 m for the whole period, except for the persistent head-to-mouth slope observed between days 90 and 100 (Fig. 3.4e), reaching values above 0.1 m. This slope was associated with the strong wind from the mouth of the estuary. The longitudinal density gradient λ calculated for the ebb tides had a small variability with no spring-neap modulation (Fig. 3.4f). The mean λ for the whole deployment was $2.3 \times 10^{-4}\ \mathrm{kg\,m^{-4}}$.

A very weak bi-directional flow was observed on day 63 during the first neap, with an out-of-estuary flow at the surface ($v_{o(s)}$ = - 0.03 /ms) and an into-the-estuary flow at the bottom ($v_{o(b)} = 0.05\ \mathrm{m\,s^{-1}}$). Maximum values for the total near-bed velocity v_b within the semi-diurnal tidal cycles occurred at the ebb tides and were slightly above 0.35 $\mathrm{m\,s^{-1}}$. On day 64, $v_{o(s)}$ reversed direction, reaching 0.05 $\mathrm{m\,s^{-1}}$, and a rapid decrease in the bottom-surface density gradient also occurred. This may have been associated with the brief easterly/southeasterly winds with wind stress reaching 0.15 $\mathrm{N\,m^{-2}}$. This wind may have affected the mean circulation by moving the saltier coastal water into the estuary, as the surface salinity averaged over semi-diurnal cycles increased from 29 to 30.3.

A weak signal of a mean flow profile consistent with gravitational circulation was established on day 76 at the same time as an increase in the mean stratification. Calm weather conditions were dominant during this period with the wind stress lower than 0.04 $\mathrm{N\,m^{-2}}$ (Fig. 3.4d). Although there was no change in the wind, a sudden collapse of

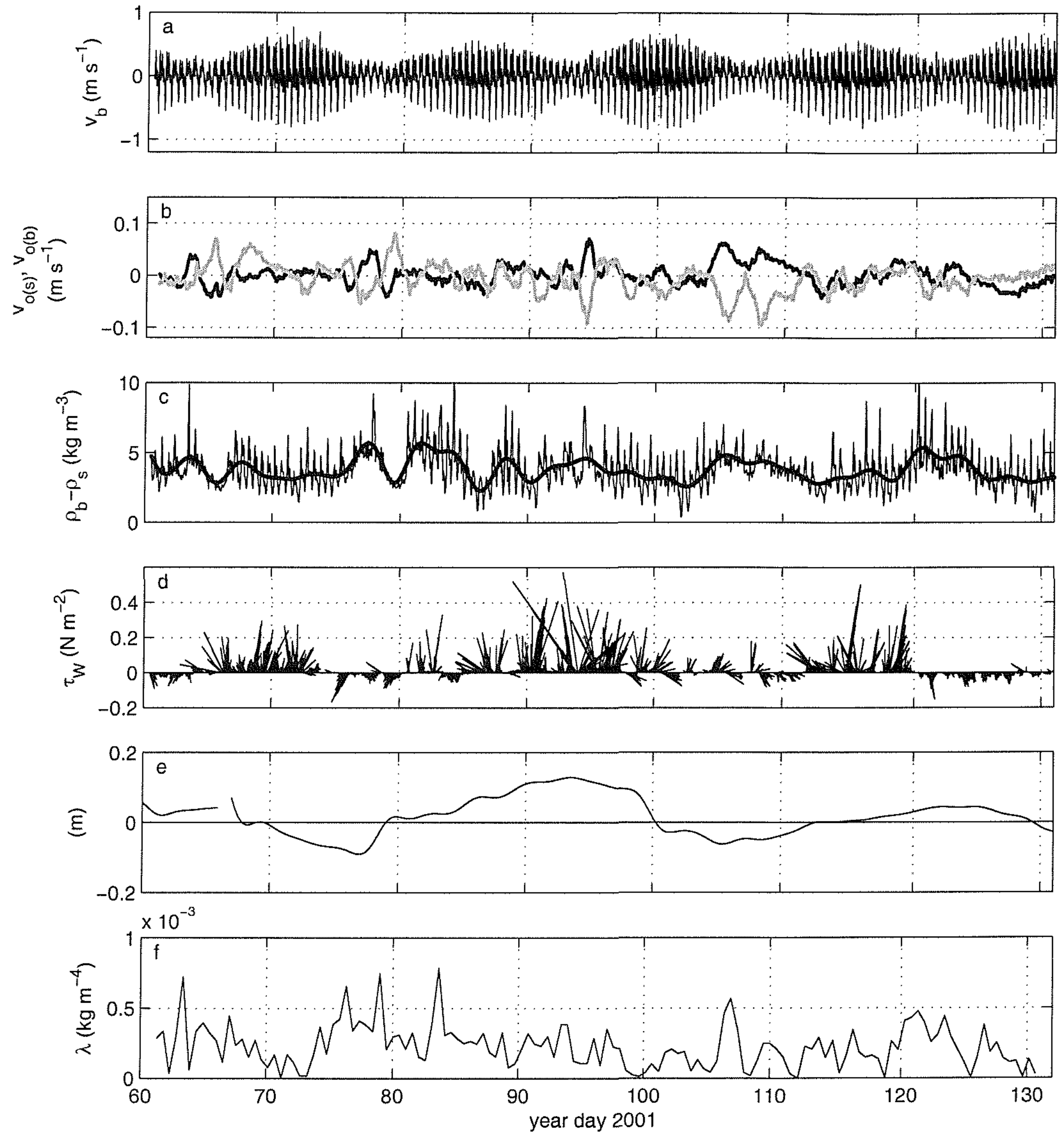

Figure 3.4: **Spring deployment time series of the (a) near bed velocity v_b; (b) hourly tidally-averaged velocity at surface ($v_{o(s)}$ - gray line) and bottom ($v_{o(b)}$ - black line); (c) 10-min (thin line) and 72 h- filtered (bold line) bottom-surface density difference; (d) hourly directional wind stress τ_W; (e) 72-h filtered head-to mouth surface slope; and (f) longitudinal density gradient λ calculated for ebb tides (kg m^{-4}). Positive values of velocity in (a) and (b) indicate into the estuary. τ_W vectors in (d) are aligned relative to north in the positive y-axis direction. Positive sea surface slope in (e) indicates higher water level at the head of the estuary (Dockhead gauge).**

the bi-directional net flow and consequent reduction of the stratification occurred on day 78. This prompt change in the sub-tidal flow appears to be related to the fall of the non-tidal water level in the estuary. This change of the sea surface level was associated with a high pressure system which caused an increase of 16 hPa in atmospheric pressure in less then 24 hours although no associated wind was observed. It also promoted a reversal of the sub-tidal barotropic gradient in the estuary, changing from a mouth-to-head to a head-to-mouth slope (see details in the Fig. 3.17).

The third neap tide (around day 94) had weak tidal currents with the maximum near-bed current velocity lower than 0.3 $\mathrm{m\,s^{-1}}$ from day 92 to day 95. A weak signal of the gravitational circulation-like mean flow was observed on day 92, but was shut down possibly in response to strong winds (τ_W up to 0.6 $\mathrm{N\,m^{-2}}$) from the southeast perhaps indicating the influence of wind-driven mixing on the mean flow. Wind subsequently acquired a very variable pattern, becoming weaker and perpendicular to the estuary on day 94, when the strong pulse of gravitational circulation occurred. An increase in the vertical density gradient was also observed. This pulse lasted for about one day, and finished when the near-bed current increased up to 0.4 $\mathrm{m\,s^{-1}}$. Winds rotated to be from southeast and may have contributed to the breakdown of this bi-directional gravitational circulation.

A well-established and persistent period of mean flow consistent with gravitational circulation was observed between days 104 and 111, the forth neap tide of the time series. The occurrence of weak winds at a time of low neap mixing would have been favourable to the onset and the long-lasting duration of this pulse. The vertical density gradient also increased during these days. The end of the bi-directional mean circulation coincided with the increase of the near-bed velocity ($v_b > 0.4$ $\mathrm{m\,s^{-1}}$), as tidal currents increased towards the next spring tide. At the same time a continuous decrease in the bottom-surface density difference was observed, indicating the effect of stronger tidal mixing. Winds remained unchanged and the sub-tidal surface slope remained constant for the whole period.

The last neap tide of this time series on day 123 was a strong neap with maximum near-bed velocity varying between 0.35 and 0.45 $\mathrm{m\,s^{-1}}$ at the ebb tides. Two weak signals of bi-directional circulation were possibly observed on days 121 and 123 although the surface and bottom tidally-averaged velocities were very low ($\approx |0.02|\ \mathrm{m\,s^{-1}}$) comparing to the standard deviation of the ADCP measurements ($\pm 0.01\ \mathrm{m\,s^{-1}}$). Nevertheless, an increase in stratification was observed, with the bottom-surface density difference rising from below 3 to 5 $\mathrm{kg\,m^{-3}}$ on these days and decreasing again to 3.5 $\mathrm{kg\,m^{-3}}$ on day 126. Wind stress was below 0.08 $\mathrm{N\,m^{-2}}$ during this neap tide, except on day 121 with $\tau_W = 0.15\ \mathrm{N\,m^{-2}}$ from the north.

Figure 3.5 shows the time series of the tidally-averaged main-axis velocity v_o calculated for the different levels of the depth-normalised grid.

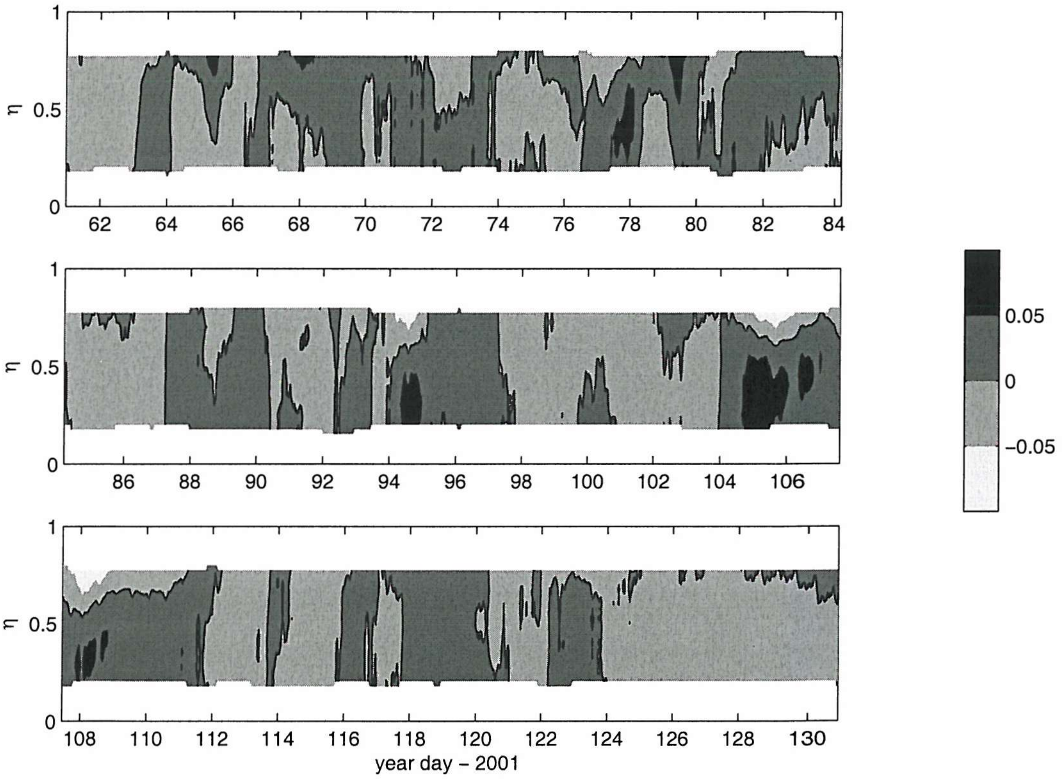

Figure 3.5: **Depth normalised time series of the tidally-averaged velocity v_o, in $\mathrm{m\,s^{-1}}$, during the spring deployment.**

3.2.2 Summer mooring observations

The second deployment included 6 spring-neap cycles over 80 days (Fig. 3.6a). Small gaps in the bed velocity v_b time series are due to the ADCP reading failures between days 227 and 244, and on day 267 (see section 2.1.1). The time series of the near-surface $v_{o(s)}$ and near-bed $v_{o(b)}$ tidally-averaged currents (equation 3.1) show a weak mean flow with values above $|0.03|$ $\mathrm{m\,s^{-1}}$ only for 8% of this deployment through the whole water column. Except possibly for a short pulse on the last neap tide around day 297 the bi-directional non-tidal current presented no spring-neap modulation during this deployment (Fig. 3.6b).

The absence of the spring-neap modulation cannot be justified by increases in the tidal- or wind-induced mixing compared to the spring deployment described before. Maximum near-bed currents within a semi-diurnal tidal cycle were lower than 0.4 $\mathrm{m\,s^{-1}}$ at all neap tides, which would result in weaker tidal-induced vertical mixing. Wind mixing was also weak as wind stress remained mostly similar to those of the spring deployment, apart from day 273 to day 282 when it reached values well above 0.3 $\mathrm{N\,m^{-2}}$ (Fig. 3.6c). This strong wind from the south possibly caused the observed rise in the water surface from 0.1 metre above the mean sea level on day 272 to 0.4 metre on day 280 (Fig. 3.6d). Time series of the head-to-mouth sea level difference presented no significant changes in sub-tidal time scales (not shown).

The only probable event of gravitational circulation started on day 296.5. The surface tidally-averaged velocity $v_{o(s)}$ was greater than 0.05 $\mathrm{m\,s^{-1}}$ during the following 2 days, although $v_{o(b)}$ was lower then 0.04 $\mathrm{m\,s^{-1}}$. During these days near-bed current v_b was below 0.35 $\mathrm{m\,s^{-1}}$ at the peak of the ebb tides and wind speed ranged from 4 to 8 $\mathrm{m\,s^{-1}}$. After day 298.5 wind speed increased to above 10 $\mathrm{m\,s^{-1}}$ ($\tau_W > 0.25$ $\mathrm{N\,m^{-2}}$) from the mouth of the estuary at the same time as the event finished. Tidal mixing remained low with $v_b < 0.25$ $\mathrm{m\,s^{-1}}$ until the end of the deployment on day 299.4.

The River Test discharge reached the lowest values of the period covered by the three deployments in mid-September being less than 7 $\mathrm{m^3\,s^{-1}}$ from day 250 to day 272 (Fig. 2.10 in the section 2.1.2). Time series of the 25-h running window averaged surface

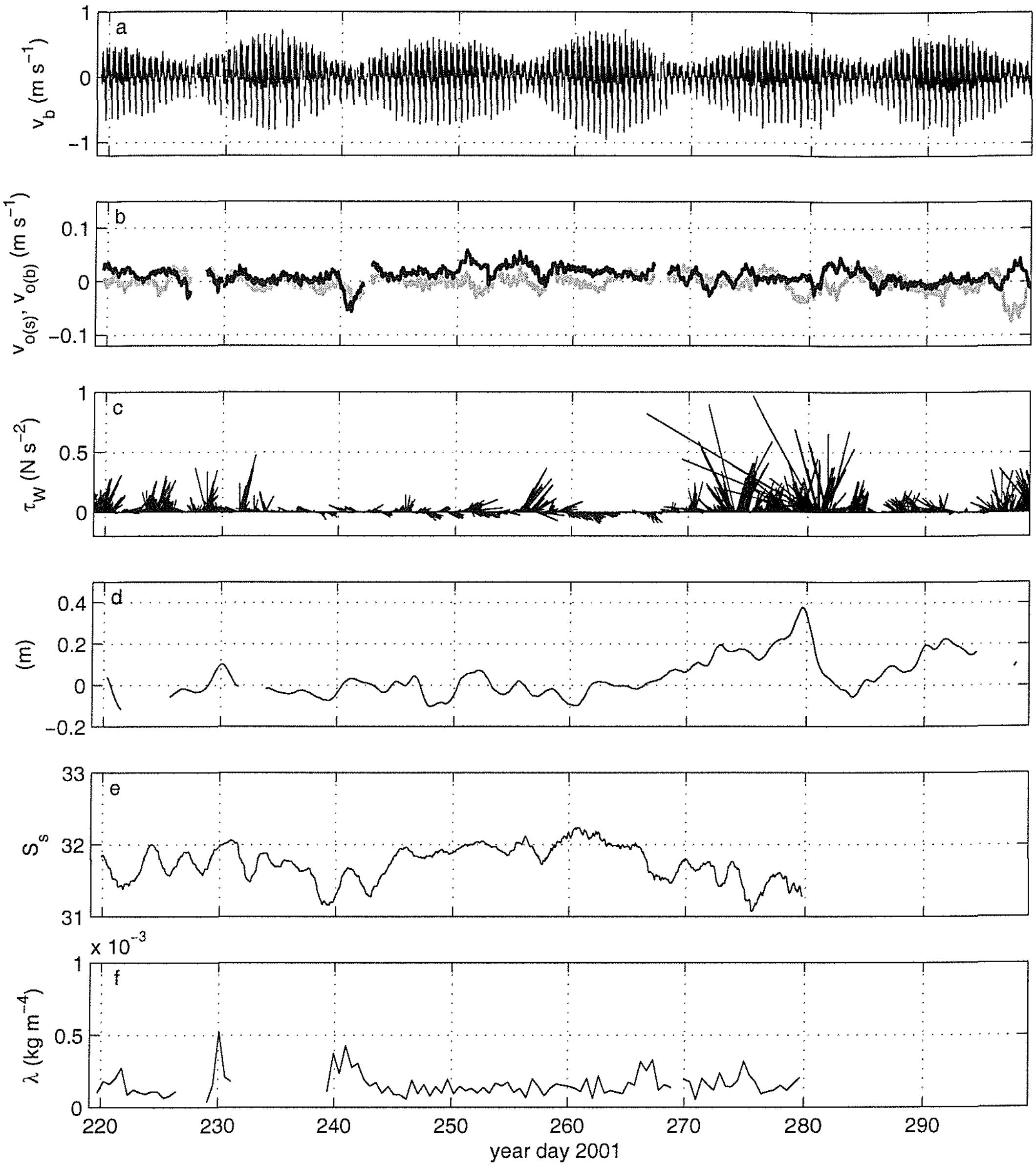

Figure 3.6: Summer deployment time series of the (a) near bed velocity v_b; (b) hourly tidally-averaged velocity at surface ($v_{o(s)}$ - gray line) and bottom ($v_{o(b)}$ - black line); (c) hourly directional wind stress τ_W; (d) 72-h filtered surface level at the head of the estuary (Dockhead), relative to the mean sea level; (e) 25-h running window average of the surface salinity S_s; and (f) longitudinal density gradient λ calculated for ebb tides (kg m^{-4}). Positive values of velocity in (a) and (b) indicate an into-the-estuary flow. τ_W vectors in (c) are aligned relative to north in the positive y-axis direction.

salinity showed slightly higher salinity during this period of low river discharge, rising from 31.3 on day 243 to 32.2 on day 260 (Fig. 3.6e) to decrease from 32.0 on day 267 to 31.3 at the end of the surface C-T logger time series on day 280. Stratification could not be accessed due to the lack of confidence in the calibration of the near-bed salinity (see section 2.1.1).

The longitudinal density gradient calculated for the summer deployment was lower than the one for the spring deployment, with the average±standard deviation of 1.5±0.8 $\times$ 10^{-4} kg m^{-4}. Values were seldom higher then 2 $\times$ 10^{-4} kg m^{-4} and stayed lower then 1 $\times$ 10^{-4} kg m^{-4} between days 245 and 265 (Fig. 3.6f). The early end of the λ time series in the summer deployment was due to the lack of surface density measurements after day 280, and the small gaps at the beginning of the time series were caused by bad ADCP data (see section 2.1.1). The lower freshwater input was most likely the cause of the weaker density gradient observed in this deployment.

It seems likely that the absence of bi-directional mean flow at the mooring site was closely related to the low freshwater input. The longitudinal density gradient during this period of low river discharge was the weakest in comparison to the rest of the period analysed over the three deployments. This suggests that the density gradient was not strong enough to induce the formation of enhanced gravitational circulation in the presence of even the weakest tidal mixing, at least in the mid-part of the estuary.

Figure 3.7 shows the time series of the tidally-averaged main-axis velocity v_o calculated for the different levels of the depth-normalised grid.

3.2.3 Winter mooring observations

This was the longest mooring deployment, covering 8 spring-neap tidal cycles (Fig. 3.8a). The two possible long events of gravitational circulation around day 358 and day 417 were associated with weak neap tides (Fig. 3.8b). Two distinctive wind conditions characterised this deployment. Weaker winds dominated the first 40 days while stronger wind occurred more frequently during the following weeks, particularly

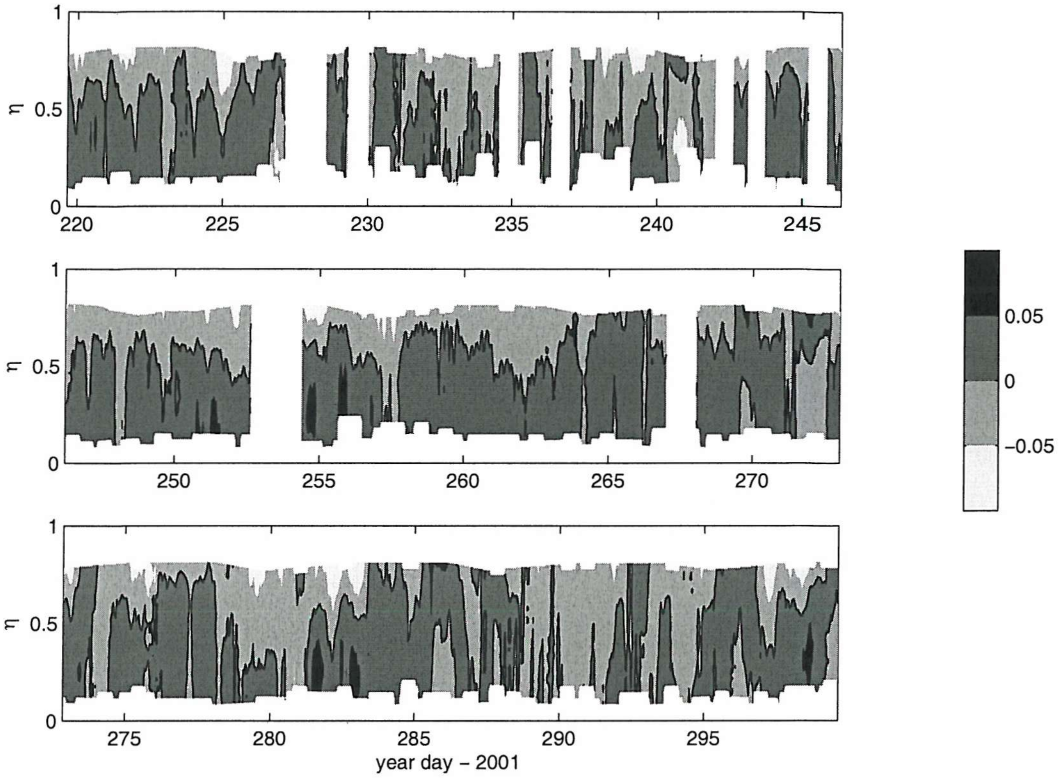

Figure 3.7: **Depth normalised time series of the tidally-averaged velocity v_o, in $\mathrm{m\,s^{-1}}$, during the summer deployment.**

between days 385 and 425 (Fig. 3.8c).

The strong pulse of non-tidal flow during the first neap tide, from day 355 to day 360, showed possible effects of both tidal- and wind- induced mixing in the control of gravitational circulation. The bottom-surface difference of the tidally-averaged velocity, $v_{o(b)} - v_{o(s)}$, was around 0.08 $\mathrm{m\,s^{-1}}$ during these days, except on day 358 when it decreased to around 0.04 $\mathrm{m\,s^{-1}}$ for 12 hours at the same time as stronger winds from the southwest ($\tau_W > 0.2$ $\mathrm{N\,m^{-2}}$). The end of this event on day 360 may be associated with the intensification of the tidal currents toward the next spring tide. Despite the presence of weak winds, tidal mixing was strong enough to prevent any gravitational flow for the next 27 days after day 360. The maximum near-bed currents were above 0.5 $\mathrm{m\,s^{-1}}$ at the neap tide within this period on day 373.

Wind was strong for three weeks after day 384. This wind, mostly from the

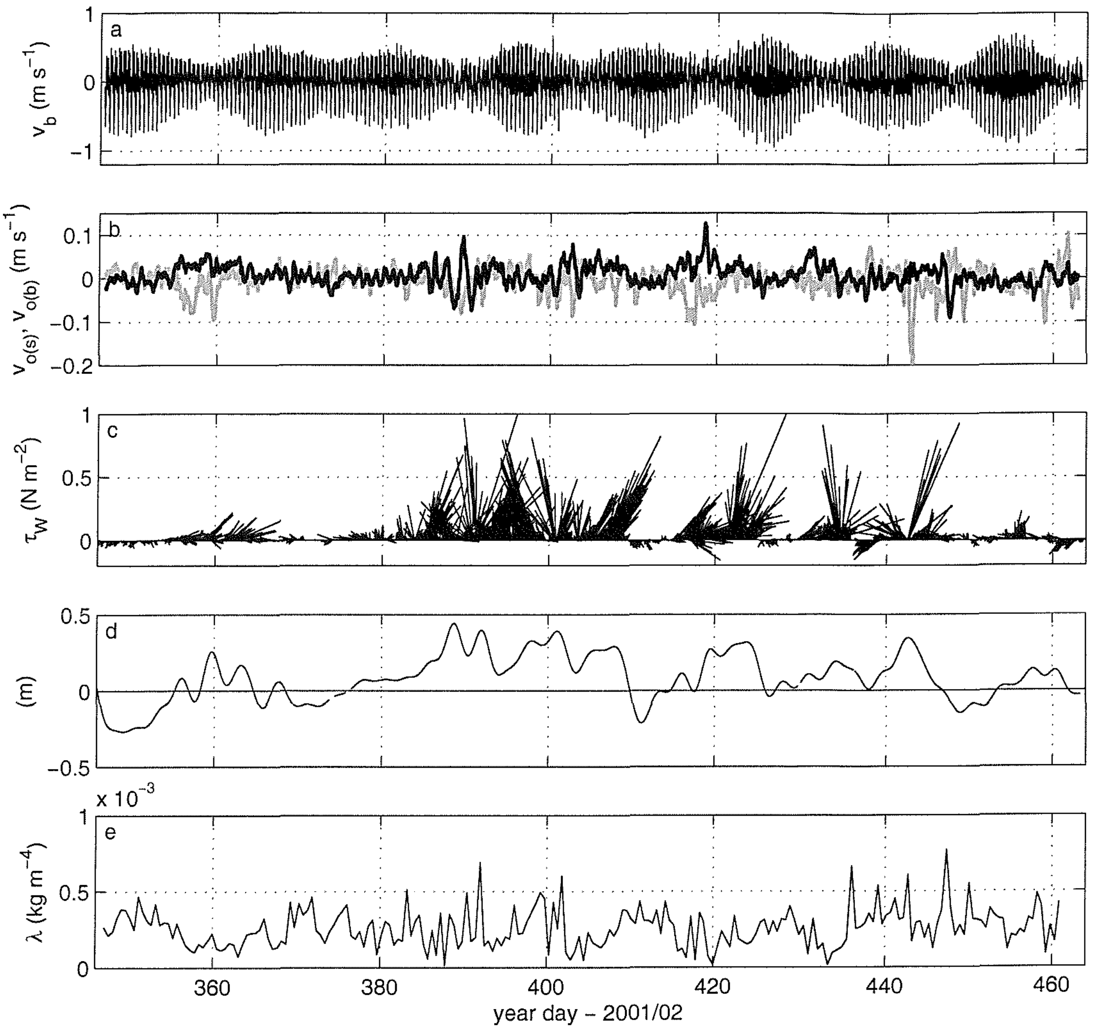

Figure 3.8: **Winter deployment time series of the (a) near bed velocity v_b; (b) hourly tidally-averaged velocity at surface ($v_{o(s)}$ - gray line) and bottom ($v_{o(b)}$ - black line); (c) hourly directional wind stress τ_W; (d) 72-h filtered surface level at the head of the estuary (Dockhead), relative to the mean sea level; and (e) longitudinal density gradient λ calculated for ebb tides (kg m^{-4}). Positive values of velocity in (a) and (b) indicate flow into the estuary. Wind stress vectors in (c) are aligned relative to north in the positive y-axis direction.**

south quadrant, was the strongest observed during the period of study. Fluctuations of this strong wind possibly caused the highly variable tidally-averaged current observed between days 384 and 410. Rises of 0.3-0.4 m of the non-tidal sea surface level in the head of the estuary were associated to this onshore wind (Fig. 3.8d) and potentially could have affected the mean flow.

A strong but highly variable bi-directional sub-tidal flow was present from day 417 to day 420. Wind speed was also highly variable during this period with the direction to varying between the northwest and the southwest. The variability observed in the sub-tidal flow appears to be related to the changes in the strength and direction of the wind. The suppression of the gravitational circulation on day 420 may have been associated with the strengthening of the tidal currents ($u_b > 0.4$ m s^{-1}) while the winds remained weak with $\tau_W < 0.2$ N m^{-2}.

Combined tidal- and wind-driven vertical mixing may have interfered with the development of the gravitational circulation around the sixth neap (day 433). Maximum semi-diurnal near-bed ebb current was above 0.4 m s^{-1}. Wind speed varied from 12 to 19 m s^{-1} (τ_W up to 1 N m^{-2}) between days 432 and 436 although mostly perpendicular to the estuary.

A strong seaward pulse of the non-tidal surface current ($v_{o(s)} >$ -0.2 m s^{-1}) was present on day 443, although the bottom current $v_{o(b)}$ was lower than 0.05 m s^{-1}. This surface pulse can be associated with the relaxation of the barotropic pressure gradient related to an increase of the water surface level in the estuary up to 0.35 m above the mean sea level. This rise of the water surface was present at both tidal gauges and was possibly caused by the strong wind from the south quadrant combined with a fall of the local atmospheric pressure. This mechanism is detailed further on in section 3.3.2 (see Fig. 3.16).

The longitudinal density gradient λ varied mostly between 1 and 5 $\times$ 10^{-4} kg m^{-4}, with an average of 2.5 $\times$ 10^{-4} kg m^{-4} which was similar to the one calculated for the spring deployment. The only signal of spring-neap variability of λ in this study was observed between days 402 and 432 when it was slightly lower at the neaps comparing to the following springs (Fig. 3.8e).

Figure 3.9 shows the time series of the tidally-averaged main-axis velocity v_o calculated for the different levels of the depth-normalised grid.

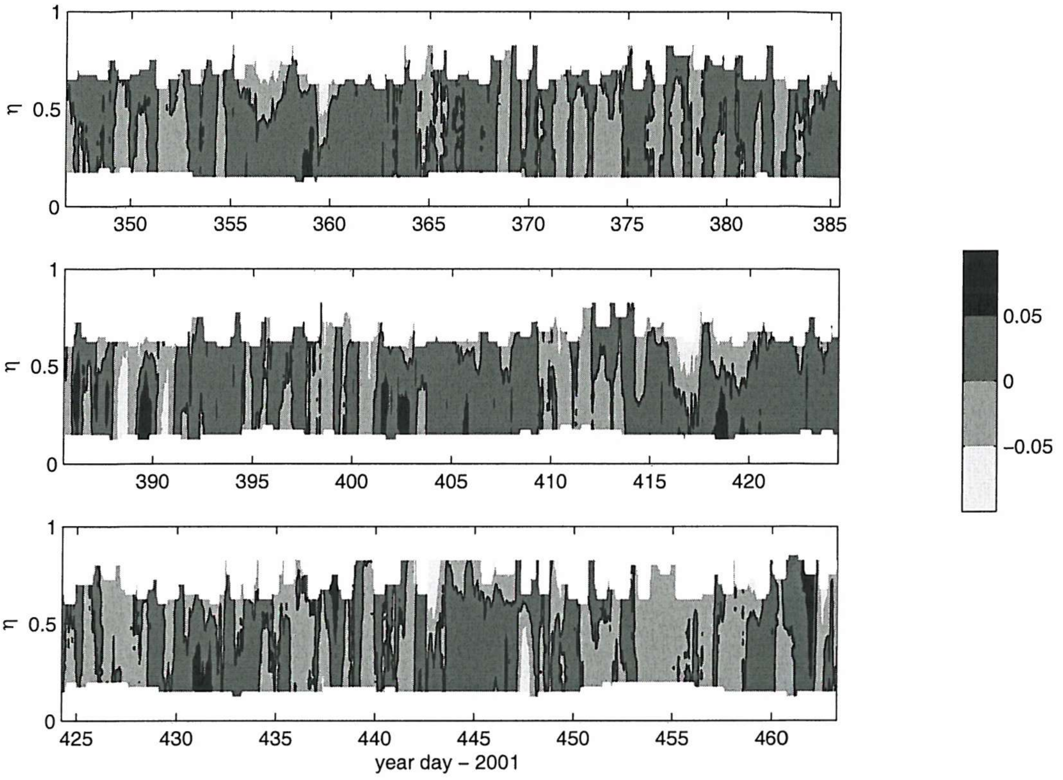

Figure 3.9: **Depth normalised time series of the tidally-averaged velocity v_o, in m s^{-1}, during the winter deployment.**

3.3 Discussion

The control of the spring-neap variability of tidal mixing on the gravitational circulation in Southampton Water is discussed in this section. However other processes which occur in the estuary may affect the mean flow and alter the spring-neap modulation. Results have shown some evidence that wind stress can be important in changing the behaviour of the mean flow. Another meteorological process discussed is the variation of the atmospheric pressure. The seasonality of the freshwater discharge from the rivers may also have played a role in controlling the strength of the gravitational circulation.

3.3.1 The spring-neap modulation

All pulses of gravitational circulation observed during these long time series occurred at neap tides, and notably the weaker the neap current, the stronger the bidirectional circulation. The close relation between tidal-induced mixing and the bidirectional mean flow on days 104-111 (spring deployment) can be well observed during the transition of tidal current strength from higher at spring to lower at neap and back to the spring higher currents (Fig. 3.10a). This long event occurred under persistent low wind conditions, with wind stress lower than 0.05 $\mathrm{N\,m^{-2}}$ (wind speed < 5 $\mathrm{m\,s^{-1}}$) mainly from the west quadrant (Fig. 3.10b), except for the short peaks of $\tau_W > 0.1$ $\mathrm{N\,m^{-2}}$ on days 104 and 107. Persistent weak winds on these days allowed the best example for illustrating the response of the gravitational circulation to long term (spring-neap time scales) changes in tidal mixing.

Stratification increased between days 102 and 104, before the main event of gravitational circulation started. The 72-h filtered bottom-surface density difference rose from 2.6 to 4.3 $\mathrm{kg\,m^{-3}}$(Fig. 3.10d) as density increased at the bottom (from 1024.6 to 1025.5 $\mathrm{kg\,m^{-3}}$) and decreased at the surface (from 1022.0 to 1021.2 $\mathrm{kg\,m^{-3}}$). This may indicate that the increasing stratification during the spring-neap transition was probably caused by lower tidal mixing as the tidal currents became weaker towards the neap. Higher stratification also may damp the boundary mixing by inhibiting the vertical mixing through the water column, leading ultimately to an even stronger stratification. This feedback process was shown by Peters (1999) in the Hudson River. The more efficient damping of the turbulent mixing due to the increasing stratification, combined with the reduction of the tidal currents toward the neap tide, could have led to the onset of the gravitational circulation on day 104.

A simple calculation of the mean density-driven velocity can be applied to the formation of the gravitational circulation by using equation 2.8. Taking the change in the surface density between days 102 and 104 and dividing by the averaged longitudinal density gradient of 1.5×10^{-4} $\mathrm{kg\,m^{-4}}$ over those days (Fig. 3.4), the mean surface velocity is 0.073 $\mathrm{m\,s^{-1}}$. The same procedure can be applied for estimating a bottom mean velocity

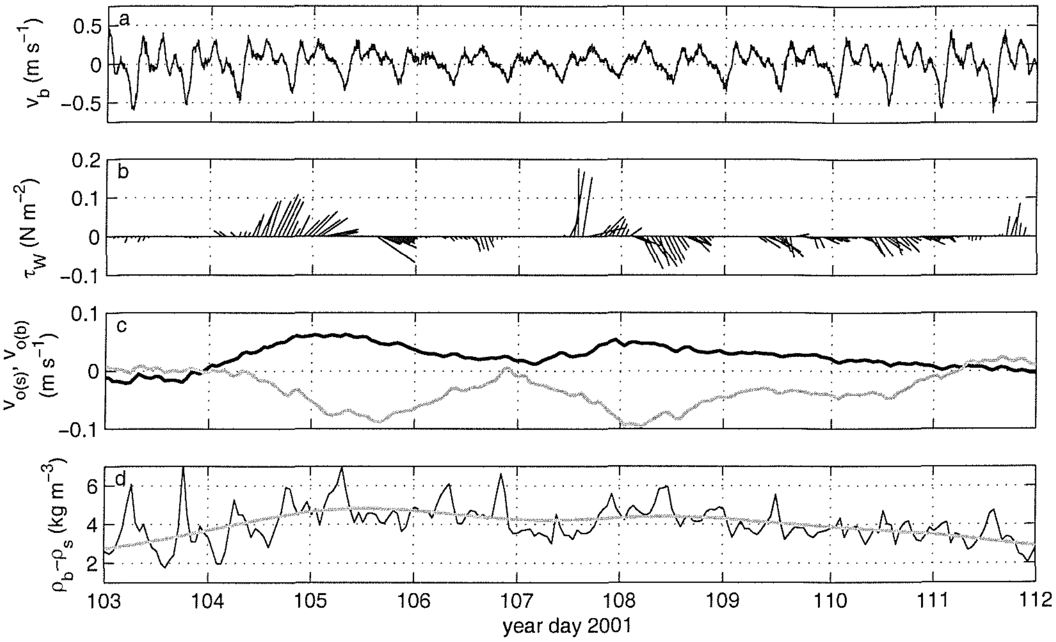

Figure 3.10: **Time series of (a) near bed velocity v_b; (b) hourly directional wind stress τ_W; (c) hourly tidally-averaged velocity at surface ($v_{o(s)}$ - dotted line) and bottom ($v_{o(b)}$ - bold line); and (d) hourly-averaged (black line) and 72-h filtered (gray line) bottom-surface density difference for the spring-neap transition between the year days 102 and 112. Wind stress vectors in (b) are aligned relative to north in the positive y-axis direction. Neap tide is on day 107.**

of 0.052 m s^{-1} using an averaged bottom $\lambda = 0.9 \times 10^{-4}$ kg m^{-4} (not shown). These velocities are in agreement with the surface and bottom velocities of the mean flow profile on day 105 (Fig. 3.11).

Knowing the local density gradient and the averaged vertical profile of the non-tidal flow during this event, it is possible to make a direct comparison with the theoretical prediction of the presented by Hansen and Rattray (1965) (equation 1.7). A least squares fit of the observed mean velocity profile (on the normalised vertical coordinates) to the Hansen-Rattray solution provides the best fit at an eddy viscosity N_z of 1.2×10^{-3} m^2 s^{-1}. Comparing the Hansen-Rattray profile with the observations of the tidally-averaged current profile it is possible to confirm the presence of the gravitational circulation in Southampton Water during extended periods of weak mixing (Fig. 3.11). This value ($N_z = 1.2 \times 10^{-3}$ m^2 s^{-1}) represents a typical low mixing period, acting anal-

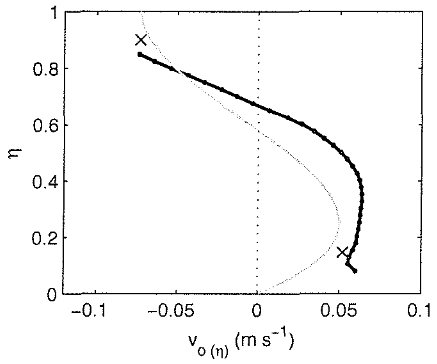

Figure 3.11: **Vertical profile of the averaged tidally-averaged velocity $v_{o(\eta)}$ over day 105 (black line with dots); and the Hansen-Rattray profile calculated by equation 1.7 with $\lambda = 1.5 \times 10^{-4}$ kg m^{-4} and $N_z = 1.2 \times 10^{-3}$ m^2 s^{-1} (gray line) for a better fit. The x's are the currents obtained from the variation in the density field (equation 2.8). The normalised depth η is zero at the bottom and seaward velocities are negative.**

ogously as a background value. It was also noticed that shear in the interior of the water column is stronger and higher up in the data compared to the theory. This deviation may be a result of a sharper stratification at the upper half of the water column.

The strength of the gravitational circulation during a semi-diurnal cycle can be quantified by the tidally-averaged shear velocity, v_g, equal to $\overline{(v_{o(b)} - v_{o(s)})}$, with $v_{o(b)}$ and $v_{o(s)}$ being the bottom and the surface tidally-averaged velocity, respectively. The overbar represents the average over each single semi-diurnal tidal cycle. The concept of some critical tidal current speed, below which the gravitational circulation accelerates, can be investigated by relating v_g with the maximum near-bed current $v_{b(Emax)}$ over a semi-diurnal cycle at the ebb tide (Fig. 3.12).

Looking at data from spring and winter deployments vg above 0.06 m s^{-1}are only present during tidal cycles of currents weaker than 0.5 m s^{-1}. It suggests a limit of tidal current below which the tidal mixing is reduced enough to permit acceleration of the gravitational circulation. This finding is corroborated by the results of the Hansen-Rattray solution (equation 1.7) applied to a N_z proportional to the bed current ($N_z \propto hv_b$). The only exception observed during the deployments is the extremely strong surface outflow (shown as a circle in Fig. 3.12b) on day 443 caused by relaxation of a wind-induced slope in the sea level (see section 3.3.2). This point has been excluded from the results of the linear regression and correlation index presented for the series of values of gravitational circulation (dot marks).

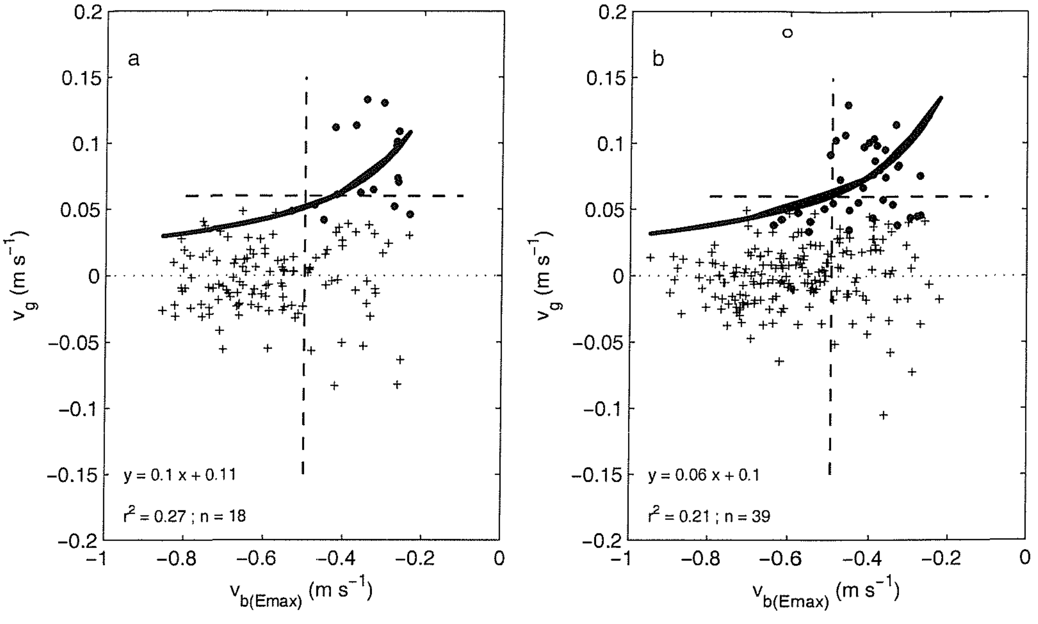

Figure 3.12: **Mean shear velocity v_g plotted with the maximum ebb bottom velocity $v_{b(Emax)}$, averaged over the semi-diurnal tidal cycles for the (a) spring (136 semi-diurnal tidal cycles) and (b) winter (225 semi-diurnal tidal cycles) deployments. The dashed lines show the ebb velocity limit of 0.5 m s^{-1} and the v_g limit of 0.06 m s^{-1}. Solid dots show tidal cycles under condition of gravitational flow and crosses mark non-gravitational circulation. Thick lines show the result of the Hansen-Rattray profile from equation 1.7. Linear regression and correlation were calculated for the n points under gravitational circulation regime marked with dots. The circle in (b) is the extreme event of high tidally-averaged surface velocity on day 443 and was excluded from the calculations.**

However, tidal mixing is not the only source of mixing that might prevent gravitational circulation. A reduction of the peak ebb current flow below 0.5 m s^{-1} will most likely be a necessary, but not a sufficient, condition for acceleration of the density-driven currents. The fact that of some of the tidal cycles with no significant event of gravitational circulation ($v_g < 0.06$ m s^{-1}) had low tidal-driven mixing (tidal current $v_{b(Emax)}$ below 0.5 m s^{-1}) supports this. Effects of the wind mixing on the spring-neap modulation of the gravitational circulation were observed and will be discussed in the following section. Note that due to the absence of gravitational circulation during most of the time of the second deployment, results from this time series are not shown.

The results presented and discussed in this section have showed that the spring-neap fluctuation of the tidal currents have a significant control on the gravitational circulation. Events of bi-directional density-driven flow were associated with the decrease on the tidal mixing during the low current neap tides. The link between the gravitational circulation and the turbulent mixing has been approached using different techniques (e.g. the theoretical study of Nunes-Vaz et al. (1989), the laboratory experiments of Linden and Simpson (1986) and modelling work in Liverpool Bay by Sharples and Simpson (1995)). This relation was inferred from results of principal component analysis done by Stacey et al. (2001), who also indicated that enhanced gravitational circulation is dependent not only on the reduction in the strength of the tidal mixing, but also on the horizontal density gradient. The Southampton Water data can now be analysed in a similar way.

The horizontal Richardson number

The reduction of the tidal mixing below some critical rate is unlikely to be a sufficient criterion for the onset of pulses of gravitational circulation. The presence of the longitudinal density gradient is the pre-condition for the development of the gravitational flow. Stacey et al. (2001) summarise the two groups of tidally-induced mechanisms which can create the gravitational circulation: (1) the baroclinic pressure gradient generated by the density difference along the estuary (section 1.2), and (2) the ebb-flood barotropic-related tidal asymmetry (section 1.3). The authors argue that the stratification-destratification following the tidal straining is an important factor in controlling vertical mixing. And, for their observations, gravitational circulation is more likely to be resulted of barotropic controlled periodic stratification than baroclinic relaxation of the longitudinal density gradient.

Sharples and Simpson (1993) used a numerical model to suggest that the development of neap tide frontogenesis in the Liverpool Bay region of freshwater influence may require an increase of the stratification acting as a trigger factor, as well as the reduction in mixing. In other words, the system needs some stable precondition before the gravitational circulation could develop. The reduction in mixing can permit an increase of the stratification, which allows further enhancement of the gravitational circulation as feedback. A detailed analysis of observations from San Francisco Bay by Stacey et al. (2001) showed that the typical changes in the gravitational circulation were greater than could be justified solely on the basis of spring-neap variability in tidal mixing. To some extent this appears to be the case in the Southampton Water data, where the mean stratification increased approaching neap tides before the pulse of enhanced gravitational circulation became established.

Stacey et al. (2001) defined a horizontal Richardson number,

$$Ri_x = \frac{g\lambda\frac{1}{\rho}H^2}{u_*^2} \tag{3.2}$$

with H the water depth, λ the longitudinal density gradient, and u_* the friction velocity, estimated from

$$u_* = k_b v_b^2 \tag{3.3}$$

with k_b the dimensionless bottom drag coefficient equal to 3×10^{-3}. The horizontal Richardson number effectively describes the processes controlling ebb-tide straining-induced periodic stratification (SIPS, Simpson et al. (1990)). On the spring-neap time scale Ri_x was seen to have a critical value of 3 (Stacey et al., 2001), above which the gravitational circulation was able to develop.

By combining equation 3.2 and the u_* data sets with the averaged λ for each of the deployments, the horizontal Richardson number could be calculated for Southampton Water. The observed neap increase in the gravitational circulation also required a critical value of Ri_x to be exceeded (Fig. 3.13), though the critical value may be slightly higher than that suggested by Stacey et al. (2001) ($Ri_x = 3$). Above this threshold a feedback effect between stratification and tidal mixing may be created, resulting in pre-condition for the observation of pulses of gravitational circulation.

The decrease in Ri_x during the summer, with top values remaining above the stratification threshold only at one neap (day 269), reflects the lower longitudinal density

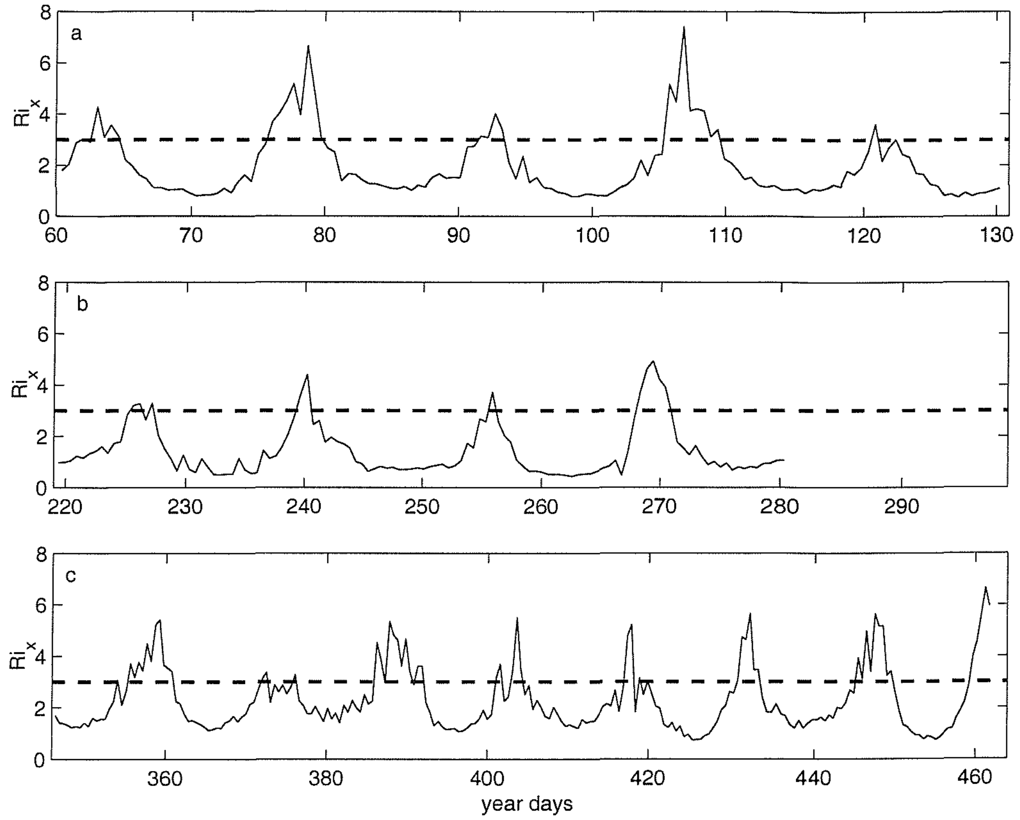

Figure 3.13: **Time series of the horizontal Richardson number Ri_x for (a) spring, (b) summer and (c) winter deployments. The dashed line indicates the limit of $Ri_x = 3$ proposed by Stacey et al. (2001).**

gradient caused by the reduced riverine freshwater input. Wind stress does not have any influence on the Ri_x estimates, however the important role of the strength and the direction of the wind in the occurrence and duration of those events has been already suggested and will be discussed below.

3.3.2 Meteorological effects on the spring-neap modulation of gravitational circulation

The principal meteorological mechanism which affects the spring-neap modulation of the gravitational mean flow is the wind stress on the surface of the estuary. Rainfall also acts on the mean flow as the riverine freshwater input controls the horizonal density gradient. The effects of the variation of this density gradient on the gravitational circulation are discussed later in this chapter (section 3.3.3). In addition to the wind effects the control of the atmospheric pressure variability on the mean flow may have been observed on one occasion.

Wind-induced effects on the gravitational circulation

The effects of the turbulent vertical mixing generated by the wind stress on the gravitational circulation has already been suggested in other studies (Nunes and Lennon, 1987, Kreeke and Robaczewska, 1989, Simpson et al., 1993, Sharples and Simpson, 1995) and were observed in Southampton Water. Reductions in the strength of the well-developed pulses of the mean flow were associated with the intensification of the wind speed, W, on day 358 (W from 4 to 10 $\mathrm{m\,s^{-1}}$) and 418 (W from 4 to 9 $\mathrm{m\,s^{-1}}$) (Fig. 3.8). Short pulses of the gravitational circulation were also associated with short periods of weak winds during generally strong wind events (e.g. days 94, 389 and 403 - Figs. 3.4 and 3.8). All of these observations of the influence of the wind on the gravitational circulation were made under low tidal-induced mixing periods at neap tides, with the maximum tidal currents over a semi-diurnal cycle being lower than 0.4 $\mathrm{m\,s^{-1}}$.

The influence of the speed and direction of the wind on the gravitational flow can be investigated by applying the simple analysis for the effects of tidal mixing shown in Fig. 3.12. Only the first (Fig. 3.14a,b) and third deployments (Fig. 3.14c,d) are shown due to the absence of gravitational circulation events during most of the time of the second deployment. Wind direction has been grouped by each of the 90° quadrants (i.e. NE quadrant from north to east, etc.). Winds to both the northeast and southwest quadrant were considered transversal to the estuary and to the northwest and the southeast were named as parallel, from the mouth and from the head of the estuary, respectively (Fig. 3.14a,c). Wind magnitude was grouped according to the speed (Fig. 3.14b,d). Events of gravitational circulation, mostly indicated by $v_g > 0.06$ $\mathrm{m\,s^{-1}}$ are in the top right of the figures (see also Fig. 3.12). Those events occurred mostly during transverse winds (Fig. 3.14a,c), generally when wind speed was below 8 $\mathrm{m\,s^{-1}}$ (Fig. 3.14b,d).

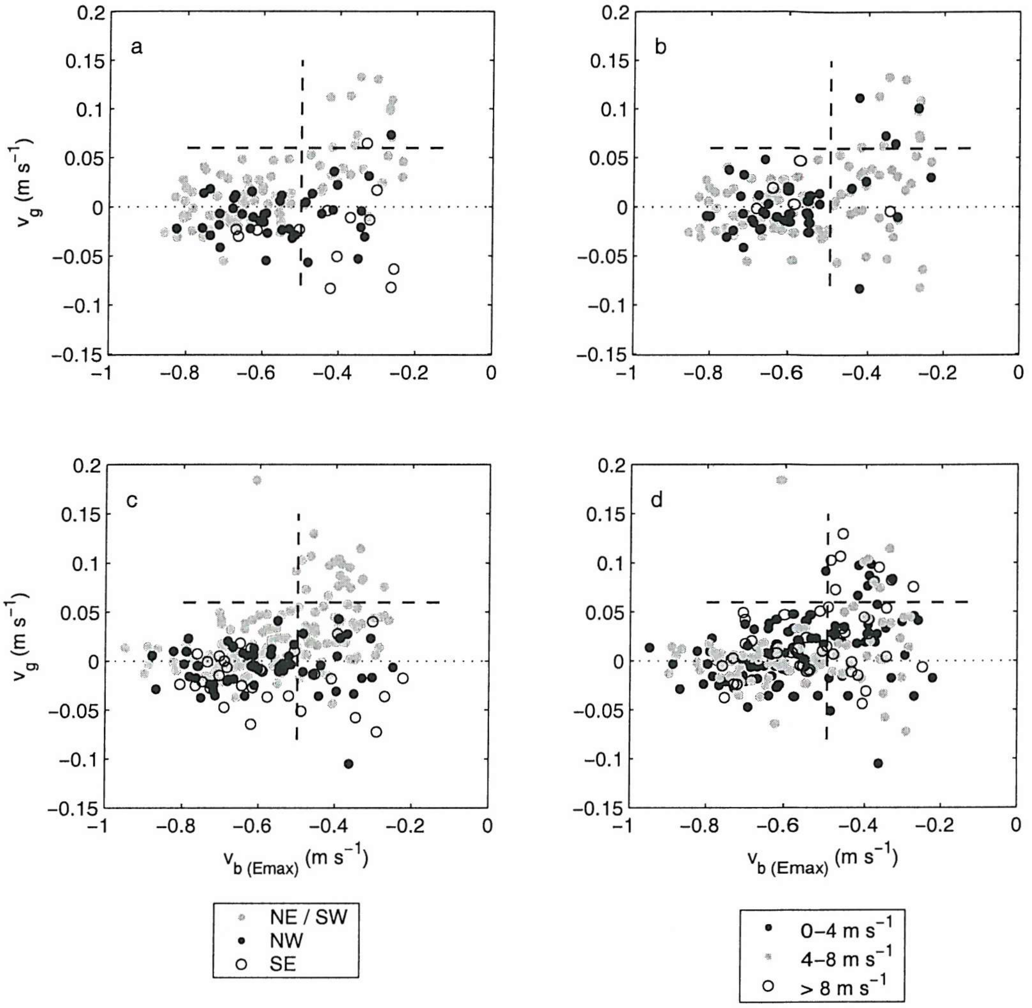

Figure 3.14: **Semi-diurnal mean shear velocity v_g and the maximum ebb velocity $v_{b\,(Emax)}$, plotted with different wind speeds and directions for the spring (a and b) and winter (c and d) deployments. The direction of the wind (a and c) are grouped as transverse to the estuary (NE and SW - gray dots), to the head (NW - black dots) and to the mouth (SE - circles) of the estuary. Wind speed (b and d) are grouped between 0 and 4 m s^{-1} (black dots), 4 and 8 m s^{-1} (gray dots) and above 8 m s^{-1} (circles). The dashed lines show the limit for v_g, which above is region of the gravitational flow (> 0.06 m s^{-1}), and for $v_{b\,(Emax)}$, which tidal mixing is low enough to permit the gravitational flow (< 0.5 m s^{-1}), as discussed in the previous section.**

In addition to this, wind induces water movement to the same direction, with along-estuary winds either aiding (offshore winds to SE) or hindering (onshore winds to NW) the surface component of the gravitational flow, $v_{o(s)}$ (Fig. 3.15a,b). The effects of the parallel wind stress on the surface layer are observed on the gravitational flow as well (Fig. 3.15c,d). Points of strong onshore winds mostly cause positive $v_{o(s)}$ (i.e. into the estuary), resulting in a weak but inverse gravitational circulation. On the other hand, offshore winds may drag water seaward, aiding to enhance the gravitational circulation surface outflow.

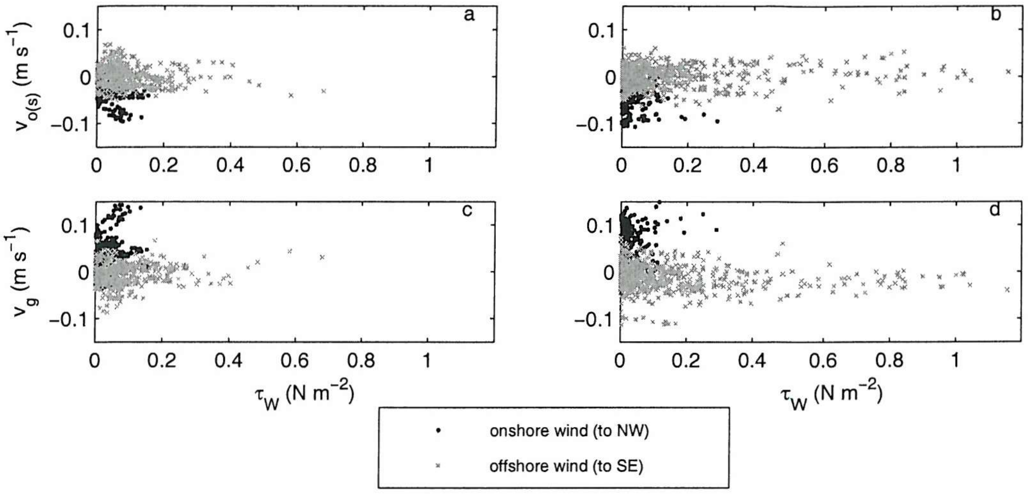

Figure 3.15: **Hourly mean wind stress τ_W for the along-estuary directions (the SE and NW quadrants) versus the hourly surface tidally averaged velocity $v_{o(s)}$ (a and b) and the hourly mean shear velocity v_g (c and d), for the (a and c) spring (918 points) and (b and d) winter (1141 points) deployments. Black dots are onshore winds (to the northwest) and gray crosses show southeasterly offshore winds.**

Strong onshore northwestward winds were not present when v_g was above 0.06 m s^{-1}. Such onshore winds would be associated with a reduction in the surface mean flow (and subsequent stratification) by moving saltier water into the surface of the estuary in addition to enhancing turbulent mixing, as observed on day 65 (Fig. 3.4). This non-tidal inflow of surface saltier water may also contribute to a stronger vertical mixing by decreasing stratification and potentially driving convective mixing although not seen in the density data set with discrete surface and bottom measurements only. Offshore winds were identified as a possible factor to contribute to the onset of gravitational circulation by advecting less dense surface water seaward over denser water below, and tending to enhance stratification and inhibit mixing.

Wind may move water windward, altering the sub-tidal sea surface level and setting up a surface slope. Relatively constant wind towards the head of the estuary can generate a surface slope by moving water landward as

$$\frac{\partial \eta}{\partial y} = \frac{\tau_W}{\rho g h} \tag{3.4}$$

which formulates the maximum wind contribution (Wong and Garvine, 1984). A non-tidal barotropic gradient can be established and can ultimately affect the mean circulation. Once the wind either stops or changes direction, the surface slope relaxes and can potentially generate a pulse of mean circulation. Data from day 443 (Fig. 3.16) showed an increase of 0.4 m on the sea level due to landward strong winds although surface slope was null. By applying equation 3.4 to the $\tau_W = 0.5\ \mathrm{N\,m^{-2}}$ observed at Southampton Water on day 443, the maximum wind contribution to the sea level rise is 0.05 m. This simple calculation indicates that local wind stress can not explain alone the observed sea level rise. From these results the effects of the wind on the adjacent coastal region is probably more effective in pumping water into the estuary than the local wind setup mechanism.

Effects of the wind-driven fluctuations of the sea level on the gravitational circulation are comparable to results of three-dimensional model experiments in the inner Juan de Fuca Strait, where the intensification of seaward winds during a period of low tidal-induced mixing was related to an increasing in the strength of the gravitational circulation (Masson and Cummins, 2000). Seaward wind on the Strait of Georgia, separated from Juan de Fuca Strait by a series of narrow channels, leads to a water level rise at its end, forcing the surface water toward the channelled passages. On neap tides, i.e. low tidal mixing, a gravity current develops with higher seaward surface velocities and lower surface salinity. However, if the wind event occurs at the higher mixing spring tide instead, no formation of gravitational circulation was noticed.

Besides the fetch-limited generation of turbulent mixing, this section showed that additional effects of the wind on the gravitational circulation moving the surface water leeward can be summarised as: (1) a positive one, with the wind direction favouring a surface flow down the estuary, as observed on day 443 and by Masson and Cummins (2000); (2) it can have little or no effect, when steady transversal winds do not alter

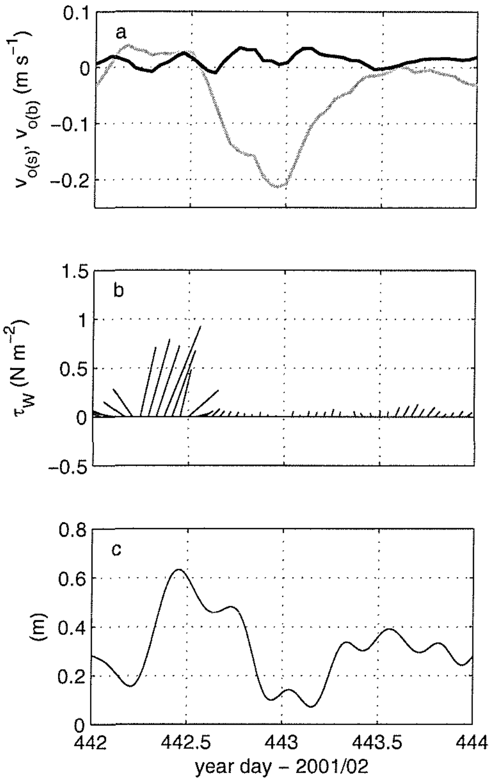

Figure 3.16: **Mean flow driven by relaxation of wind-induced surface set up on day 443, with (a) hourly tidally-averaged velocity at surface ($v_{o(s)}$ - gray line) and bottom ($v_{o(b)}$ - black line); (b) hourly directional wind stress τ_W; and (c) 6-h filtered surface level at the head of the estuary (Dockhead), relative to the mean sea level. Positive values of velocity in (a) indicate flow into the estuary. Wind stress in (b) points the direction to with north at the top of the figure.**

significantly the bi-directional flow (day 358); and (3) it can have an opposite effect when wind from the mouth of the estuary can transport saltier water into the estuary and alter mean circulation and vertical stability.

Effects of the variation of the atmospheric pressure on the gravitational circulation

Changes in the atmospheric pressure may cause a rise or fall of the sea surface and bring water into or out of the estuary as a consequence. This sub-tidal variation of the height of the water may set a barotropic pressure gradient and affect the mean circulation. Effects of the variation of the atmospheric pressure on the mean circulation were possibly observed during a weak event of gravitational circulation during the spring deployment (Fig. 3.17).

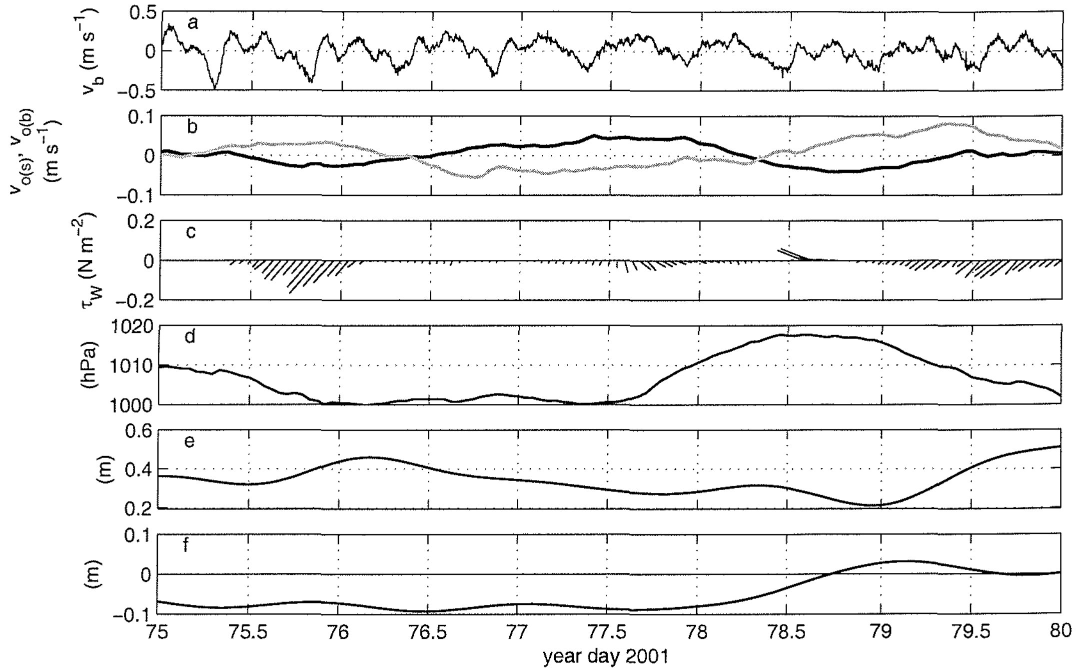

Figure 3.17: **Effects of changes of the atmospheric pressure on the gravitational circulation on day 78, with (a) near bed velocity v_b; (b) hourly tidally-averaged velocity at surface ($v_{o(s)}$ - gray line) and bottom ($v_{o(b)}$ - black line); (c) hourly directional wind stress τ_W; (d) atmospheric pressure at sea level; (e) 24-h filtered sea surface height above datum at Dockhead tidal gauge; and (f) 24-h filtered head-to mouth surface height difference. Positive values of velocity in (a) and (b) indicate into the estuary. Wind stress in (c) points the direction to with north at the top of the figure. Positive sea surface slope in (f) indicates higher water level at the head of the estuary.**

The semi-diurnal maximum bed velocity $v_{b(Emax)}$ decreased approaching the neap tide on day 76.5 (Fig. 3.17a), allowing the development of a weak bi-directional flow (Fig. 3.17b) when wind stress was very weak, with $\tau_W < 0.1$ N m^{-2} for the next three days (Fig. 3.17c). After day 77.5 atmospheric pressure increased from 1000 to 1017 hPa in less than 24 hours (Fig. 3.17d). As result of this rise of atmospheric pressure the sub-tidal sea surface level decreased 0.1 metre to be 0.2 metre above datum (Fig. 3.17e). The sub-tidal surface slope also changed from 0.09 metre higher at the mouth on day 77.9 to 0.04 metre higher at the head of the estuary on day 79.1 (Fig. 3.17f). These changes in both the sea surface height and the surface slope in the estuary were associated with the variation of the atmospheric pressure. The sub-tidal barotropic flow, possibly induced by these changes of the atmospheric pressure, might have caused the cessation of the bi-directional mean flow consistent with the gravitational circulation observed on day 78. A simple comparison between the forces induced by the longitudinal density gradient and the slope variation can be done by applying the right hand side of the equation 1.1 to Southampton Water. Taking a mean depth of 15 m and a estuary length of 10 km, the force driven by a change of 0.01 m of the surface slope corresponds to two-thirds of the force driven by a longitudinal density gradient of 1×10^{-4} $\mathrm{kg\,m^{-4}}$.

3.3.3 Intra- and inter-annual variability

The longitudinal density gradient is obviously a necessary requirement to initiate and sustain gravitational circulation. During the period of low freshwater input in August/September 2001 (second deployment) the most probable cause for the non-observation of clear episodes of gravitational circulation was the lower longitudinal density gradient. The low river discharge may have limited the density gradient near the mouth of the rivers and confined the location of gravitational circulation to a restricted area in the upper estuary. The higher values of salinity measured at surface in the mooring site (days 260 to 267) are consistent with the lower freshwater input into the estuary (Fig. 3.18).

The value of bed velocity which is critical to stall the gravitational flow (see Fig. 3.11) may change according to the strength of the longitudinal density gradient, mainly controlled by the freshwater input. The link between extended periods of low tidal mixing and the occurrence of gravitational circulation, observed on the spring-neap modulation described above, suggests that a lower horizontal density gradient would require the tidal currents to be weaker in order to allow an acceleration of the gravitational flow. The implication is that the horizontal density gradient during the summer deploy-

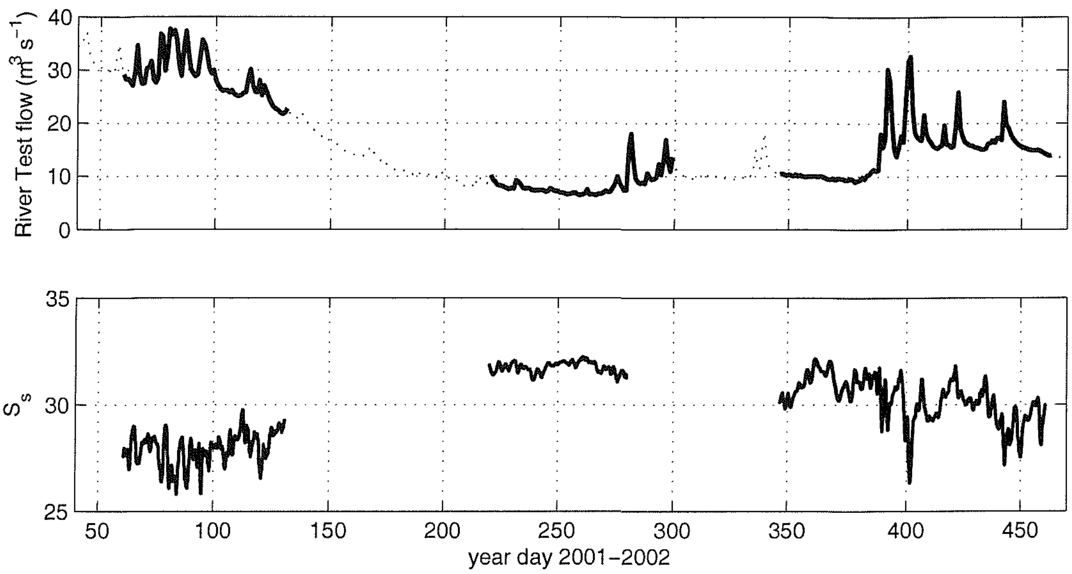

Figure 3.18: **Time series of (a) the River Test discharge, as shown in the Fig. 2.10; and (b) the 25-h running window average of the surface salinity S_s at the mooring site. Year day starts counting on 1 Jan 2001.**

ment dropped below some critical level such that the tidal currents were always supplying enough mixing to prevent enhanced gravitational circulation. It seems that Southampton Water is on the borderline between being able to have times of enhanced gravitational flow (higher freshwater input) and not being able to (lower freshwater input).

During periods of low river discharge, the stratification induced by the gravitational circulation would have been restricted to a region much closer to the freshwater source permitting a stronger vertical mixing along the estuary due to less buoyancy stability. A possible migration of the region of the estuary which can be potentially affected by the stronger episodes of gravitational circulation can be suggested. This region would be confined more at the vicinities of the freshwater source during the dry season, propagating seawards as river flow increases.

Inter-annual variability of rainfall can be a function of long-period meteorological signals, such as the North Atlantic Oscillation and the El Niño Southern Oscillation. Considering the observed influence of river discharge on the exchange flow via gravitational circulation, these meteorological signals can lead to an inter-annual modulation of the gravitational circulation. Wetter or drier climate following global climate changes could also increase or reduce the water exchange and modify the ecosystem. Potential decadal variability should be taken into account by environmental decision makers when discussing future policies for estuarine areas.

Chapter 4

Semi-diurnal modulation

In this chapter the short-term fluctuations of the gravitational circulation are analysed in the context of the variability in tidal and wind mixing. The aim is to assess the timescales of turbulent mixing reduction that lead to a detectable increase in the gravitational circulation and identify which physical processes may be involved.

The section below describes the specific methods used in the analyses of the short-term fluctuations of the non-tidal velocity, including a brief introduction to the wavelet transform. The following sections show the results obtained by these analyses, focusing firstly on the fluctuations of the non-tidal velocities in individual tidal cycles. Afterwards the short-term fluctuations are shown in combination with the spring-neap modulation of the gravitational circulation detailed in the previous chapter.

4.1 Methods

The specific methods used to analyse the fluctuations of the gravitational circulation on hourly time scales are described in this section. The procedure for obtaining the non-tidal velocity during the different semi-diurnal tidal stages is explained. This non-tidal velocity is broke in five different semidiurnal tidal stages.

4.1.1 Non-tidal velocity at different tidal stages

Time series of the non-tidal velocity were obtained by subtracting the predicted or reconstructed periodic tidal signal from the original data set. By applying the least square fitting harmonic analysis (equation 3.1) to the three ADCP deployments the non-tidal current, v_A, can be calculated as

$$v_A = v_o + v_R \qquad [\mathrm{m\,s^{-1}}] \tag{4.1}$$

where v_o is the tidally averaged velocity and v_R is the residual velocity, interpreted as the residual signal in the tidal analysis. The residual component of the time series velocity is normally calculated by the difference between the ADCP data, v, and the harmonic analysis results. Then v_R can be expressed by rearranging equation 3.1 as

$$v_R = v - \left[v_o + \sum_{i=1,N} A_i \cos(\omega_i\ t + \phi_i) \right] \qquad [\mathrm{m\,s^{-1}}] \tag{4.2}$$

for N harmonic constituents. The non-tidal velocity v_A can then be written as

$$v_A = v - \sum_{i=1,N} A_i \cos(\omega_i\ t + \phi_i) \qquad [\mathrm{m\,s^{-1}}] \tag{4.3}$$

The analyses was applied in a moving 25 hour window of data continuously for tidal constituents of periodicity of, or shorter than, the semi-diurnal cycle (i.e. M_2, M_4, M_6, M_8, M_{10}, M_{12} and M_{14}) as described in section 2.2.1. The surface time series were measured at 0.75 m below the surface and the bottom at 1.5 m above the bottom. The standard deviations of the non-tidal velocity, v_A, were lower than 0.004 $\mathrm{m^2\ s^{-2}}$ for the bottom and less than 0.007 $\mathrm{m^2\ s^{-2}}$ for the surface during the three deployments (Table 4.1).

Time-series of the surface, $v_{A(s)}$, and bottom, $v_{A(b)}$, non-tidal velocities were broken into sections following the times of distinct semi-diurnal tidal stages. The semi-diurnal tidal cycle was divided in five stages according to main characteristics of the tide in Southampton Water: ebb tide (E), first flood tide (F1), young flood stand (YFS), second flood tide (F2) and double high water (DHW). To delimit these tidal stages the time of maximum ebb velocity within a cycle was used as a reference time and the limits of the five different stages were fixed following the duration of each stage related to this maximum ebb current point (Fig. 4.1). The limits of the tidal stages were determined by selecting data from the depth-averaged ADCP velocity time series for the five tidal stages, calculating the standard deviation for each stage and finding the combination of lower standard deviations. This method was applied on each deployment data set. Surface and bottom non-tidal currents were then averaged within the limits of each stage, resulting in a time series of mean non-tidal current for each one of the five stages.

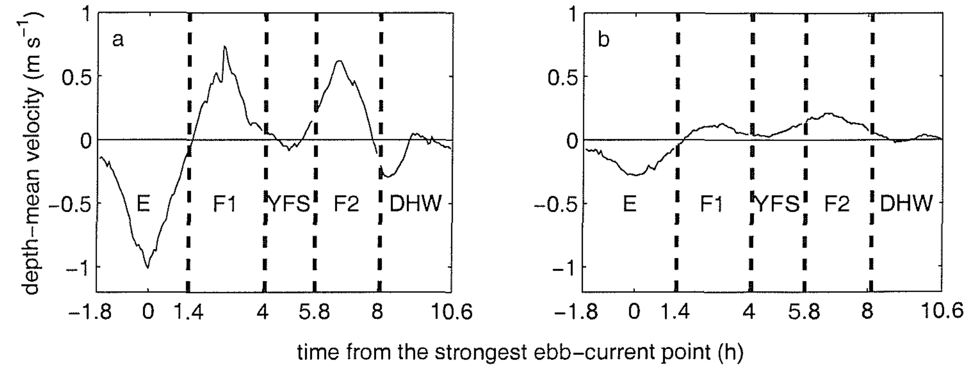

Figure 4.1: **Depth-mean velocity at a typical spring (a) and neap (b) tide showing the division of the semi-diurnal tidal stages. The vertical dashed lines indicate the limit between the different stages referred to the time of the peak of the ebb current (t = 0). The five characteristic tidal stages in Southampton Water are ebb tide (E), first flood (F1), young flood stand (YFS), second flood (F2) and double high water (DHW).**

Table 4.1: **Mean square error of the surface and bottom non-tidal velocities, v_A, for each of the three mooring deployments.**

deployment (duration)	*surface (m^2 s^{-2})*	*bottom (m^2 s^{-2})*
spring (71 days)	0.006	0.003
summer (80 days)	0.006	0.002
winter (117 days)	0.006	0.004

4.2 Results

This section describes the results of the analysis of the non-tidal velocity fluctuations on semi-diurnal, tidal cycle, time scales with the spectra limited to variabilities of periods shorter than 24 hours. The analysis was extended to the three deployments carried out.

Observations of the net circulation after the onset of the gravitational circulation (spring-to-neap transition on day 104 - Fig. 4.2a) showed a surface outflow and a bottom inflow of both the 25-h running window mean velocity (Fig. 4.2b) and the tidally averaged velocity, calculated by equation 3.1 (Fig. 4.2c). These observations motivated an investigation of the short term fluctuations of the non-tidal velocity. Data was analysed using a range of methods of different complexities, from a simple direct assessment of the residual current through to the wavelet analysis described earlier. The reasoning behind this was to describe the fluctuations according to the degree of complexity of the method, from the less to the more complex. First, some of the semi-diurnal tidal cycles, chosen specifically because of the low wind stress at the time, were examined. By assuming no wind effects these low wind tidal cycles permit a simple investigation of the tidal mixing mechanism acting on the modulation of the bi-directional flow in semi-diurnal time scales.

Following this most simple analysis, the non-tidal currents from all observed tidal cycles are analysed in terms of the behaviour during the five tidal stages. The spring-neap analysis of Chapter 3 provides a context for this method, to assess whether or not the longer-term behaviour of the gravitational circulation is made up of short-term intra-tidal events.

4.2.1 Behaviour of gravitational circulation over individual tidal cycles

To investigate the short term fluctuations of the gravitational flow, time series of the surface and bottom non-tidal velocities were analysed over individual periods of 25

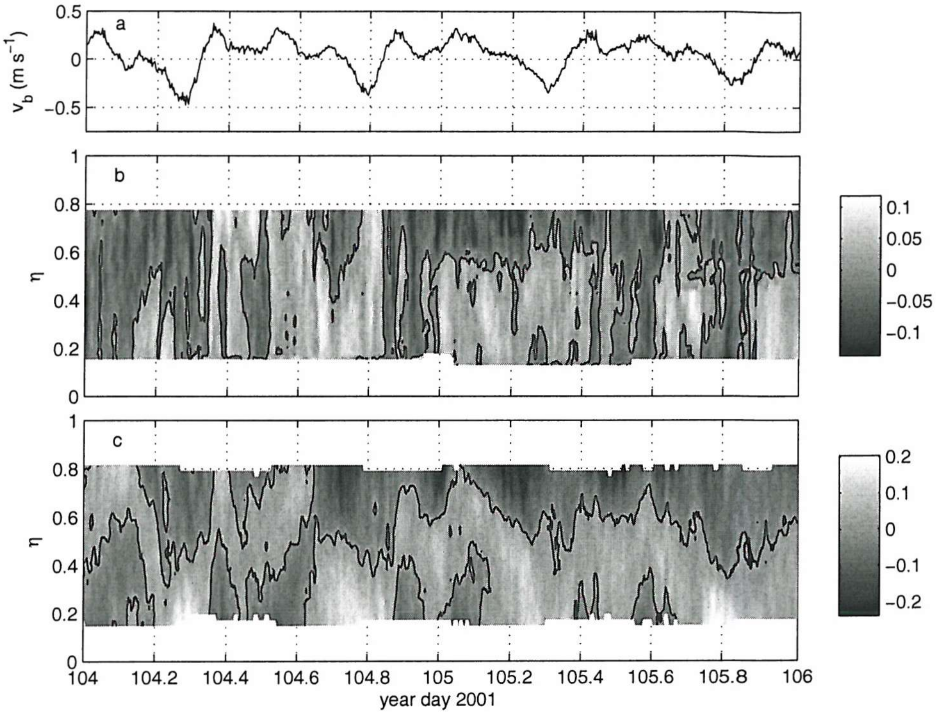

Figure 4.2: **Time series of the bottom velocity (a), the depth-normalised 25-h running window mean velocity (b), and the depth-normalised tidally averaged velocity (c), for the period of gravitational flow between days 104 and 106. Positive velocities are into the estuary. Units in the contour plots are in m s^{-1}, with black lines showing the zero velocity.**

hours. To minimise the interference of measured physical mechanisms other than tide in the behaviour of the non-tidal currents, the criteria for the choice of the tidal cycles to be analysed here were: (1) wind speed lower than 4 m s^{-1} (τ_W < 0.04 N m^{-2}) and with a preferable direction perpendicular to the estuary; (2) constant sub-tidal surface sea level in the estuary; and (3) mouth-to-head sub-tidal surface slope lower than 0.04 m (see section 2.1.2). The reason for taking this approach was to attempt to visualise any basic link between tidal mixing and non-tidal flows during a tidal cycle, as the simplest expression of the main topic of this thesis. Ten 25 hour periods were found from the three deployments, following the criteria above (Table 4.2). Four of those ten periods were chosen based on the strength of the tidal mixing to show the effects of different current fluctuation on the semi-diurnal cycle.

Two 25 hour periods were selected from the first deployment to investigate the fluctuation of the non-tidal currents. These periods began on day 60.8 (Fig. 4.3a to e) and on day 63.4 (Fig. 4.3f to j). The first selected 25 hour period from the spring deployment was during the spring-neap transition at the beginning of the first deployment (day 61) with wind stress lower than 0.025 N m^{-2} (Fig. 4.3a,b). Bottom tidal velocities reached 0.45 m s^{-1} on the flood and -0.5 m s^{-1} on the ebb tides, and the slack water periods extended for two hours during the YFS and three hours at the DHW stages. Surface and bottom non-tidal currents varied around zero with a few peaks for both direction (i.e. into and out of the estuary) particularly in the surface. No obivious bi-directional flow was observed during this period. The mean flow over the period was very weak, with surface and bottom mean currents lower than $|0.01|$ m s^{-1}. Bottom-surface density difference varied between 3 and 4 kg m^{-3} during most of this period (Fig. 4.3e), increasing only at the ebb tides to be higher than 5 kg m^{-3}.

The second low wind period occurred during the neap tide on day 63, with bottom currents being lower than 0.25 m s^{-1} during the floods and reaching -0.3 m s^{-1} during the ebbs (Fig. 4.3f,g). The small difference found in the bottom currents between F1 and YFS during the second tidal cycle on day 64 ($v_b \approx 0.1$ m s^{-1}) shows that the separation of the tidal stages at the neap tides can be occasionally very subtle or even indistinguishable. A weak pulse of flow consistent with gravitational circulation appeared to be after the

Table 4.2: **Maximum bed velocity and wind stress and mean surface slope for the ten 25-h period of low wind found in the time series, following the criteria in the text. Positive surface slope means a higher level at the mouth of the estuary. Days marked with ⋆ were selected for detailed analysis.**

year day	*max v_b (m s^{-1})*	*max τ_W (N m^{-2})*	*surface slope (m)*
61⋆	-0.5	0.025	0.03
64⋆	-0.3	0.005	-0.01
74	-0.55	0.055	0.02
105	-0.36	0.086	-0.03
264	-0.73	0.007	0.01
293	-0.6	0.036	-0.03
351⋆	-0.72	0.03	0.01
356⋆	-0.4	0.035	-0.01
368	-0.68	0.009	0.02
412	-0.75	0.045	0.0

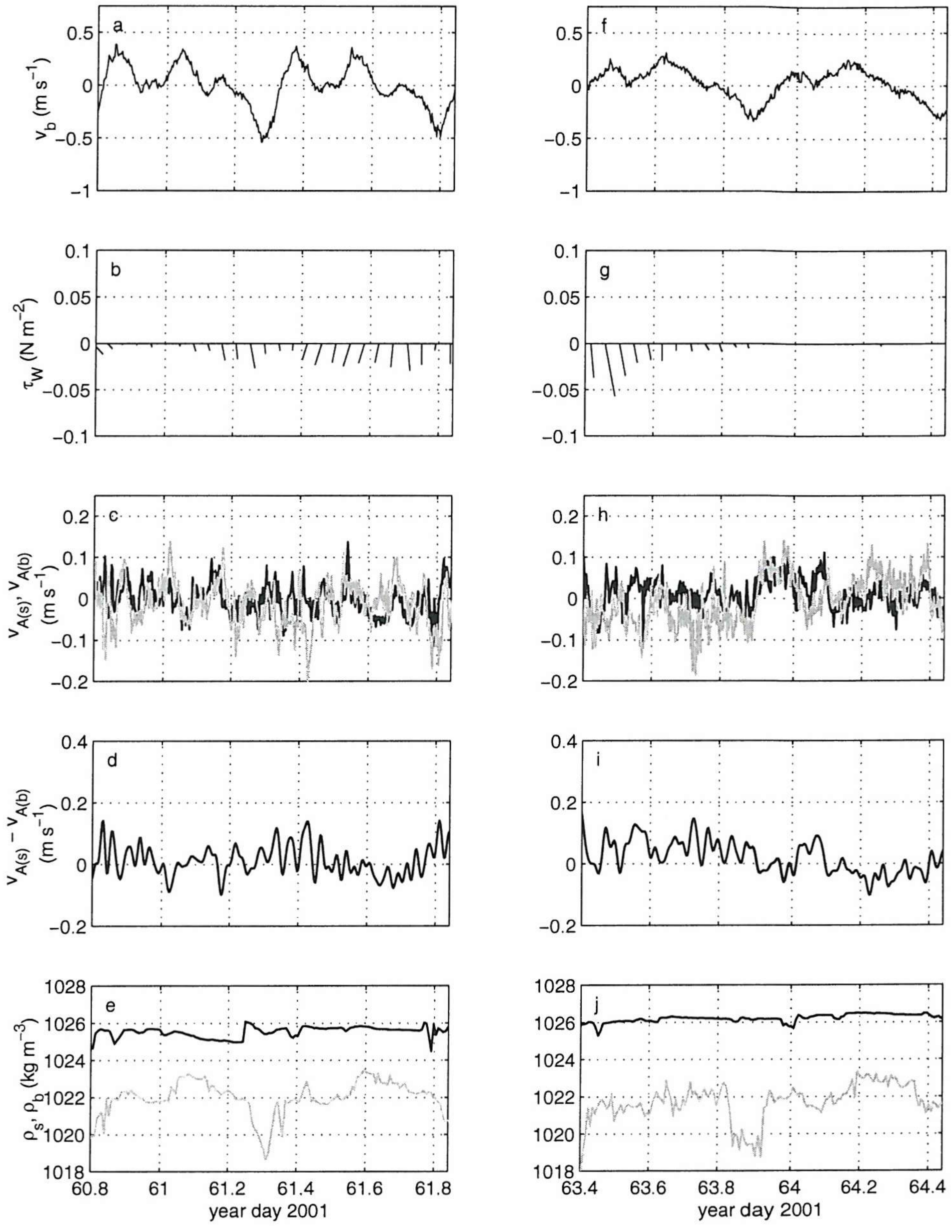

Figure 4.3: **Data from two 25 hour periods of calm weather conditions on days 61 (a to e) and 63 (f to j), showing time series of (a and f) bottom velocity v_b; (b and g) hourly wind stress τ_W; (c and h) surface $v_{A(s)}$ (gray line) and bottom $v_{A(b)}$ (black line) non-tidal velocities; (d and i) 32-minute filtered non-tidal velocity shear $v_{A(b)} - v_{A(s)}$; and (e and j) surface ρ_s (gray line) and bottom ρ_b (black line) density. Positive velocities are into the estuary. Wind stress in (b and g) indicates direction to with the north on the top of the figure.**

YFS stage on day 63.5, with the non-tidal shear being higher than 0.1 m s^{-1} for 2 hours (Fig. 4.3h,i). A fast but strong pulse of seaward non-tidal current in the surface ($v_{A(s)} >$ 0.1 m s^{-1}) occurred on day 63.7 for less than one hour at the DHW, although the bottom non-tidal current remained around zero. After the following ebb both surface and bottom non-tidal currents were around 0.05 m s^{-1} directed into the estuary. The mean surface and bottom tidal currents over the 25 hour period were 0 and 0.03 m s^{-1}, respectively. Bottom density was around 1026 kg m^{-3} during the whole 25 hour period while surface density decreased from 1022 to less than 1020 kg m^{-3} at the ebb tide to return to 1022 kg m^{-3} at the flood (Fig. 4.3j).

The two selected tidal cycles from the third deployment began on days 351 and 356.3. Wind stress at these tidal cycles was lower than 0.035 N m^{-2} and no significant changes of the non-tidal sea surface level and sea surface slope in the estuary were present. The second tidal cycle (day 356.3) is included in one of the neap tide gravitational circulation events observed during the winter deployment and is described in section 3.2.3. Time series of bottom density is not available for this deployment due to poor quality of the data (see section 2.1.1).

On day 351 the maximum bed current v_b was higher than 0.7 m s^{-1} at the ebb tides (Fig. 4.4a). Surface and bottom non-tidal velocities had similar behaviour with no bi-directional flow (Fig. 4.4c). The 25-h mean tidal current was zero at the bottom and -0.02 m s^{-1} at the surface and the non-tidal shear varied mostly between ± 0.1 m s^{-1} (Fig. 4.4d). Surface density was above 1025 kg m^{-3} during most of the tidal cycle, decreasing to 1022 kg m^{-3} at the ebb tides (Fig. 4.4e).

The second tidal cycle in the winter deployment began on day 356.3 during neap tide, with the bottom tidal current weaker than $|0.4|$ m s^{-1} (Fig. 4.4f). Non-tidal velocity showed two short events of bi-directional flow consistent with gravitational circulation: on day 356.5-356.6, during the YFS and the 2F; and on day 357-357.1, at the YFS. During these events the non-tidal velocity ranged between 0 and 0.1 m s^{-1} at the bottom and between -0.1 and -0.15 m s^{-1} at the surface (Fig. 4.4h). Non-tidal shear $v_{A(b)} - v_{A(s)}$ was mostly positive during this tidal cycle, with the mean non-tidal current over the 25-h period of -0.10 m s^{-1} at the surface and 0.03 m s^{-1} at the bottom. This bi-

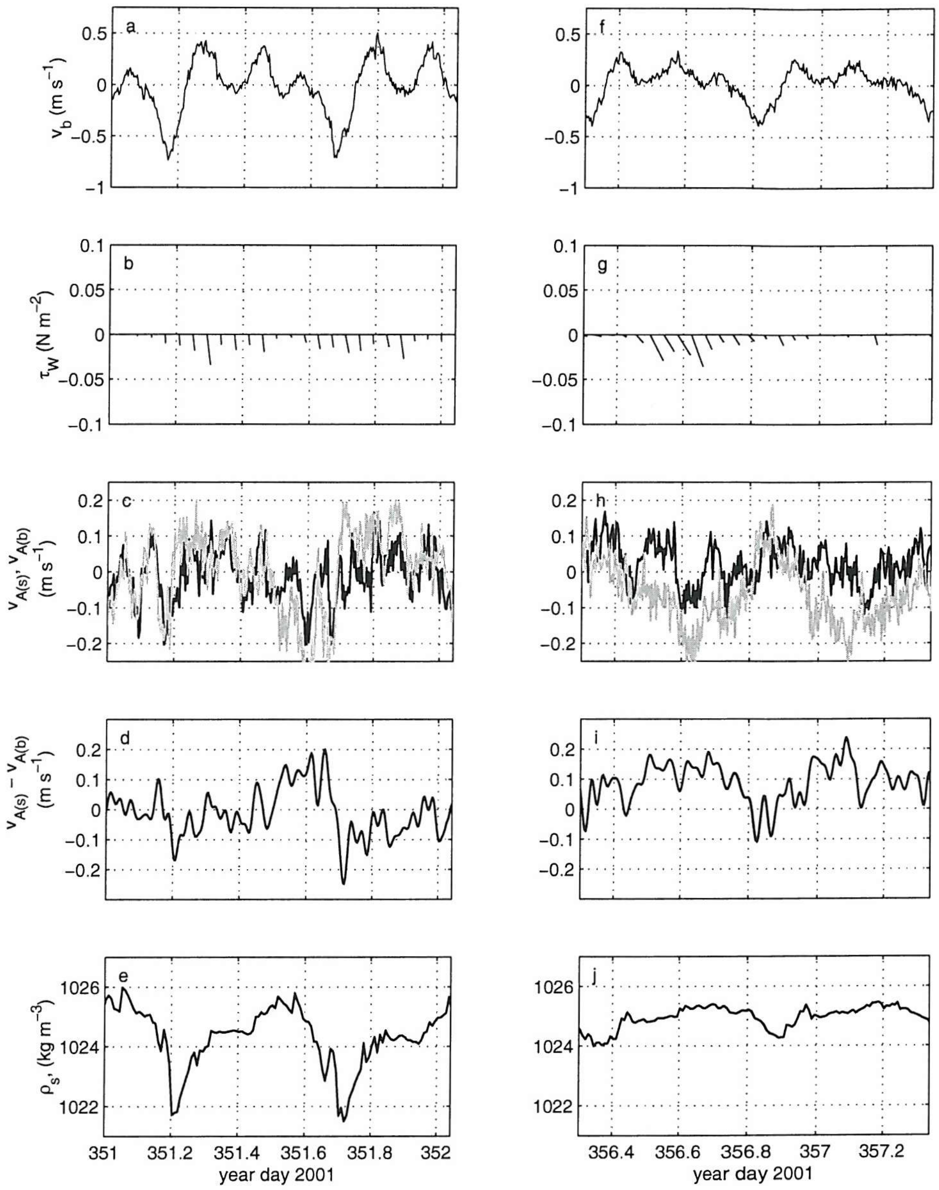

Figure 4.4: **Same as Fig. 4.3 for days 351 and 356, except for e and j where only surface density ρ_s is showed.**

directional mean flow suggests a non-tidal circulation consistent with the gravitational circulation over the 25-hour block (Fig. 4.4i). However no apparent relation could be found between the highly variable short term signal of the non-tidal current and the semi-diurnal modulation of the tidal currents.

In addition to those four 25-h periods of low wind the short-term fluctuations of the mean flow can also be investigated by focusing on the changes of the non-tidal current during the evolution of the events of the gravitational circulation identified in chapter 3. In order to follow the changes of the vertical structure of density, only events from the first deployment have been chosen. This deployment allows the observation of three different mechanisms acting in the control of the gravitational circulation. The first mechanism is the increase of the vertical mixing driven by the tides at the end of a low wind neap tide, which may suppress the bi-directional flow (days 107-110). Another process is the influence of the wind-induced mixing on the formation and collapse of the circulation during the short period of weaker wind within a strong wind period (day 94). The third mechanism is the fluctuation of the non-tidal sea surface level driven by wind setup altering the resultant non-tidal flow on day 94.

Tidal effects

The weak wind conditions observed during the neap tide on the day 107 (Fig. 4.5a) provided a good opportunity to investigate the effects of the tidal mixing on the fluctuations of the gravitational circulation in time scales of hours. The bi-directional flow was completely re-established in less than six hours after the temporary discontinuance on day 106.

The non-tidal velocities increased from near zero on day 107.6 to higher than 0.1 $\mathrm{m\,s^{-1}}$ on day 107.8 (Fig. 4.5b) being out of the estuary at the surface (negative velocity) and into the estuary at the bottom (positive velocity). The bi-directional flow persisted for 16 hours with the surface outflow occupying the top 40% of the water column. No clear fluctuation of the mean flow could be observed although semi-diurnal fluctuations of the bottom-surface density difference showed an increase of approximately 2 $\mathrm{kg\,m^{-3}}$ associated to the ebb tides (Fig. 4.5c). Decrease of bottom density was shifted by one hour comparing to the surface density leading to a stronger stratification during a short period. Stratification followed the onset of the gravitational circulation although no increase of stratification was observed prior to the event. Bi-directional flow became progressively weaker during the next tidal cycles, with the peak bottom currents around 0.4-0.5 $\mathrm{m\,s^{-1}}$ at the ebb tides. During the short period of these stronger ebbs the non-tidal

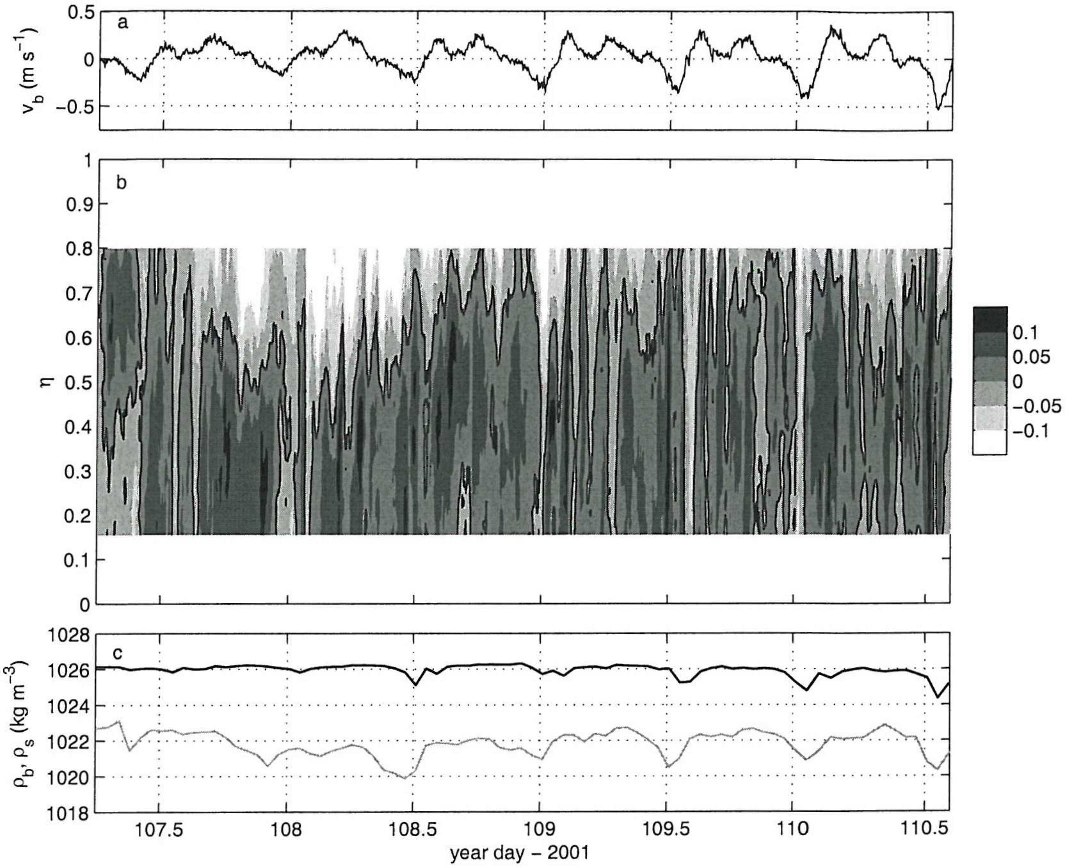

Figure 4.5: **Behaviour of the non-tidal velocity on the onset, duration and cessation of the gravitational circulation between days 107 and 110 showing (a) the bottom velocity, v_b, time series; (b) time series of the depth-normalised non-tidal velocity, $v_{A(\eta)}$, in m s^{-1}; and (c) bottom (ρ_b - black line) and surface (ρ_s - gray line) density time series. The black contour in (b) represents the zero velocity line.**

current was dominantly out of the estuary and consequently both surface and bottom density were reduced. The vertical density structure responded to the decrease of the gravitational circulation by an increasing of the surface density of about 1 kg m^{-3} and a decrease of 0.5 kg m^{-3} at the bottom. This reduction of stratification can reflect an increase of the tidal mixing caused by the stronger bottom currents towards the spring tide, which is also related to the weakening of the bi-directional flow.

Non-tidal effects

Short-term changes of the gravitational circulation due to the action of the wind were observed on day 94 (Fig. 4.6). The vertical structure of the non-tidal velocity changed from a weak bi-directional circulation on day 92-93 to a strong surface flow into the estuary after day 93.5 ($v_{A(s)} \approx 0.1$ m s^{-1}). This change to a landward non-tidal flow was caused by the strong wind ($\tau_W > 0.3$ N m^{-2}) from the mouth of the estuary. The effects of this wind were noticed in rise of the sub-tidal sea level in the estuary caused by the water movement into the confined estuary. The fast reduction of the stratification, with the bottom-surface density difference decreasing from 5 to 2.5 kg m^{-3} during the 12 hours of wind, indicated a vertical mixing which was probably induced by wind stress. Wind then changed after day 94 to become weaker and transversal to the estuary. The sub-tidal sea level immediately responded to this change on the wind by falling in a rate of 0.05 m per hour. The relaxation of the wind setup released the less dense water which was confined at the head of the estuary and a gravitational circulation was established in about 6 hours, with surface and bottom non-tidal velocities reaching 0.2 m s^{-1} out of and into the estuary, respectively. This circulation persisted for 18 hours and its suppression was possibly caused by the increase of the tidal-induced mixing from the ebb tide on day 95 onwards, with a reduction of the stratification. Strong wind from the mouth of the estuary resumed on day 95.5. This northward wind caused another rise in the sub-tidal sea level but apparently the vertical mixing was high enough to avoid the formation of another pulse of gravitational circulation.

4.2.2 Tidal stage analysis over spring-neap cycles

For a more general analysis of the semi-diurnal variability of the bi-directional flow over the 268 days of ADCP measurements, the fluctuations of the surface and bottom non-tidal currents, $v_{A(s)}$ and $v_{A(b)}$, were compared separately at the five different tidal stages (ebb, first flood, young flood stand, second flood and double high water). Mean non-tidal currents in both surface and bottom layers were very irregular, although the spring-neap modulation of the bi-directional circulation identified in chapter 3 can be

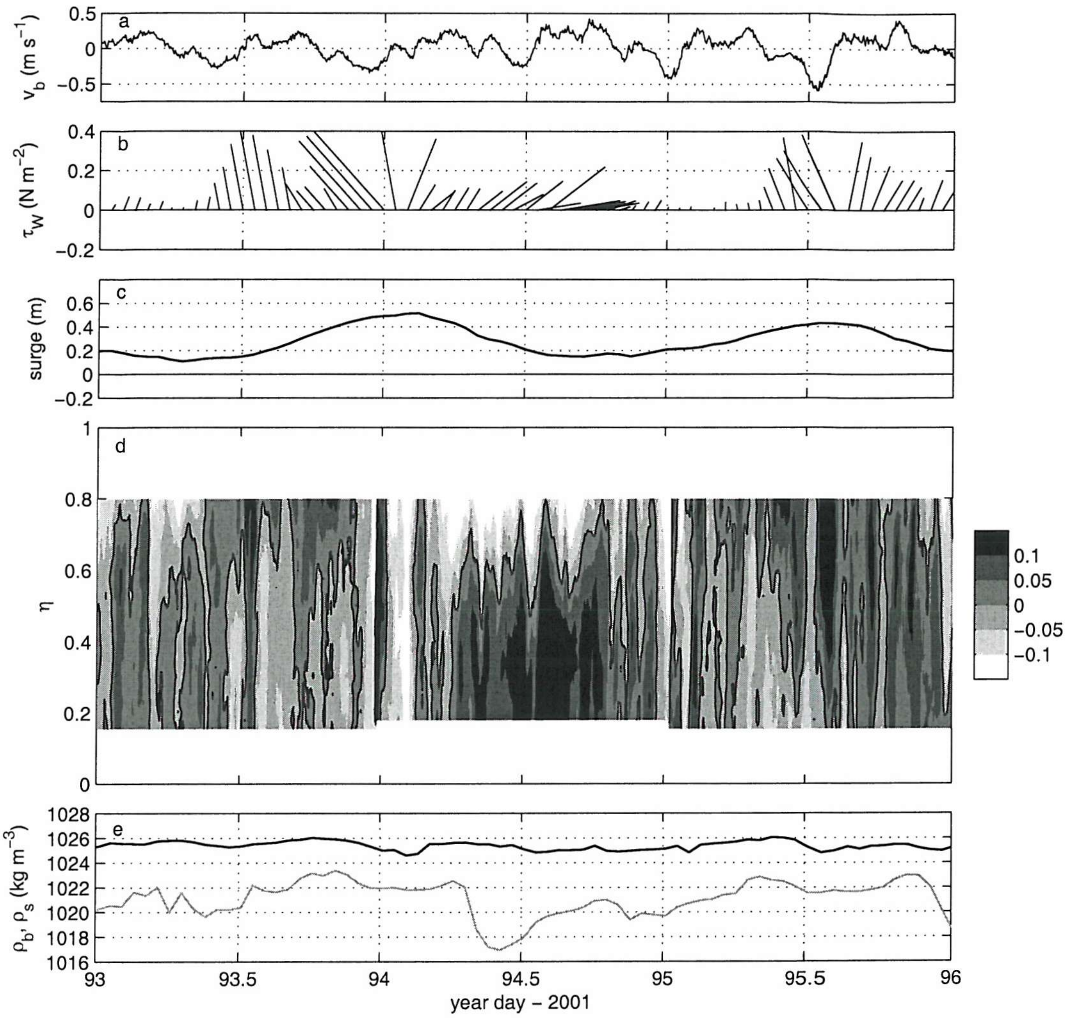

Figure 4.6: **Behaviour of the non-tidal velocity in the establishment, duration and cessation of the gravitational circulation on day 94 showing (a) the bottom velocity, v_b, time series; (b) wind stress τ_W; (c) sub-tidal sea level at Dockhead; (d) depth-normalised non-tidal velocity time series, $v_{A(\eta)}$, in m s^{-1}; and (e) bottom (ρ_b - black line) and surface (ρ_s - gray line) density time series. Wind stress in (b) is aligned relative to north in the positive y-axis direction. The zero sea level in (c) represents the chart datum.**

noticed in the time series.

Analyses of variance (ANOVA) test was applied in order to compare the non-tidal current between the five different stages of the tidal cycle. By taking the time series of the non-tidal velocity from each different tidal stages as a group, the ANOVA indicates if the variance between the groups is significantly different from the variance within the groups (Emery and Thomson, 1997). The results showed there is no significant difference between the five tidal stages of the surface and bottom non-tidal velocities in all of the three deployments for 95 % of confidence level.

The following sections show the results of the comparison of the non-tidal current for each one of those five tidal stages during the spring (Fig. 4.7), the summer (Fig. 4.8) and the winter deployment (Fig. 4.9).

Spring mooring observations

The three events of gravitational circulation during the spring deployment (days 60-131) described in the previous chapter are present in the time series of the surface and bottom non-tidal velocities (Fig. 4.7). The first event on days 76 and 77, the weakest one, showed a persistent non-tidal bi-directional current at F1, F2 and DHW with $v_{A(b)} - v_{A(s)} > 0.1$ m s^{-1} during four consecutive tidal cycles. Weak seaward surface currents can be noticed at YFS without a landward bottom flow though. This event finished with a fast rise of the sub-tidal sea surface level caused by the decrease of the atmospheric pressure (section 3.3.2).

The second event of gravitational circulation in this deployment is the short pulse of bi-direction flow observed around day 95 (Fig. 4.7), with the averaged non-tidal currents reaching values around 0.1 m s^{-1} in the bottom (positive) and the surface (negative) in all the five tidal stages. The non-tidal bi-directional flow was stronger at the DHW, with the bottom-surface non-tidal shear being higher than 0.15 m s^{-1}. The highly variable non-tidal velocities before and after day 95 were associated with the presence of a relatively strong wind, which may have contributed to the observed variability of this gravitational circulation event.

The last pulse of the spring deployment, during a low wind period, was dominated by the presence of a circulation consistent with the gravitational flow during all stages of the semi-diurnal tidal cycle from day 104 to day 111. The shear flow, $v_{A(b)} - v_{A(s)}$, had slightly lower values at the YFS than at the other tidal stages although the averaged values over the times of the events were very similar (Table 4.3).

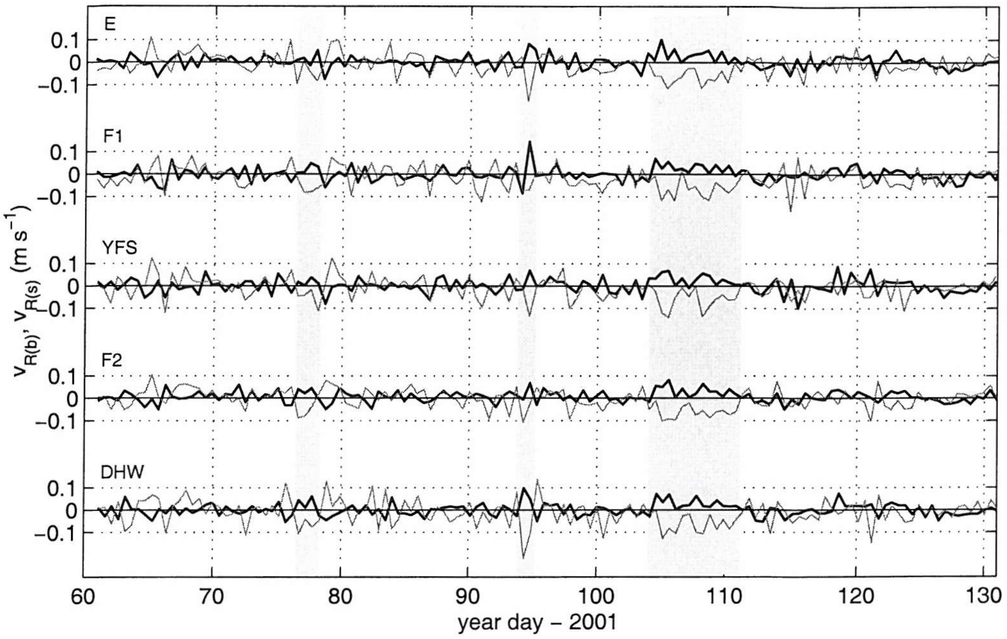

Figure 4.7: **Spring deployment near-surface (gray line) and near-bottom (black line) non-tidal velocities, averaged for each of the following tidal stages: ebb tide (E), first flood (F1), young flood stand (YFS), second flood (F2) and double high water (DHW). Vertical shadows indicate the days of the pulses of gravitational circulation clearly identified in the long term variability analysis.**

Table 4.3: **Mean±standard deviation of the surface ($v_{A(s)}$), bottom ($v_{A(b)}$) and bottom-surface non-tidal shear velocity ($v_{A(b)} - v_{A(s)}$), in m s^{-1}, for the five tidal stages during the gravitational circulation event on days 104-111.**

	EBB	**F1**	**YFS**	**F2**	**DHW**
$v_{A(s)}$	**-0.063±0.044**	**-0.062±0.049**	**-0.059±0.035**	**-0.058±0.042**	**-0.062±0.034**
$v_{A(b)}$	**0.029±0.030**	**0.029±0.022**	**0.028±0.024**	**0.032±0.025**	**0.029±0.024**
$v_{A(b)} - v_{A(s)}$	**0.091±0.045**	**0.091±0.044**	**0.087±0.067**	**0.090±0.048**	**0.090±0.051**

Summer mooring observations

The main characteristic of the summer deployment (from day 219 to day 299) was the low longitudinal density gradient caused by an extended period of lower river discharge. This weak density gradient is thought to be the most probable reason for the absence of gravitational circulation during summer 2001, as described in chapter 3.

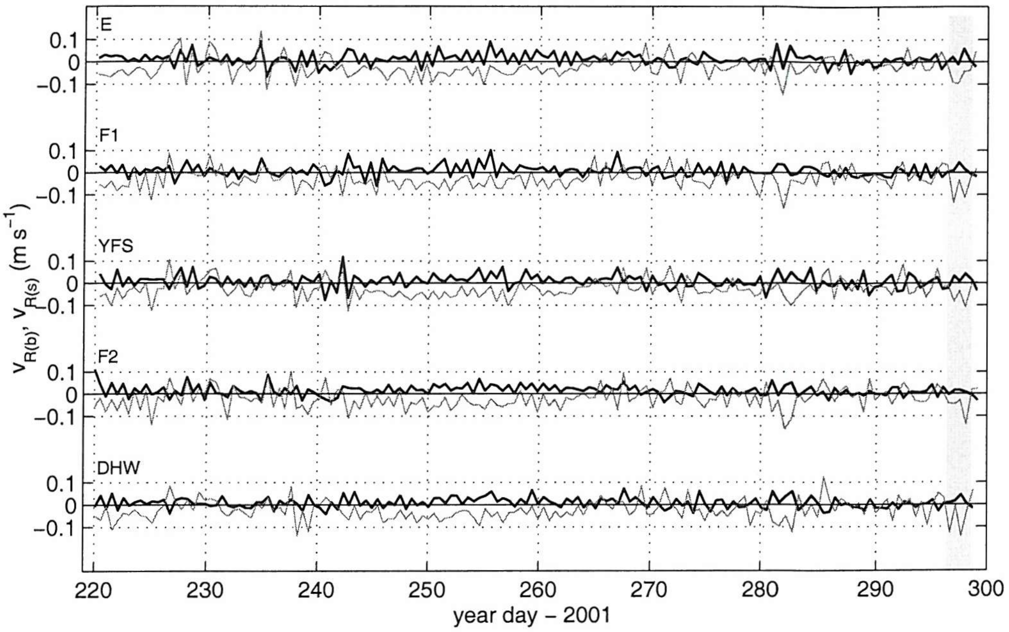

Figure 4.8: **Same as Fig. 4.7 for the summer deployment.**

The variability of non-tidal currents averaged of the five tidal stages suggested that there is a weak mean background flow at all the summer deployment. Small differences can be noticed though. The first third of this time series had a more variable flow in all five tidal stages (Fig. 4.8) although the wind was calm through most of this period. A weak bi-directional residual currents were predominant from day 245 to day 262. The averaged velocities over this period was around -0.04 m s^{-1} in the surface and 0.02 m s^{-1} in the bottom at all stages, when river discharge reached the lowest values.

A short but pronounced peak in the surface mean non-tidal current ($|v_{A(s)}| > 0.1$ m s^{-1}) was observed on day 283 at all five different tidal stages. These out-of-estuary velocities may be related to the relaxation of the barotropic pressure gradient caused by a wind-induced elevation of the sea level (see Fig. 3.6c,d). An increase of the surface non-tidal current was observed on day 297 during all 5 tidal stages. This persistent surface net outflow, with an average of -0.08 m s^{-1}, coincides with the only bi-directional flow identified by the long-term analysis described in Chapter 3 for this deployment. However the bottom non-tidal current did not increase significantly to characterise well a bi-directional flow in any stage of the semi-diurnal tidal cycle, with an average lower than 0.03 $\mathrm{m\,s^{-1}}$ at all five tidal stages.

Winter mooring observations

The time series of the averaged non-tidal current for the 5 different tidal stages in the winter deployment (days 346 to 464) are presented (Fig. 4.9). Two long (days 356-360 and days 416-419) and four short (days 389, 402, 443 and 459) events of gravitational circulation were associated with the low tidal mixing at the neap tides in the analysis of the long term modulation (section 3.2.3).

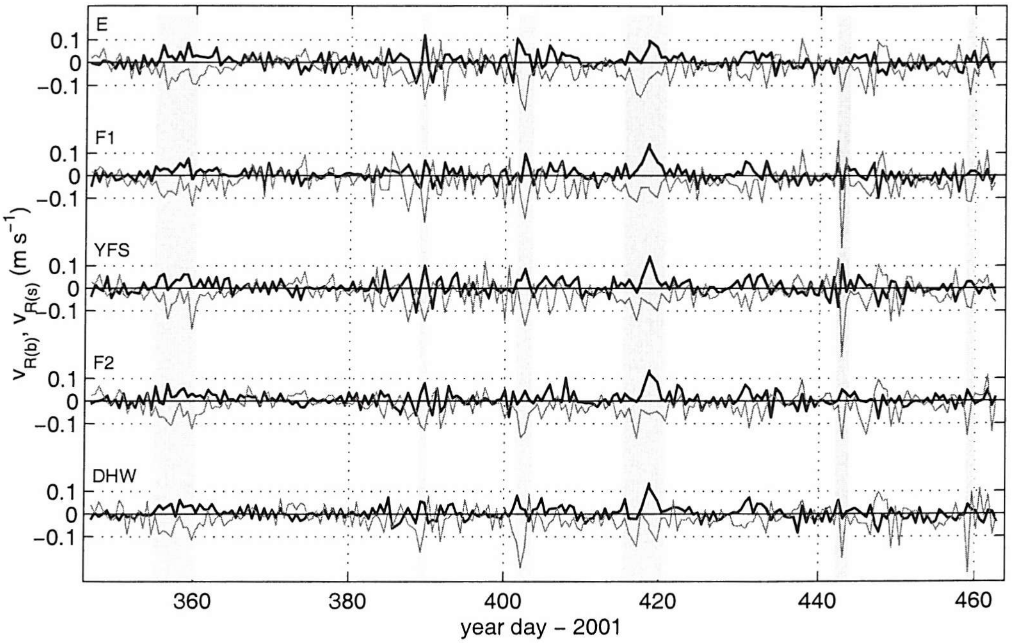

Figure 4.9: **Same as Fig. 4.7 for the winter deployment.**

During the two longer events of gravitational circulation (days 356-360 and 416-420) the averaged surface non-tidal velocities over the days of the events were -0.07 $\mathrm{m\,s^{-1}}$ for days 356-360 and -0.08 $\mathrm{m\,s^{-1}}$ for days 416-419. Averaged bottom non-tidal velocities were respectively 0.03 and 0.06 $\mathrm{m\,s^{-1}}$. Tidal stage mean values of the non-tidal shear velocity, $v_{A(b)} - v_{A(s)}$, were around 0.10 $\mathrm{m\,s^{-1}}$ on the first and 0.12 $\mathrm{m\,s^{-1}}$ on the second event at all stages. Short pulses of bi-directional flow were observed on days 389 and

403 at all five different stages. Strong non-tidal velocities were present particularly on day 403 in the surface ($v_{A(s)} > 0.13$ m s^{-1}) but were weaker and more variable in the bottom, except for both ebb tides with slightly stronger velocities. A pulse of intense outflow of the non-tidal surface velocity was present for one tidal cycle on day 443. This pulse was particularly strong at the F1 and the DHW, when the average over the stage time was above 0.3 m s^{-1}. However a bi-directional flow was observed only at the YFS, with bottom non-tidal velocity of 0.11m s^{-1}. A similar pattern was repeated on day 459 with lower non-tidal velocities in the surface.

4.3 Discussion

Two different methods were applied in the analysis of the semi-diurnal modulation of the non-tidal flow and their results are discussed in this section. The simpler method was the 25-hour analysis block of surface and bottom non-tidal velocities data, selecting tidal cycles of weak wind stress. This is the simplest way to observe the effects of the semi-diurnal variability of the tidal mixing on the non-tidal circulation. In addition to this method the short term fluctuations of the non-tidal velocity during two events of gravitational flow were also analysed. In the second method the non-tidal velocity data set were separated between the five tidal stages. This strategy allows an indication of any sub-tidal variability of the mean flow that might be consistent with gravitational circulation responding to different aspects of the tidal cycle.

By only including periods of low wind, the analysis of the 25-hour blocks of non-tidal velocities offers an opportunity to investigate the role of the short term fluctuation of different strengths of tidal mixing in affecting non-tidal flow. The results did not show any clear tidally-related modulation of the non-tidal velocity. Not even during the gravitational circulation events identified in the chapter 3 on days 94 and 107 could the effects of the semi-diurnal fluctuations of the tidal mixing on the non-tidal circulation be observed. A systematic reason for the non-observation of semi-diurnal modulation of the gravitational circulation may be the harmonic method applied to obtain the non-tidal velocity. Slack water signal may appear to the analysis as part of shallow water tidal constituents and be removed from the non-tidal velocity analysed.

Based on the visual comparison of the non-tidal currents from the different five tidal stages there was no semi-diurnal modulation of the non-tidal flow during the events of gravitational circulation. The results of the ANOVA also showed that there is no significant difference for a confidence level of 95% between the bottom-surface non-tidal shear velocity from the different tidal stages. These results persisted even if only data from the observed long-term event of gravitational circulation on days 104-111 were analysed (section 3.2.1). The lack of significant different between the bottom-surface non-tidal shear velocity from the different tidal stages suggests that the gravitational circulation was indeed confined to the neap tide pulses described in the previous chapter. However, the far more numerous semi-diurnal tidal cycles with no signal of gravitational flow would have made it difficult for the ANOVA be able to identify any of the short-term fluctuations.

Stacey et al. (2001) showed through principal component analysis the modulation of gravitational flow following the semi-diurnal tidal cycle. This modulation was driven by the barotropic ebb-flood fluctuation of the tidal straining mechanism which enhanced stratification during weak ebb tides and inhibited during the flood. The stronger stratification at ebbs reduced the vertical mixing, allowing gravitational flow to develop further. Convective instabilities appeared on the flood tides leading to an increase of the tidal mixing due to unstratified conditions. The stronger mixing at flood refrained the occurrence of gravitational circulation pulses.

Separating the different barotropic and baroclinic mechanisms operating in tidally non-linear system is difficult, and may require a model-based approach (e. g., Burchard and Baumert, 1998). This difficulty is due to the superimposition of these mechanisms on tidal timescales. The horizontal Richardson number presented above can not determine whether one or other group of the forcing mechanisms is the main responsible for the creation of the gravitational circulation. Stacey et al. (2001) investigated what forcing is more important by comparing the governing equation of the baroclinic driven flow (Prandle, 1991) with the magnitude of the observed gravitational flow. Assuming an unstratified water column and a timescale of the gravitational flow longer than the vertical mixing time, the authors related the baroclinic flow, u_{cl}, to the bed friction velocity as

$$u_{cl} = \frac{k_f g H^2 \lambda}{\rho u_*} \qquad [\mathrm{m\,s^{-1}}] \tag{4.4}$$

where the scale factor k_f of the order of 10^{-2} at the bed (Prandle, 1991).

In order to examine this concept in the observations from Southampton Water, a typical gravitational circulation event was chosen - the neap tide over days 105 - 110 (Fig. 4.5). During these days, the gravitational circulation over the water column was typically 0.1 $\mathrm{m\,s^{-1}}$. Assuming a depth of 15 m and the horizontal density gradient of 1.5 $\times 10^{-4}$ $\mathrm{kg\,m^{-4}}$ as a typical value at the onset of the gravitational flow, equation 4.4 leads to a friction velocity of approximately 10^{-4} $\mathrm{m\,s^{-1}}$. The typical friction velocity from the ADCP data over those days was 1 - 2 x 10^{-4} $\mathrm{m\,s^{-1}}$ (equation 3.3).

The agreement between data and the baroclinic induced u_* show that the observed mean flow can be interpreted as being consistent with gravitationally-driven baroclinic flow. This result differs from that found by Stacey et al. (2001) in San Francisco Bay, where the gravitational flow was considered to be controlled by barotropic forcing mechanisms instead. The marked semi-diurnal asymmetry, with a vertical instability on the flood tide and strong stability on the ebb (tidal straining mechanism), is considered by the authors as a key factor for the barotropic control of the onset of the gravitational flow. Although semi-diurnal variability on stratification was observed, water column does not become fully mixed during the flood tides during the gravitational flow events at the mooring site (Fig. 4.5). This status of permanent stratification may cause a comparatively weaker process of tidal straining in Southampton Water and reduce the influence of this barotropic mechanism on the control of the gravitational circulation.

An intriguing observation in Southampton Water is that the presence of shallow water tidal constituents results in an ebb-flood asymmetry in the tidal mixing. Considering the total production of the tidal turbulent energy is proportional to the cubic of the bottom tidal velocity (Simpson et al., 1996), at spring tide the production during an ebb tide is between 2 and 3 times greater than that of the flood tide. In other words, there is more mixing during the ebb tide due to the higher current speeds, which is not compensated by the longer lasting flood phase at lower speeds. During neap tides the ebb and flood tidal energy production are almost equal due to the similarity of the tidal velocities. Thus the mixing asymmetry is in the opposite sense to the typical barotropic mechanism observed by Stacey et al. (2001), where convective mixing during the flood tide provides the imbalance (Jay and Musiak, 1996).

The observed fluctuations of the Ri_x indicated an increase in the stratification driven by the baroclinic velocities during the neap tides (Fig. 3.13). This increase of the stratification dominance over the tidal mixing due to the tidal straining process seems to be essential to trigger the onset of the gravitational circulation.

For stronger longitudinal density gradient (larger river discharge) the gravitational flow was more persistent and no semi-diurnal modulation could be observed in their analysis. This latter situation was found in the Southampton Water where persistent pulses of gravitational circulation had a duration of days at the weak neap tides with no semi-diurnal modulation.

These results suggests two different situations for the occurrence of gravitational circulation in Southampton Water at higher longitudinal density gradient. Tidal mixing has to be weak ($v_b < 0.4\ \mathrm{m\,s^{-1}}$) for 1-2 days to allow an enough increase of stratification, which inhibits further mixing. Gravitational flow is able to persist until the stronger tidal mixing at neap-to-spring transition overcomes the buoyancy-driven damping of the vertical mixing and interrupts the mean flow. If tidal mixing remains above the threshold, the feedback mechanism of stronger stratification-weaker mixing does not occur and gravitational flow can not develop. It seems that for a lower longitudinal density gradient, as observed on the summer deployment, weaker stratification allows higher mixing and no gravitational circulation can develop.

Chapter 5

The numerical model experiments

This chapter presents a series of numerical experiments using a simple hydrodynamical model which simulates the effects of turbulent mixing on the mean flow of a partially mixed estuary, in particular the variability of the tidal mixing within the spring-neap and the semi-diurnal tidal cycles. The effects of the wind-induced mixing on the mean circulation are also investigated.

5.1 Introduction

Hydrodynamical numerical models have been extensively used in numerous formulations to simulate many of the processes present in estuarine systems. While any model will only be a simplified representation of the real world, the use of models in oceanography allows the a manipulation of physical processes that is not possible in the real world. Thus models are useful in investigations of how key physical processes interact, allowing processes to be added or removed, and allowing fuller exploration of the driving parameters beyond the existing observational data.

The approach taken here is to develop further understanding of the estuarine system by beginning with a very simple model and gradually increasing model complexity; i.e. following Occam's Razor, the emphasis is on the understanding of the simplest interactions before adding more complexity. After a general description of the model structure and the objectives of the modelling work, the simple balance between a barotropic pressure gradient and a longitudinal density gradient is explored. Tidal and wind-driven mixing are then added using a simple level 2 turbulence closure scheme (Mellor and Yamada, 1974). This model is then used as a tool to investigate the questions posed in the model objectives.

5.1.1 General description

The model presented here solves numerically the velocity and density vertical structure through the equations of motion and advection-diffusion of density. It is a one-dimension model in the vertical domain mainly forced by the tidal-oscillation slope, derived from tidal observation in Southampton Water. It also includes a dynamical interaction between a baroclinic term induced by the longitudinal density gradient and a counteracting non-tidal surface slope term. The vertical mixing is solved by a turbulence closure scheme, which calculates the vertical turbulent diffusivities of momentum and density, as a function of the Richardson number.

5.1.2 Objectives of the model

The main objectives of the numerical experiments in the study are:

- Verify numerically the response time for the onset and discontinuance of the gravitational circulation due to the fluctuation of the tidal mixing, via N_z, operating at the different time scales of the unusual tide present in Southampton Water.

- Quantify the role of the wind as a control on the gravitational circulation.

- Assess wether or not a simple 1-D turbulence closure model is adequate for a full description of processes acting in a partially-mixed estuary.

5.2 Equation of motion

The equation of motion describes the acceleration of water particles due to the fluctuations of the sum of all forces acting on the particles. Taking the velocity u as the sum of the large- and small-scale fluctuations, as in equation 1.10, the forces involved in the motion can be divided into large-scale forcing, driven by the fluctuations on the pressure gradient ($\partial P/\partial x$), and small-scale, due to the turbulent molecular shear and represented by the Reynolds stress, σ (section 1.4.1). Thus, adding any external forces F_{ex}, the equation of motion for the x-direction is written as

$$\frac{du}{dt} = -\frac{1}{\rho}\frac{\partial P}{\partial x} - \left(\frac{1}{\rho}\frac{\partial \sigma_{xx}}{\partial x} + \frac{1}{\rho}\frac{\partial \sigma_{xy}}{\partial y} + \frac{1}{\rho}\frac{\partial \sigma_{xz}}{\partial z}\right) + F_{ex} \qquad [\mathrm{m\,s^{-2}}] \qquad (5.1)$$

where the second term on the right hand side represents the frictional forces due to small-scale turbulent effect.

Assuming hydrostatic pressure the depth-dependent pressure $P(z)$ is given by

$$P(z) = P_0 + \rho_s g\zeta + \int_z^h \rho(z) g dz \qquad [\mathrm{N\,m^{-2}}] \qquad (5.2)$$

where P_0 is the atmospheric pressure ($\mathrm{N\,m^{-2}}$), ζ is the surface slope (m), z is the depth above the bed (m), h is the total depth (m) and ρ_s is the surface density ($\mathrm{kg\,m^{-3}}$). To be consistent with the reference grid used for the ADCP data, hereinafter the main axis of the model simulation is also considered to be in the y-direction, and the x-axis is across the estuary. Thus, the horizontal pressure gradient along the longitudinal axis (y-component) can be written as

$$\frac{\partial P}{\partial y} = \rho g\frac{\partial \zeta}{\partial y} + (h - z)g\frac{\partial \rho}{\partial y} \qquad [\mathrm{N\,m^{-3}}] \qquad (5.3)$$

The transverse and vertical large-scale velocities, respectively $\langle u\rangle$ and $\langle w\rangle$ in equation 1.10, are very small compared to the longitudinal large-scale velocity, $\langle v\rangle$. In order to satisfy continuity the term dv/dx (equation 1.13) becomes zero (Officer, 1976), and assuming lateral homogeneity, $\partial u/\partial x$ is also zero. Reynolds stress can be parametrised by the coefficient of eddy viscosity by including equation 1.13 into equation 5.1 and substituting the longitudinal pressure gradient in the first term on the right hand side of equation 5.1 by equation 5.3, the equation of motion can be written as

$$\frac{dv}{dt} = -g\frac{\partial \zeta}{\partial y} - \frac{gz}{\rho}\frac{\partial \rho}{\partial y} + \frac{\partial}{\partial z}\left(N_z \frac{\partial v}{\partial z}\right) + F_{ex} \qquad [\mathrm{m\,s^{-2}}] \tag{5.4}$$

where the first term on the right hand side is the longitudinal pressure gradient corresponding to the surface slope, i.e. the barotropic term, and the second term represents the longitudinal variation in pressure due to the longitudinal changes in density, i.e. baroclinic term. The surface slope can still be separated into two different components as

$$g\frac{\partial \zeta}{\partial y} = g\sum_{c=1}^{n} A_c \sin(\omega_c t + \phi_c) + g\frac{\partial \bar{\zeta}}{\partial y} \qquad [\mathrm{m\,s^{-2}}] \tag{5.5}$$

where the first term on the right hand side is the tidally oscillating slope which can be described by the amplitude A_c, the angular frequency ω_c, and the phase ϕ_c of the c^{th} tidal constituents c, analogous to the equation 2.7. The $\partial\bar{\zeta}/\partial y$ on the right hand side is the non-tidal mean slope which acts in opposition to the longitudinal density gradient to balance the baroclinic flow. Assuming an integrated zero net flow over the water column with no friction on the bottom, the balance between the mean barotropic and the baroclinic pressure gradients is

$$\int_0^h g\frac{\partial \bar{\zeta}}{\partial y}dz = -\int_0^h \frac{gz}{\rho}\frac{\partial \rho}{\partial y}dz \qquad [\mathrm{m\,s^{-2}}] \tag{5.6}$$

leading to

$$g\frac{\partial \bar{\zeta}}{\partial y} = -\frac{1}{2}\frac{gh}{\rho}\frac{\partial \rho}{\partial y} \qquad [\mathrm{m\,s^{-2}}] \tag{5.7}$$

which is equivalent to equation 1.8. The constant 1/2 on the right hand side can be substituted by the variable γ, called here the *surface slope coefficient*, in order to include the effects of friction on the balance. As demonstrated in section 1.2.1 γ can vary between 1/2 for a frictionless bottom situation and 3/8 for a no-slip bottom conditions. However it can reach values lower than 1/3 where the longitudinal density gradient is strong (estuaries), or greater then 3/5 where Coriolis force is important (e.g. coastal regions) (Sharples, 1992).

By substituting equation 5.7 into equation 5.5, and equation 5.5 into 5.4, the equation of motion in the longitudinal y-direction can now be expressed as

$$\frac{dv}{dt} = \text{-}g \overset{\text{TIDE}}{\sum_{c=1}^{n} A_c(y)\sin(\omega_c t + \phi_c)} + \overset{\substack{\text{NON-TIDAL}\\ \text{BAROTROP}}}{\frac{gz\gamma}{\rho}\frac{\partial\rho}{\partial y}} - \overset{\text{BAROCLIN}}{\frac{gz}{\rho}\frac{\partial\rho}{\partial y}} + \overset{\text{TURB MIX}}{\frac{\partial}{\partial z}\left(N_z\frac{\partial v}{\partial z}\right)} + \overset{\substack{\text{CORIOLIS,}\\ \text{WIND, ...}}}{F_{ex}} \quad [\mathrm{m\,s^{-2}}] \quad (5.8)$$

where the first and second terms on the right hand side are the tidal and non-tidal barotropic pressure gradient, respectively; the third term is the baroclinic pressure gradient given by the longitudinal density gradient; the forth term is the vertical turbulent mixing; and the last term includes any external force. Similarly, the equation of motion for the transverse x-direction can be written as

$$\frac{du}{dt} = -g\sum_{c=1}^{n} A_c(x)\sin(\omega_c t + \phi_c) + \frac{gz\gamma}{\rho}\frac{\partial\rho}{\partial x} - \frac{gz}{\rho}\frac{\partial\rho}{\partial x} + \frac{\partial}{\partial z}\left(N_z\frac{\partial u}{\partial z}\right) + F_{ex} \quad [\mathrm{m\,s^{-2}}] \quad (5.9)$$

Considering that the tide propagation only occurs in the y-direction and there is no lateral density gradient ($\partial\rho/\partial x = 0$), the equation of motion for the x-axis can be simplified to

$$\frac{du}{dt} = \frac{\partial}{\partial z}\left(N_z\frac{\partial u}{\partial z}\right) + F_{ex} \qquad [\mathrm{m\,s^{-2}}] \qquad (5.10)$$

5.2.1 Model grid and boundary conditions

The one dimensional vertical grid of the model is divided into a series of discrete evenly-spaced cells where the motion and the advection-diffusion equations were applied in order to solve the vertical variability of the currents and scalars. Currents and scalars are calculated for every mid-cell point and the parameters related to the turbulent motion are associated with the lower boundary of each grid cell (Fig. 5.1). The averaged depth of 15 metres was considered for Southampton Water neglecting the tidal variation. The constant depth was divided in to 10 cells, resulting in a cell size of 1.5 m.

The use of an explicit numerical integration of the equations in the model results in a less complex code but imposes a restricting condition of maximum time step. The

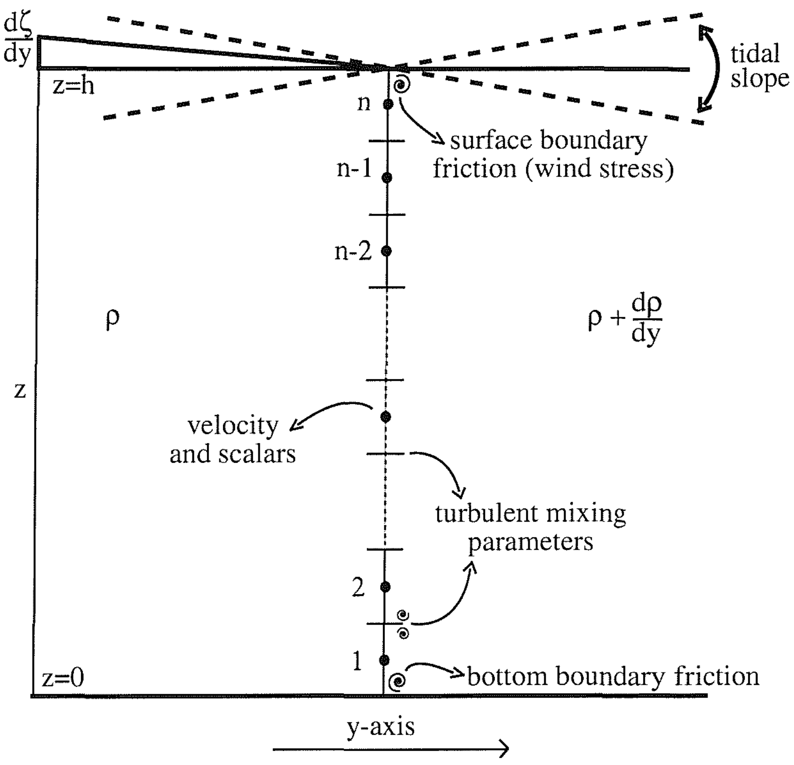

Figure 5.1: **Schematic of the model grid with the following physical processes involved: tidal slope, longitudinal density gradient ($d\rho/dy$), non-tidal slope ($d\zeta/dy$) and vertical turbulent mixing.**

maximum time step is given by

$$\Delta t < \frac{(\Delta z)^2}{2N_z} \qquad [\mathrm{s}] \qquad (5.11)$$

where Δt is the time step and Δz is the height of each vertical cell or the depth interval. The physical meaning of this maximum limit is that the model time step must be less than the time taken for a property to be mixed out of a grid cell. Considering the variability of N_z for different conditions of vertical stability, the choice of a typical maximum value of $N_z = 0.1\ \mathrm{m^2\,s^{-1}}$ was chosen. This value allows a maximum time step Δt for the model of 10 seconds.

Bottom and surface boundary conditions

A stress condition at the bottom boundary is necessary to include the effects of friction in the equation of motion due to the current flow over the solid bed. These effects are expressed in the quadratic friction bottom condition for the longitudinal and transverse axis as

$$\begin{aligned}\tau_{b(y)} &= -k_b\,\rho_b\,v_b\,\sqrt{u_b^2+v_b^2} \\ \tau_{b(x)} &= -k_b\,\rho_b\,u_b\,\sqrt{u_b^2+v_b^2}\end{aligned} \qquad [\mathrm{N\,m^{-2}}] \qquad (5.12)$$

where k_b is the bottom drag coefficient, ρ_b the density in the bottom cell, and v_b and u_b the longitudinal and the transversal near-bed velocities, respectively. For k_b the typical value of 0.003 was assumed.

At the surface boundary the friction is related to the wind stress, τ_W, decomposed in the x- and y-direction (equation 2.3), with the surface drag coefficient C_d dependent on the wind speed (equations 2.4 and 2.5).

5.2.2 The turbulent closure scheme - TCS

The advantage of using a model which includes the TCS instead of a prescribed solution is the non-arbitrary parameterisation of the feedback between water column stability and vertical turbulent mixing. A series of TCS were proposed by Mellor and Yamada (1974). These schemes have different levels of complexity depending on the degree of anisotropy in the turbulence, i.e. the spatial variance of the turbulent motion due to its advection and diffusion (Landahl and Mollo-Christensen, 1986, Lesieur, 1994).

For this work the so-called level 2 scheme is used, which is based on a local equilibrium between the production and dissipation of turbulence (i.e. it does not include the vertical diffusion of the turbulent kinetic energy). The vertical eddy viscosity, N_z, and diffusivity, K_z, are written as

$$N_z = -S_M\,l\,q \qquad [\mathrm{m^2\,s^{-1}}] K_z = -S_H\,l\,q \qquad [\mathrm{m^2\,s^{-1}}] \qquad (5.13)$$

where Sm and Sh are stability functions, l the turbulent length scale in metres and q is the turbulent velocity scale, or the turbulent intensity, in $\mathrm{m\,s^{-1}}$.

The stability functions, S_M and S_H, are dependent on the local gradient Richardson number, Ri, (equation 1.14), via a flux Richardson number, R_f, and are expressed as

$$S_M = B_1^{-1/3} \frac{(1 - R_{fc}^{-1} R_f)(1 - R_{f1}^{-1} R_f)}{(1 - R_f)(1 - R_{f2}^{-1} R_f)} \qquad (5.14)$$

and

$$S_H = \frac{B_1^{-1/3}}{P_r^N} \frac{(1 - R_{fc}^{-1} R_f)}{(1 - R_f)} \qquad (5.15)$$

where $B_1 = 15$, $R_{fc} = 0.166$, $R_{f1} = 0.25$ and $R_{f2} = 0.2$ are all empirical constants detailed by Nunes-Vaz and Simpson (1994), and the turbulent Prandtl number, P_r^N, is the ratio N_z/K_z under conditions of neutral stability, typically taken to be unity. The dimensionless flux Richardson number, R_f, is

$$R_f = \frac{1}{2}\left[R_{f1} + R_i R_{f1} R_{f2}^{-1} - \left((R_{f1} + R_i R_{f1} R_{f2}^{-1})^2 - 4 R_{f1} R_i\right)^{1/2}\right] \qquad (5.16)$$

The turbulent length scale, l, can be thought of as describing the typical spatial scale of turbulent eddies in the water column. It represents the fact that turbulent eddies are not a local small-scale phenomenon, but rather larger scale eddies which may occupy a significant part of the water column. The only limitation on size of the eddies is that it must be equal to κz towards the boundaries (Mellor and Yamada, 1974), with κ being the dimensionless von Karman's constant ($= 0.41$) and z the height above the bed. Sharples and Simpson (1995) analysed different methods for calculating l and observed that some forms (Chen et al., 1988, Mofjeld and Lavelle, 1984) underestimate vertical mixing in shallow water. More realistic results were found from the formulations by Galperin et al. (1988) and Davies (1990). The former incorporates l into the turbulent kinetic energy equation while the latter calculates it from a direct function of κ as

$$l(z) = \kappa z \left(1 - \frac{z}{h}\right)^{\frac{1}{2}} \qquad [\mathrm{m}] \qquad (5.17)$$

Thus the preference for using equation 5.17 was based on its simplicity for solving satisfactorily the l calculation (Sharples and Simpson, 1995). The above formulation results in a parabolic profile of the turbulent length scale biased towards the surface and reduced towards both the surface and the bottom boundaries (Fig. 5.2). This profile describes the typical spatial scale taken up by turbulent eddies and limited by the proximity of the boundaries.

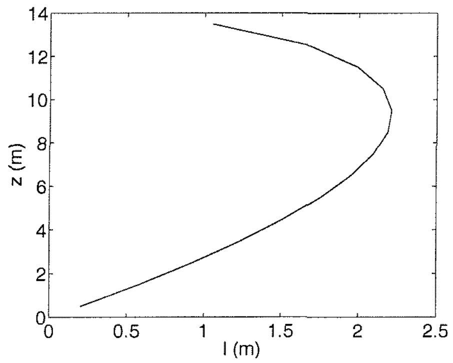

Figure 5.2: **Vertical profile of the turbulent length scale l (m) for the average depth of the Southampton Water (h = 15 m) calculated from equation 5.17.**

The level 2 TCS determines the turbulent intensity, q, from the simplified turbulent kinetic energy equation (Chen et al., 1988), here neglecting the transverse x-axis

$$S_M\, l\, q \left(\frac{\partial v}{\partial z}\right)^2 + S_H\, l\, q \left(\frac{g}{\rho}\frac{\partial \rho}{\partial z}\right) = \frac{q^3}{B_1 l} \qquad [\mathrm{m}^2\ \mathrm{s}^{-3}] \qquad (5.18)$$

Equation 5.18 describes the balance between the shear and the buoyancy production of the turbulent kinetic energy, respectively the first and the second terms on the left hand side, and the turbulent dissipation, on the right hand side. This balance assumes that the production of turbulent motion is dissipated locally and instantaneously, with no advection or diffusion of turbulent energy. However, as the shear can become negligible during the slack water periods of the tide, the assumption of local equilibrium between production and dissipation can result in very small values of N_z and K_z. Once this very low shear condition occurs, the runaway stratification cannot be prevented as Ri tends to remain greater than 0.5 (Sharples, 1992). The simplest way to overcome this problem is to set a lower limit to N_z, preventing the turbulent viscosity falling below a background level. The choice of the background N_z is normally done by adjusting this parameter purely based on comparisons between the results of the model and observations.

5.3 Preliminary tests on the model outputs

Before the use of the model including the TCS some preliminary tests were carried out to check the model's operations. The capacity of the model in reproducing the unusual tidal currents in Southampton Water was tested. The modelled solution to the balance between non-tidal slope and longitudinal density gradient was also analysed, allowing the setting of the surface slope coefficient, γ, as a function of the horizontal mean flow.

5.3.1 Reproducibility of the tidal current

The oscillating tidal elevation used in the model was derived from the tidal velocity calculated by the least square harmonic analysis of the depth-averaged ADCP velocity. The harmonic constituents have described in Table 2.2.

In order to investigate the effects of the spring-neap and semi-diurnal fluctuations of the tidal mixing on the gravitational circulation the model must reproduce the major features of the complex tidal currents in Southampton Water. To test if the tidal velocity output from the model agreed with observations, the mean slope and density-driven flow were initially not included. Thus the velocity output was purely driven by the tidal elevation assuming a constant mixing ($N_z = 2.5 \times 10^{-2}$ m^2 s^{-1}).

The modelled velocities driven by the tidal barotropic gradient have a good fit with the ADCP raw data, following the observed semi-diurnal variability at both spring and neap tides (Fig. 5.3). The root mean square of the difference between data and model output over the period analysed (rms_{48h}) is 0.02 and 0.01 m s^{-1} at spring tide and 0.04 and 0.02 m s^{-1} at neap for surface and bottom velocities, respectively. The larger difference at the surface during the neap tide is due to the underestimation of the peak of the ebb velocity by the model (Fig. 5.3b - days 92.4 and 92.9).

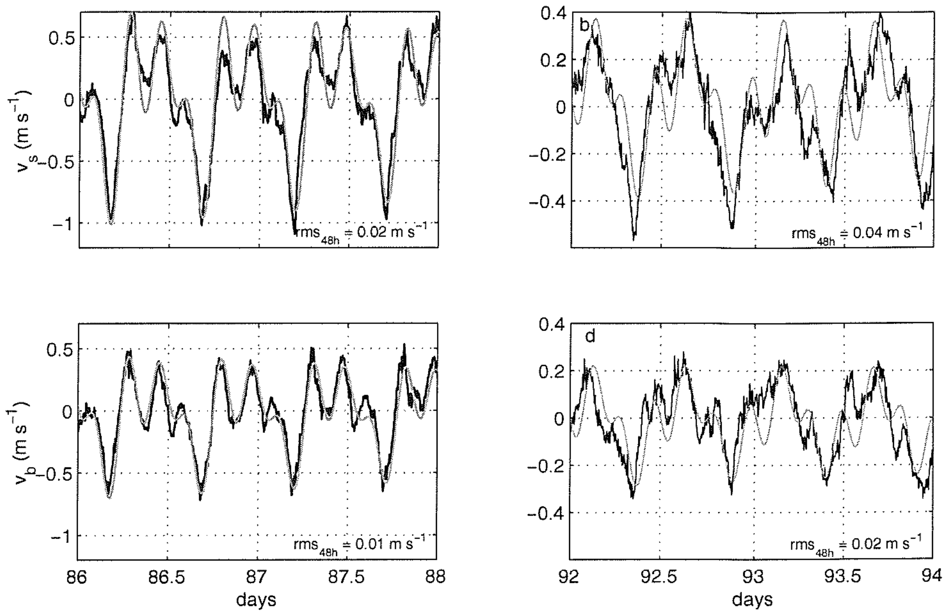

Figure 5.3: **Tidal velocities at surface, v_s, (a and b) and bottom, v_b, (c and d) during a 48-h period at spring (a and c) and neap (b and d) tides. Black line shows the ADCP raw data from the spring deployment and gray line shows the modelled tidal velocity. The difference between data and model is indicated by the root mean square over the period (rms_{48h}). Time-domain axis is based on the ADCP time series.**

5.3.2 Balance between non-tidal slope and longitudinal density gradient

In order to achieve the zero net flow boundary condition, the baroclinic flow induced by the longitudinal density gradient, λ, has to be counteracted by the barotropic flow induced by the non-tidal surface slope, $d\zeta/dy$. This balance is determined by the surface slope coefficient, γ, and is described for the particular conditions of non-slip ($\gamma = 3/8$) and frictionless bottom ($\gamma = 1/2$) of the Hansen-Rattray solution in equations 1.5 and 1.8, respectively. Driscoll et al. (1998) found both the horizontal and the vertical structure of the flow very sensitive to the choice of the bottom boundary condition and Sharples (1992) suggested the need to calculate γ according to the averaged net flow in order to retain no net flow. To adjust γ for the zero mean flow condition the following equation was applied at each time step t

$$\gamma(t) = \gamma(t-1) - F\overline{u(t)} - D\left[\overline{u(t)} - \overline{u(t-1)}\right] \tag{5.19}$$

where F and D are the feedback and the damping factors and $\overline{u(t)}$ is the depth mean velocity at t time step. The units of F and D have to be s m^{-1} in order that γ be non dimensional.

In order to choose the values for the factors F and D in equation 5.19 the time-response of the depth-averaged velocity to a change of N_z was compared for different adjustments of γ. An initially vertically homogeneous condition was modelled with a longitudinal density gradient of 10^{-4} $\mathrm{kg\,m^{-4}}$ and a jump of N_z from 0.01 to 0.1 $\mathrm{m^2\,s^{-1}}$ after day 1 of model simulation. For γ constant ($= 0.5$) the surface slope does not balance λ and the resulting depth mean flow is not zero (Fig. 5.4a,b). By allowing gamma to change in response to the mean flow it is possible to achieve a zero mean flow (Fig. 5.4c,e,g), although the time response depends on the choice of F and D (Fig. 5.4d,f,h). This zero mean flow condition is important to keep the barotropic term of the equation 5.8 as low as possible. Higher F allows a faster response of γ to the change of N_z, but can also lead to oscillatory "hunting" of gamma towards the required value. The factor D is used to damp this oscillatory behaviour.

Values of F and D were chosen to be 5 and 100 s m^{-1} respectively. These constants typically resulted in an adjustment time scale of less than 1 hour (Fig. 5.5). By forcing this adjustment to operate on the same time scale as the tidal current variability the model is able to keep the gravitational flow responding to the semi-diurnal variability of the mixing.

5.4 Configuration of the TCS model

Initial experiments with the TCS model highlighted a significant problem with the effect of the TCS if no constraints were imposed on the range of Ri or Nz available to the model. For instance, the ratio between the buoyancy frequency N^2 and the velocity shear S^2, Ri (see equation 1.14), is a key parameter in determining the turbulent coefficients

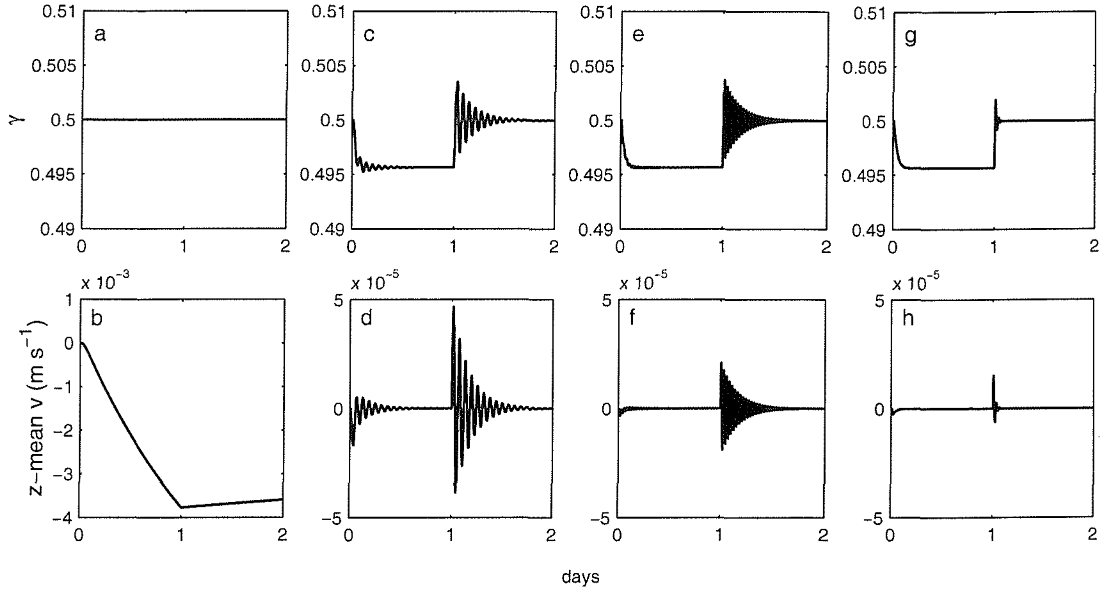

Figure 5.4: **Surface slope coefficient γ (a,c,e,g) and depth-mean velocity (b,d,f,h) for four different situations of γ adjustment: no adjustment, with γ constant (a and b); $F = 1$ and $D = 10$ s m^{-1} (c and d); $F = 5$ and $D = 10$ s m^{-1} (e and f); and $F = 5$ and $D = 100$ s m^{-1} (g and h). $N_z = 0.01$ m^2 s^{-1} at time 0-1 day and 0.1 m^2 s^{-1} at time 1-2 day, $\lambda = 10^{-4}$ kg m^{-4} and initial $\gamma = 0.5$.**

used by the TCS. High *Ri* means stratification is strong enough to inhibit any vertical propagation of the turbulent motion. In the model this leads to runaway stratification, with no vertical mixing at all.

On the other hand, very low *Ri* ($S^2 \gg N^2$) can result in high N_z and possible contravention of the model stability condition (equation 5.11). A solution is to impose a range of *Ri* allowable for the model, or alternatively to impose maximum and minimum values for Nz. The latter approach is frequently taken by other workers using TC schemes (Simpson and Souza, 1995, Sharples and Simpson, 1995). It has generally been justified in terms of the existence of mixing processes not present in models (e.g. internal waves), and as a requirement to maintain numerical stability at the same time as using a practical model time step. The full range of the TCS modelled *Ri* can be seem by considering a plot of the stability function, *Sm*, as a function of *Ri* (Fig. 5.6). The critical *Ri* above which all mixing is stopped by the TCS is 0.33. *Ri* can become negative (with

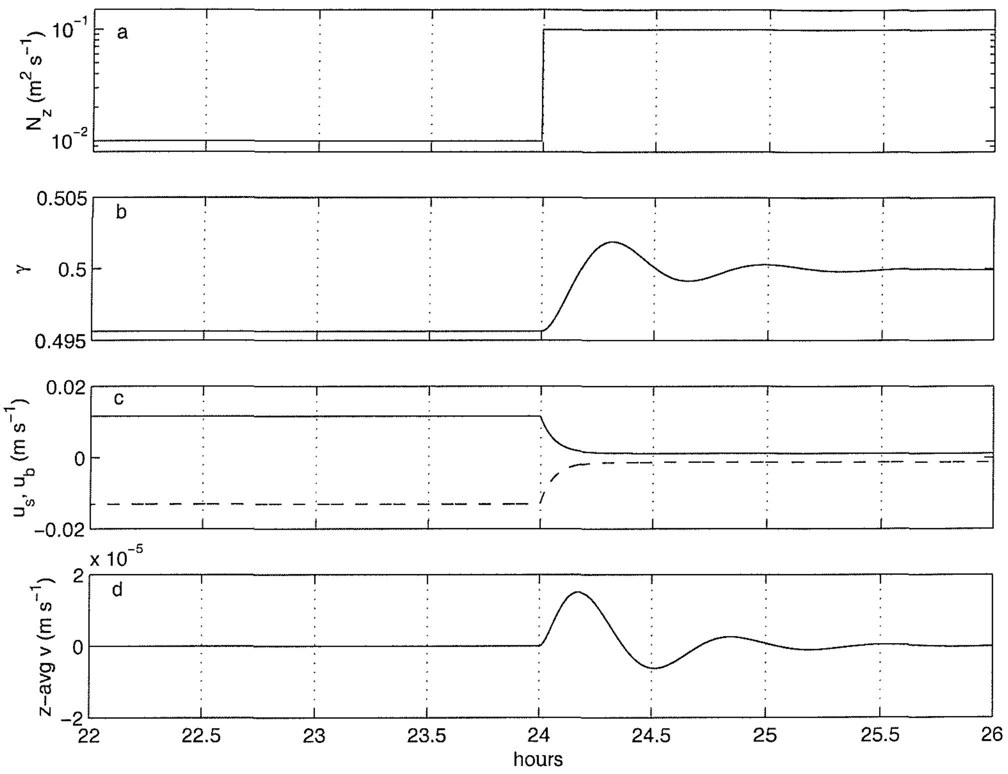

Figure 5.5: 4-hour period of (a) the N_z input variability, (b) the γ adjustment for $F = 5$ and $D = 100$ s m^{-1} in equation 5.19, (c) the bottom (bold line) and surface (dashed line) velocity, and (d) the depth-averaged velocity; showing the response time on the density-driven circulation to a change on the vertical mixing at time = 24 hours. Tidally-driven elevation was not included and λ was 10^{-4} kg m^{-4}.

correspondingly larger Sm) in regions of convective instability.

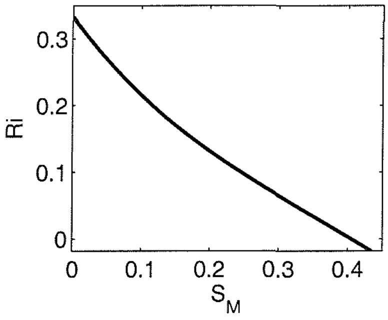

Figure 5.6: The Richardson number Ri plotted against the local stability function of momentum S_M, showing the limits of Ri used in the model runs.

As Ri approaches the critical value of 0.33, the viscosity decreases to very low values. Without limiting N_z to some prescribed minimum background level the model would not be able to recover from an increasingly stratified state. The choice of the background N_z was based on testing the strength of the gravitational circulation for different values, considering a constant longitudinal density gradient. The model responds very sensitively to small variations in the background eddy viscosity. For the mean longitudinal density gradient of 2.5×10^{-4} kg m^{-4}, based on the spring (Fig. 3.4f) and winter (Fig. 3.8e) deployments, the model was able to simulate the effects of the mixing on the gravitational flow only in a narrow band of values of background viscosity. For $N_z < 10^{-3}$ m^2 s^{-1} the density-driven flow accelerates and stability damps vertical mixing. On the other hand, with a background N_z more than 4×10^{-3} m^2 s^{-1} the water column remains fully mixed. The best performance in reproducing the balance between stratification and mixing was achieved for a background eddy viscosity of 2.5×10^{-3} m^2 s^{-1}, which has been used in all the numerical experiments presented in this study. This value of background eddy viscosity is more than one order of magnitude larger than in other studies (Sharples and Simpson, 1995). A possible reason for the need of such a high background N_z is the strong and persistent stratification in the shallow Southampton Water.

To test the ability of the model to simulate the gravitational circulation a 25-h averaged profile of the modelled velocity at neap tide was compared to the analytical solution of the gravitational circulation described in section 1.2.1 (Hansen and Rattray, 1965), applying a N_z of 2.5×10^{-3} m^2 s^{-1}. This value is similar to the maximum N_z output during the modelled neap tide. It shows that the modelled mean flow is in satisfactory agreement with the theoretical solution of the density-driven flow (Fig. 5.7).

The difference observed at the bottom is caused by the model adjustment of the surface slope coefficient, γ. This coefficient is tuned to achieve the zero mean flow condition in the model instead of the fixed value of 0.375 for the non-slip bottom condition at the theoretical solution.

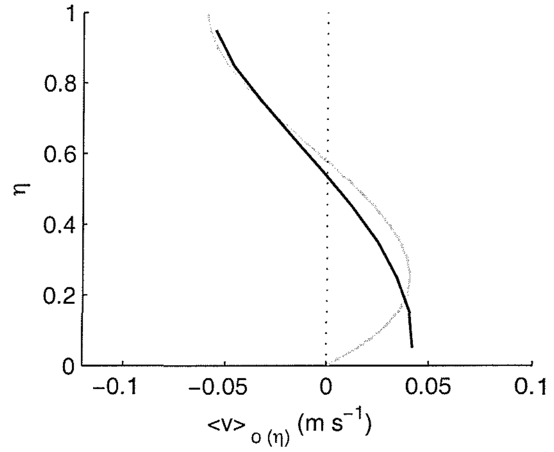

Figure 5.7: **Vertical profiles of the 25-h mean density-driven velocity from the modelled output at neap tide (black line) and calculated by the Hansen-Rattray solution (gray line). λ is 2.5 $\times$ 10^{-4} kg m^{-4} and N_z is 2.5 $\times$ 10^{-3} m^2 s^{-1} for both model (background N_z) and H-R solution. The normalised depth η is zero at the bottom and seaward velocities are negative.**

5.4.1 The numerical experiments

A series of different experiments were carried out to investigate the principal points of the relation between vertical mixing and the presence of gravitational circulation observed during the field work and described in chapters 3 and 4. These experiments were: (1) the effects of the tidal mixing on the presence and persistence of the gravitational circulation; (2) the response of the gravitational circulation to changes of the longitudinal density gradient; and (3) the effects of the variability of the direction and intensity of the wind on the resulting net flow.

Following the monthly modulation of the observed tidal currents two extremes of the tidal inputs were used in the model. Ebb bottom currents at weak neap tide were chosen to be below 0.3 m s^{-1} while strong neap currents were set higher than 0.45 m s^{-1}. These two tidal situations were set to test the effects of the different spring-neap variability of the tidal mixing on the gravitational circulation.

In order to verify the possible effects of the observed variation of the longitudinal density gradient two different freshwater discharge scenarios were set. For the higher river flow observed in the spring/2001 and winter/2002 λ was set to be 2.5×10^{-4} $\mathrm{kg\,m^{-4}}$ while for the lower river flow of the summer-autumn/2001, $\lambda = 1 \times 10^{-4}$ $\mathrm{kg\,m^{-4}}$.

Effects of wind-induced turbulent mixing were analysed in three different scenarios: (1) the dependence of mixing on the wind-direction in a straight estuary such as Southampton Water; (2) the effects of the persistence of a steady wind on the gravitational flow; and (3) the response of the gravitational circulation to different wind speed.

The modelled scenarios and their respective values of longitudinal density gradient, λ, maximum bottom velocity at neap tide, *max neap* v_b, and wind stress, τ_W, are described in the Table 5.1.

Table 5.1: **Values of the longitudinal density gradient, maximum bottom velocity at neap tide and wind stress for different numerical experiments. The background eddy viscosity was set as 2.5×10^{-3} $\mathrm{m^2\,s^{-1}}$ for all cases.**

experiment	λ *(kg m^{-4})*	*max neap* v_b *(m s^{-1})*	τ_W *(N m^{-2})*
WEAK NEAP - NO WIND			
A1	2.5×10^{-4}	0.3	0
A2	1×10^{-4}	0.3	0
STRONG NEAP - NO WIND			
B1	2.5×10^{-4}	0.45	0
B2	1×10^{-4}	0.45	0
WEAK NEAP - LANDWARD WIND			
C1 to **C9**	2.5×10^{-4}	0.3	0.18
WEAK NEAP - SEAWARD WIND			
D1 to **D9**	2.5×10^{-4}	0.3	0.18
WEAK NEAP - TRANSVERSAL WIND			
E1 to **E9**	2.5×10^{-4}	0.3	0.18
WEAK NEAP - LANDWARD WIND			
F1 to **F4** - 6-h wind	2.5×10^{-4}	0.3	0.02 to 0.3
G1 to **G4** - 12-h wind	2.5×10^{-4}	0.3	0.02 to 0.3
H1 to **H4** - 18-h wind	2.5×10^{-4}	0.3	0.02 to 0.3

The duration of each simulation was set to 21 days starting before a spring tide, allowing a spring-neap-spring transition after discarding 2 days due to the spin-up of the model. The initial condition of stratification for all experiments was a linear profile varying from 1026 $\mathrm{kg\,m^{-3}}$ at the bottom to 1023 $\mathrm{kg\,m^{-3}}$ at surface, which is the mean bottom-surface difference observed.

5.5 Results

This section describes the results of the 21-day numerical simulations (Table 5.1). For the experiments involving tidally-induced mixing (**A** and **B**), an output of the bottom tidal current, bottom eddy viscosity and bottom-surface density difference are shown. Results from the gravitational term of the model, which includes from the second to the fifth terms on the right hand side of equations 5.8 and 5.9, and tidally-averaged velocity (see section 3.1) are also exhibited. The first two days of the output time-series were omitted due to the spin-up of the model. Results about the effects of the wind are also presented (experiments **C** to **H**) although in these cases time series of the model output are not shown.

5.5.1 Tidal control on the gravitational circulation

The output for weak currents at neap tide and high river discharge (experiment **A1**) shows the typical spring-neap variability of bottom current (Fig. 5.8a). The eddy viscosity at the bottom cell (Fig. 5.8b) also presents the fortnightly variation reflecting the tidal-induced mixing. Although bottom-surface density difference is well below observations (e.g. Fig. 3.4c), it does show an increase of the stratification during the lower mixing period at neap around day 12, followed by a decrease towards the next spring tide (Fig. 5.8c).

The model output of the density-driven flow, calculated through the second and third terms in the equation 5.8, shows the increase of the bi-directional flow in the spring-to-neap transition from day 4 to day 10 (Fig. 5.8d). There appears to be a threshold in the maximum density-driven current around -0.1 $\mathrm{m\,s^{-1}}$ in the surface and 0.08 $\mathrm{m\,s^{-1}}$ in the bottom. These values represent the maximum possible flow driven by the imposed longitudinal density gradient during the time of the very low turbulent mixing, when N_z assumes the background value (Fig. 5.8b). The weakening of the gravitational circulation

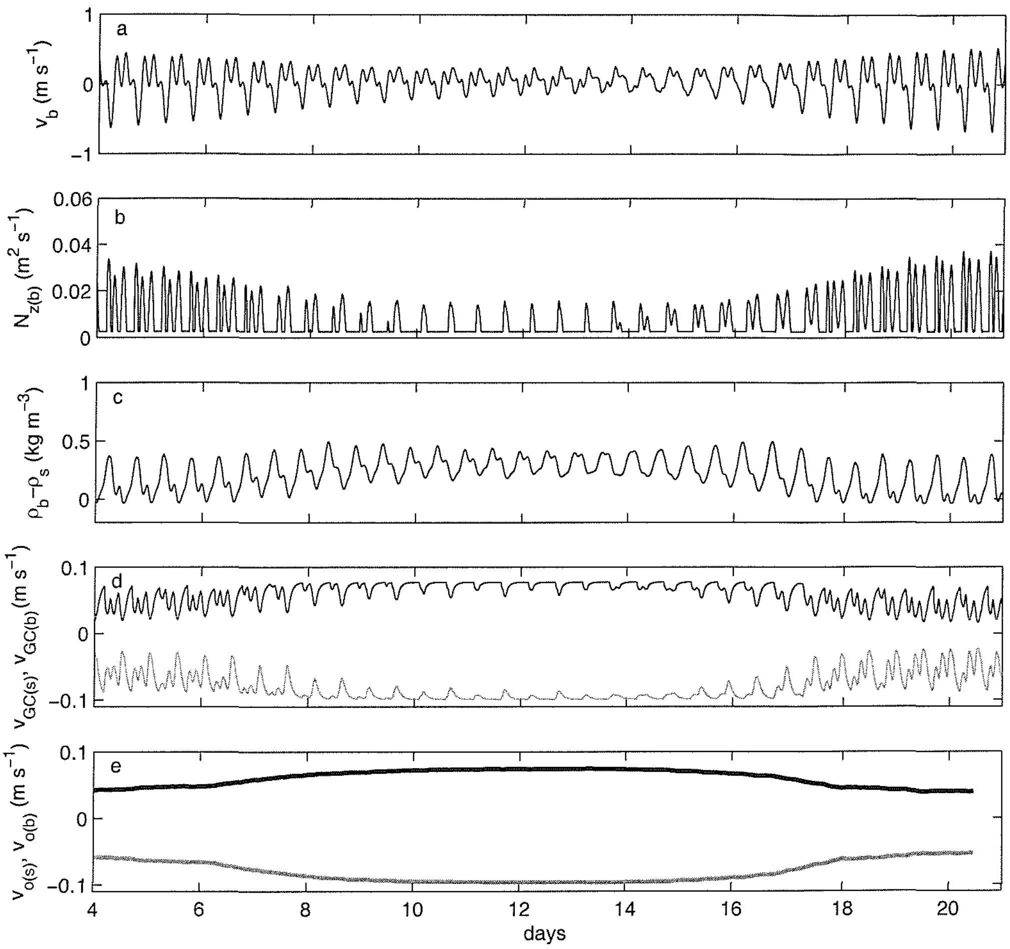

Figure 5.8: **21-day model output for the A1 experiment showing the spring-neap variation of (a) the bed velocity v_b, (b) the near-bed eddy viscosity $N_{z(b)}$, (c) the bottom-surface density difference $\rho_b - \rho_s$, (d) the surface (gray) and bottom (black) density-driven velocity, v_{GC}, and (e) the surface (gray) and bottom (black) tidally-averaged velocity, v_o.**

after day 15 is due to stronger tidal mixing caused by the increase of the bed currents toward the following spring tide. In order to compare modelled and observed results the tidally averaged velocity was calculated by the same methods applied to the data, described in the section 3.1. It shows the spring-neap modulation with the bottom-surface difference of the tidally averaged velocity varying from 0.08 m s^{-1} at spring tides to 0.18 m s^{-1} at neap (Fig. 5.8e), which compares with typical values in the observations of around zero averaged flow at springs and 0.2 m s^{-1} under a gravitational flow situation at neap tide (day 105 on Fig. ??h).

Experiment **A2** repeats **A1** settings but with a lower longitudinal density gradient of 1×10^{-4} kg m^{-4}. This value is comparable with the mean λ observed during the summer deployment when the river discharge was weaker (see Figs. 3.6e and 3.18). There is no change of mixing as the tidal bed currents and eddy viscosity are the same in both **A1** and **A2**. However stratification is greatly reduced for the low λ scenario (Fig. 5.9a,b,c).

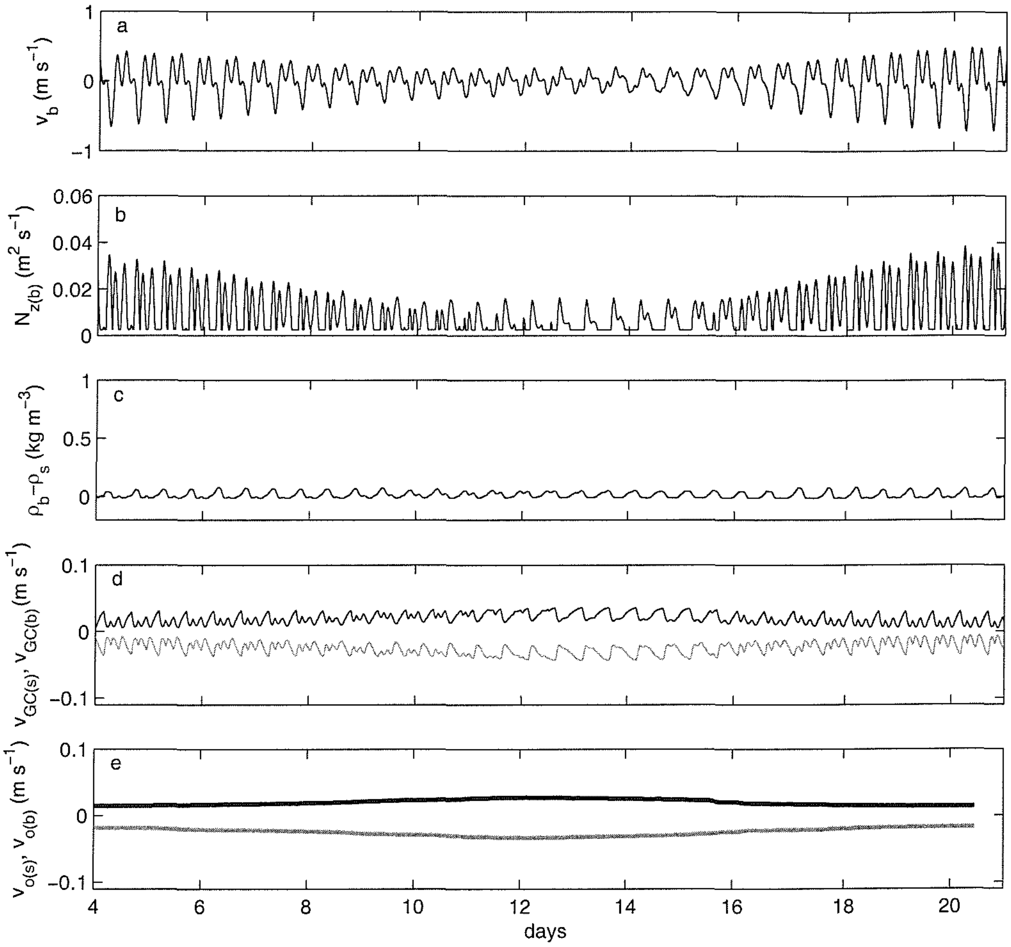

Figure 5.9: **Same as Fig. 5.8 for the A2 experiment.**

The lower density gradient affects the strength of the gravitational circulation throughout the whole spring-neap tidal cycle independently of the fluctuations of the tidal mixing. Effects of the smaller freshwater input are seen in both the density-driven current output and the tidally averaged velocity (Fig. 5.9d,e). The difference between the modelled surface and bottom density-driven components of the flow (Fig. 5.9d) shows semi-diurnal variability ranging between 0.04 and 0.07 m s^{-1}, compared to values always above 0.15 $\mathrm{m\,s^{-1}}$ for the higher density gradient (Fig. 5.8d). Those effects can also be observed in the time series of tidally-averaged bottom-surface shear $v_{o(b)} - v_{o(s)}$ for higher and lower longitudinal density gradients. It shows that the decrease in λ from 2.5 to 1 $\times$ 10^{-4} $\mathrm{kg\,m^{-4}}$ results in the gravitational flow in the low gradient case decreasing to about 30% of that in the high gradient case. This reduction is present throughout the whole spring-neap tidal cycle, with the $v_{o(b)} - v_{o(s)}$ shear decreasing from 0.06 to 0.01 $\mathrm{m\,s^{-1}}$ at spring and from 0.14 to 0.03 $\mathrm{m\,s^{-1}}$ at neap tide.

The effects of the stronger neap tide currents on the onset of the density-driven flow are investigated for $\lambda = 2.5 \times 10^{-4}$ $\mathrm{kg\,m^{-4}}$ in the **B1** experiment, with bottom velocity higher than 0.45 $\mathrm{m\,s^{-1}}$ at neap tide (Fig. 5.10a). This scenario is analogous to the observational case of the stronger neap tides during each month. The resulting tidal mixing and stratification do not have any clear variability at the transition from spring to neap (Fig. 5.10b,c). The maximum N_z for each tidal cycles remains above 0.02 $\mathrm{m^2\,s^{-1}}$.

The **B1** model output for the gravitational circulation does not show long-term variability, except for the small reduction of the density-driven currents after day 14 (Fig. 5.10d), with the 25-h averaged gravitational flow varying from 0.05 to 0.04 $\mathrm{m\,s^{-1}}$ for $v_{GC(b)}$ and from -0.05 to -0.03 $\mathrm{m\,s^{-1}}$ for $v_{GC(s)}$. The strengthening of the tidal currents toward the second spring, with the maximum v_b within a semi-diurnal cycle increasing from 0.45 on day 12 to 0.85 $\mathrm{m\,s^{-1}}$ on day 18, is most likely to be the cause for this reduction. The tidally-averaged velocity, calculated from the model output, shows a variation only during the same neap-to-spring transition, with $v_o(s)$ varying from -0.08 to -0.04 $\mathrm{m\,s^{-1}}$ and $v_o(b)$ from 0.06 to 0.02 $\mathrm{m\,s^{-1}}$ (Fig. 5.10e).

Compared with the **B1** experiment, in the **B2** experiment (reduced λ) both the bed tidal velocity and eddy viscosity are unchanged (Fig. 5.11a,b). In spite of the same turbulent tidal mixing, the water column remains fully mixed due to the lower λ (Fig. 5.11c). No spring-neap modulation can be identified in the model output of the density-driven velocity nor in the tidally-averaged velocities, with $v_{o(s)} <$ -0.03 $\mathrm{m\,s^{-1}}$ and $v_{o(b)} < 0.02$ $\mathrm{m\,s^{-1}}$ (Fig. 5.11d,e).

Vertical profiles of the 25-h averaged tidal velocity $< v >$ were calculated for the

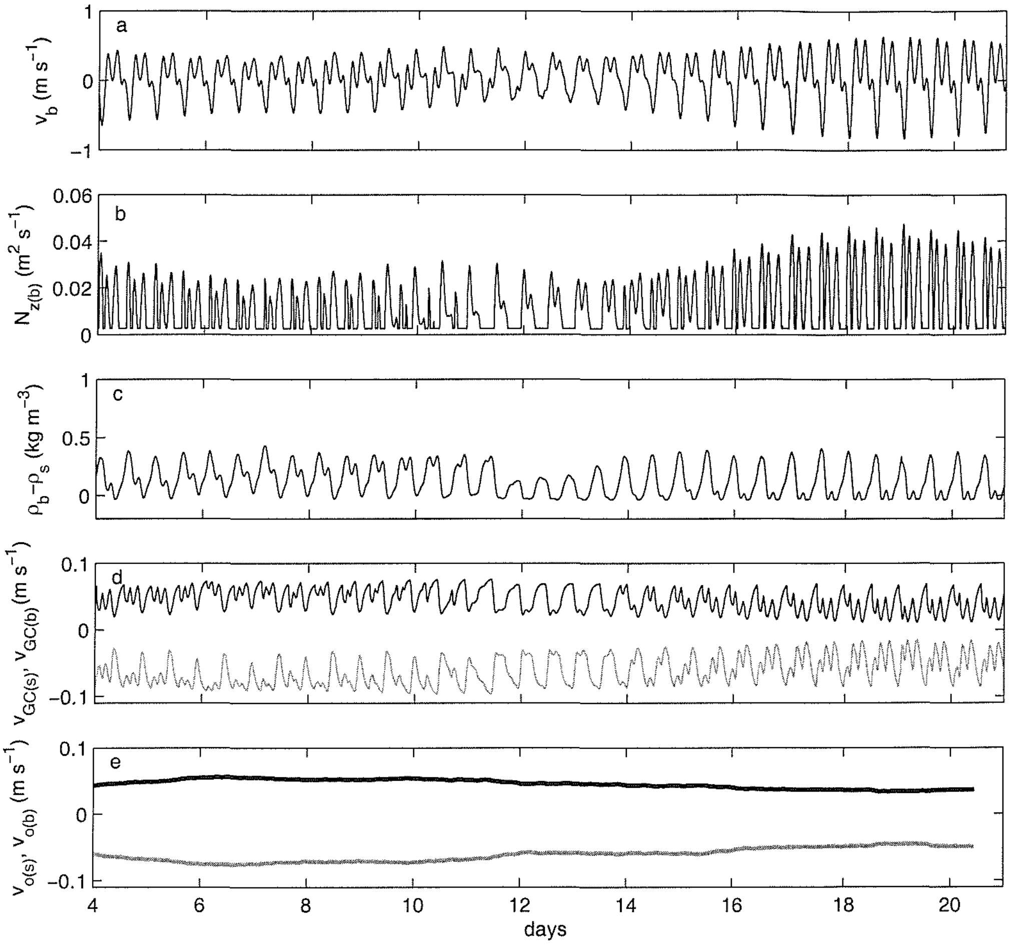

Figure 5.10: **Same as Fig. 5.8 for the B1 experiment.**

B1 and **B2** experiments, in order to compare the net flow at spring and neap tides, day 19 and day 12 of the model output respectively (Fig. 5.12). Bi-directional flow coherent with gravitational circulation is present at all tidal cycles, though with variable strength. Greater difference between spring and neap is observed for the weak tidal currents at neap ($v_{b(EBB)} < 0.3$ m s^{-1}), with the net flow being twice at neap than at spring ($v_{b(EBB)} >$ 0.9 m s^{-1}) in both surface and bottom. The neap-to-spring reduction of the 25-h mean velocity ranges from -0.1 to -0.05 m s^{-1} at surface and from 0.07 to 0.04 m s^{-1} at bottom in the **A1** experiment (Fig. 5.12a) and from -0.03 to -0.02 m s^{-1} at surface and from 0.03 to 0.01 m s^{-1} at bottom in the **A2** (Fig. 5.12b). The cause of the lower mean velocities in the **A2** experiment is the reduced longitudinal density gradient. Meanwhile a much smaller spring-neap contrast in density-driven flow is seen when bed currents stay above

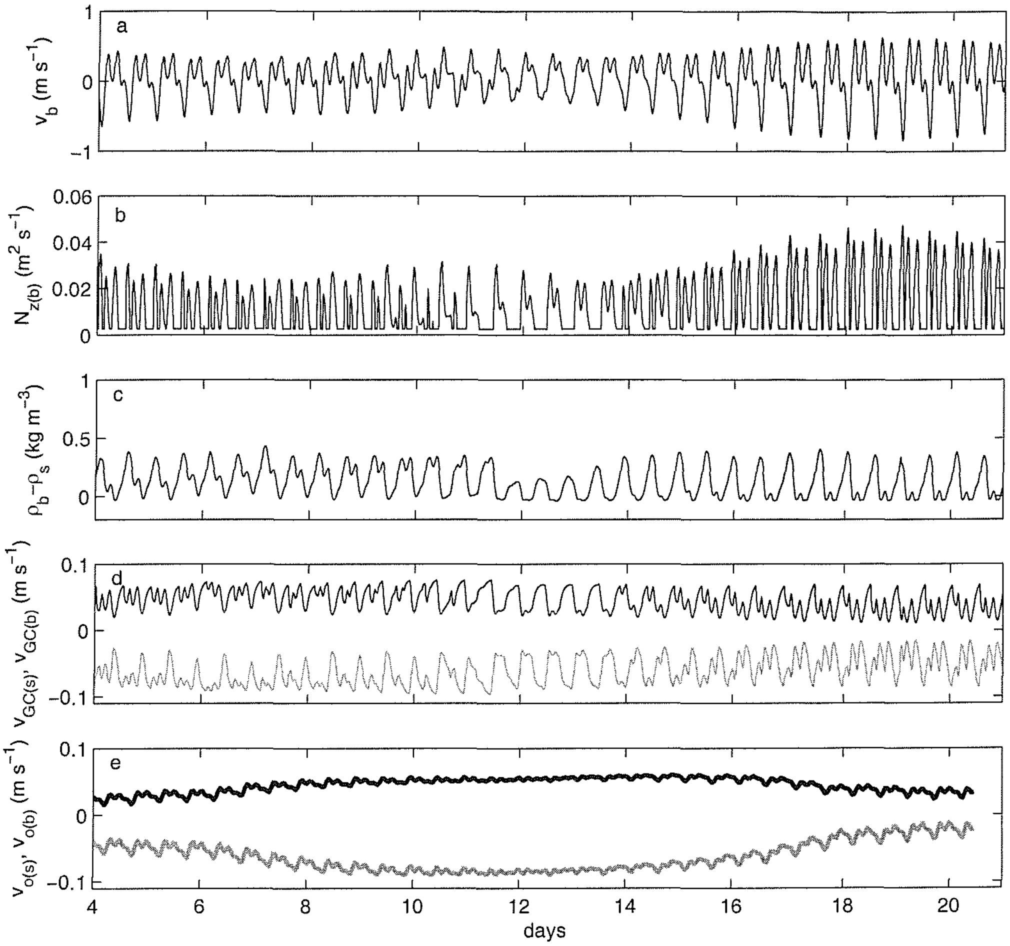

Figure 5.11: **Same as Fig. 5.8 for the B2 experiment.**

0.45 m s^{-1} at the neap tide. For $\lambda = 2.5 \times 10^{-4}$ kg m^{-4} (experiment **B1**) the maximum difference between neap and spring density-driven velocities is 0.01 m s^{-1} (Fig. 5.12c). For lower λ the mean velocity profile is very weak, with absolute values of mean velocities being around 0.01 m s^{-1} and the difference between spring and neap tides is negligible (Fig. 5.12d).

The spring-neap modulation of stratification is clearly observed in experiment A1 (weak neap tide, strong lambda; Fig. 5.13a), with the bottom-surface difference being twice as high at neaps compared to spring. For stronger v_b (experiment B1) the neap tide mean density profile is very close to the spring tide profile, i.e. showing very little spring-neap modulation (Fig. 5.13c). The modelled stratification becomes negligible for

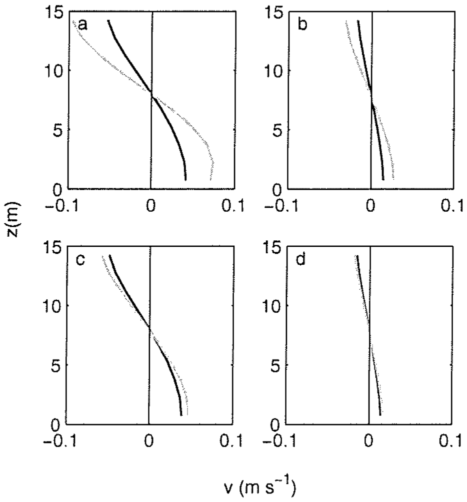

Figure 5.12: **25-h averaged profile of tidal velocity for day 19 at spring (black) and day 12 at neap (gray) tides showing the mean vertical velocity distribution for the experiments (a) A1, (b) A2, (c) B1 and (d) B2.**

the lower λ experiments at both spring and neap tides as response to the lower buoyancy forcing (Fig. 5.13b,d). While the model appears to be useful in highlighting aspects of the link between tidal mixing, the horizontal density gradient, and the gravitational circulation, it is clear that the modelled vertical density structure is far weaker than that observed. The 25-h averaged bottom-surface density difference observed in the spring deployment ranged from 2 $\mathrm{kg\,m^{-3}}$ at the spring tides to 5 $\mathrm{kg\,m^{-3}}$ at the weak neap tides (Fig. 3.4c), while the modelled stratification for a similar conditions of longitudinal density gradient (experiments **A1** and **B1**) reached values one order of magnitude weaker than these values (Fig. 5.13a,c). Possibly this underestimated stratification in the model results is caused by the need of including a background N_z, which can keep vertical mixing stronger than observations during slack periods of the tidal cycle.

In spite of this disagreement the model is able to reproduce qualitatively some of the effects of different tidal currents on the variability of the stratification, such as the increase of stability at weak neap tides and the semi-diurnal fluctuation. This link between stratification and tidal mixing was also found by Sharples and Simpson (1995) in their level 2 TCS model though with a much better observation/model agreement. However the comparison between the model results and the field observations is not valid for the lower λ experiments as there is no bottom density measurements for this scenario presented during the summer deployment (see section 3.2.2).

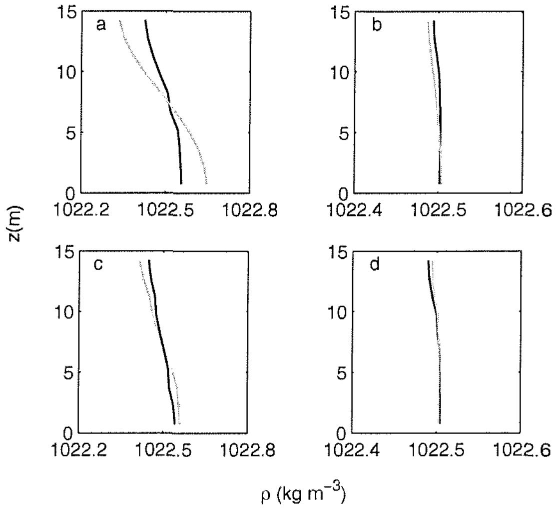

Figure 5.13: **25-h averaged profile of density for spring (black) and neap (gray) tides showing the mean vertical density distribution for the experiments (a) A1, (b) A2, (c) B1 and (d) B2. Note the different scales for x-axes.**

For the analysis of the semi-diurnal variability of the modelled gravitational circulation the output from the high λ-low neap v_b scenario (**A1** experiment) is used. It should be noted that this analysis is potentially compromised by the need to impose a background eddy viscosity. Once N_z assumes the background value at low current periods at slackwater, and particularly near neap tides, the density-driven flow reaches its maximum velocity and no further increase is possible (Fig. 5.14a,c,e). The only pulse of N_z observed at neap tide is associated with the velocity peak during the second flood around days 12.2 and 12.7. During the spring tide N_z attains higher values driven by the stronger ebb and flood currents. However the background value still occurs during the slack water periods (Fig. 5.14b,d). This semi-diurnal fluctuation of the mixing induced a modulation of the density-driven velocity (Fig. 5.14f).

The model reproduced the observed influence of the tidal current on the gravitational circulation. Occurrences of stronger shear velocity v_g follow the reduction of the maximum bottom velocity within a tidal cycle (Fig. 5.15). Despite the overestimated gravitational flow in the model results, the behaviour of the shear velocity in the **A1** and

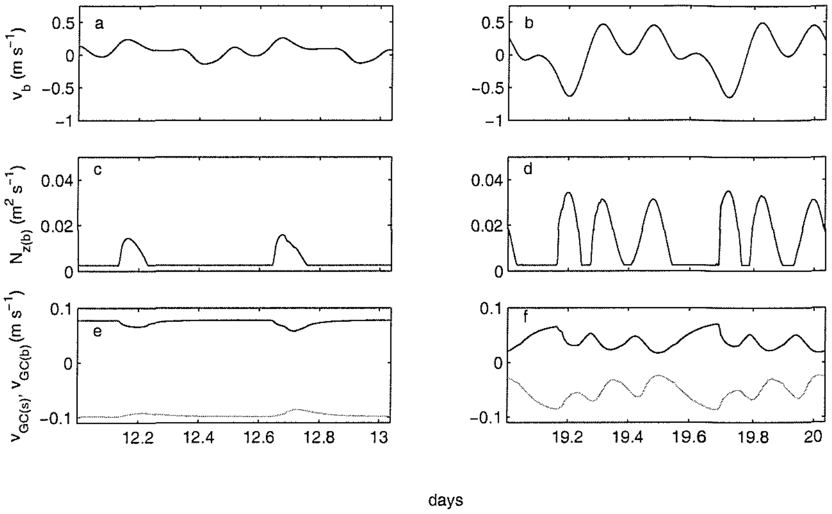

Figure 5.14: **25 hour model output of bottom velocity v_b (a,b); near-bottom eddy viscosity $N_{z(b)}$ (c,d); and bottom (black) and surface (gray) density-driven currents v_{GC} (e,f). Neap tide is on the left-hand side (a,c,e) and spring tide is on the right-hand side (b,d,f). Results are from the A1 experiment ($\lambda = 2.5 \times 10^{-4}$ kg m^{-4}; neap $v_b < 0.3$ m s^{-1}; no wind).**

B1 experiments agreed with observations under typical λ regime (see Fig. 3.12). For reduced longitudinal density gradient, in experiments **A2** and **B2**, gravitational circulation was not present, with v_g staying lower than ± 0.02 m s^{-1}, except for a small increase during weak tidal currents ($v_{bE(max)} < 0.3$ m s^{-1}).

5.5.2 Wind effects on the gravitational circulation

Wind stress at the estuary surface can affect the estuarine stratification and gravitational circulation in in number of ways. Turbulent mixing generated by wind stress directly on the surface can affect the vertical structure and density-driven flow of the estuary similarly to the tide-induced mixing. As well as the direct effects of mixing, local or remote wind can promote sub-tidal water exchange (Wong and Valle-Levinson, 2002). Local wind can cause fluctuations of currents and sea level (Janzen and Wong, 2002), while disturbances associated with remote wind on the adjacent coastal region may affect the barotropic and baroclinic balance in the estuary (Ou et al., 1981).

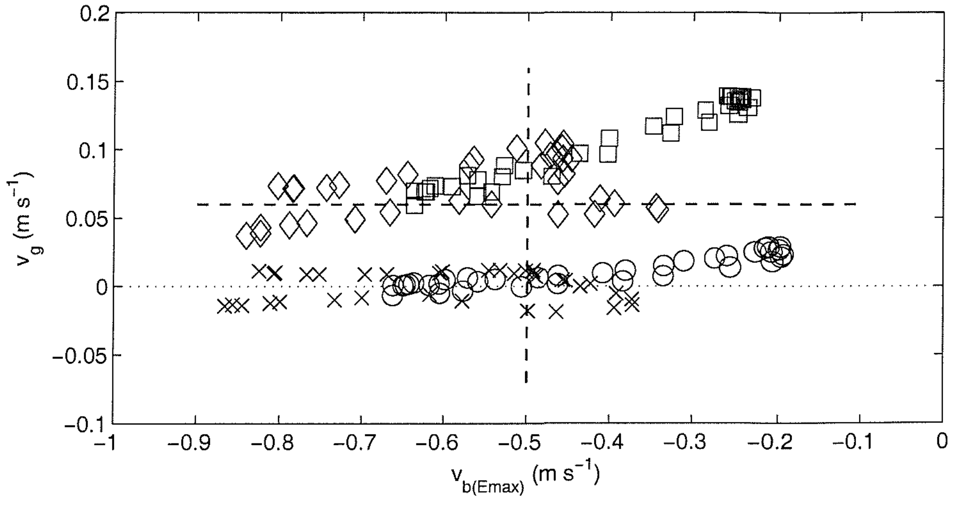

Figure 5.15: **Mean shear velocity v_g plotted against the maximum ebb bottom velocity $v_{b\,(Emax)}$, averaged over the semi-diurnal tidal cycles for the no wind model experiments. Squares represent the high λ - weak neap (A1), circles low λ - weak neap (A2) , diamonds high λ - strong neap (B1), crosses low λ - strong neap (B2).**

Contrary to the predictable tidal currents, winds are difficult to forecast more than a few days in advance, and are often highly variable in direction, speed and duration. This leads to a large variety of different interactions between wind and tidal conditions. It is clearly not possible to model all potential scenarios, so the experiments with the numerical model described here are restricted to the effects of the wind-induced mixing on a well-established event of gravitational circulation during weak neap tide. The no-wind experiment **A1** described in the Table 5.1 is used as a basis for running the model with the desired wind variability.

The necessity of using the zero mean non-tidal flow condition in the model (see section 5.3.2) will have an effect on the way the a surface wind stress is able to transport water within the model. However this simple 1-D model needs the imposition of the zero mean-flow to run. This limitation on the wind-driven currents certainly affects the model output but in a similar way for all wind-related experiments allowing comparisons between their results.

In order to test the influence of the direction and the persistence of the wind on the density-driven velocity profile a constant wind stress of 0.18 $\mathrm{N\,m^{-2}}$ was applied during nine different time windows: 1, 3, 6, 9, 12, 15, 18, 21 and 24 hours. These experiments are numbered from **x1** to **x9** respectively, where **x** represents the indicative letter for the three different directions: (**C**) landward wind, or wind to the SE; (**D**) seaward wind, which corresponds to wind to the NW; and (**E**) transverse wind, perpendicular to the estuary either to SW or NE. Wind started on the same day for all experiments, day 13, at neap tide and the $\tau_W = 0.18\ \mathrm{N\,m^{-2}}$ corresponds to the observed critical wind speed of 8 $\mathrm{m\,s^{-1}}$ (see section 3.3.2).

Bottom-surface velocity difference $< v_b > - < v_s >$ was obtained from the profile of the model output of tidal currents averaged over 25 hours since the wind had started. By plotting this shear for all nine experiments with landward wind this difference decreases almost linearly from 0.13 $\mathrm{m\,s^{-1}}$ for the 1 hour wind (experiment **C1**) to -0.004 $\mathrm{m\,s^{-1}}$ for the 24 hour (experiment **C9**) wind (Fig. 5.16a). The decrease of the bottom-surface shear is caused by the reduction of the surface current from -0.08 $\mathrm{m\,s^{-1}}$ for **C1** (Fig. 5.16b) to -0.04 $\mathrm{m\,s^{-1}}$ for **C5** (12 h wind - Fig. 5.16c) and to flow in the opposite direction into the estuary for **C9**, with $< v_s >= 0.01\ \mathrm{m\,s^{-1}}$ (Fig. 5.16d). Contrasting to the strong action of the wind stress on the shallower cell, at the deeper two-third of the water column the non-tidal velocities still exhibit gravitational circulation though slightly reduced (decrease of 0.03 $\mathrm{m\,s^{-1}}$ from **C1** to **C5**). As onshore wind stress acts for longer periods vertical convective instability develops leading to negative *Ri*. Greater 25-h mean depth-integrated N_z is present in **C9** ($= 10^{-2}\ \mathrm{m^2\,s^{-1}}$) compared to **C5** ($= 3 \times 10^{-3}\ \mathrm{m^2\,s^{-1}}$) due to the reduction of the Richardson number.

The seaward winds have similar effects to the landward on the net flow although in the opposite direction. Bottom-surface non-tidal shear increases from 0.15 $\mathrm{m\,s^{-1}}$ for the 1-h wind **D1** experiment to 0.21 $\mathrm{m\,s^{-1}}$ for the 24-h wind **D9** experiment (Fig. 5.17a), responding to longer wind duration. This variation is caused mainly by the wind action on moving surface waters out of the estuary. The 25-h mean surface current $< v_s >$ strengthens according to the increase of the wind duration, from -0.09 $\mathrm{m\,s^{-1}}$ in the 1 hours scenario (**D1**) to -0.11 $\mathrm{m\,s^{-1}}$ in the 12 hours (**D5**) to -0.13 $\mathrm{m\,s^{-1}}$ in the 24 hours (**D9**). However below the most surface cell the profile of the non-tidal velocities change

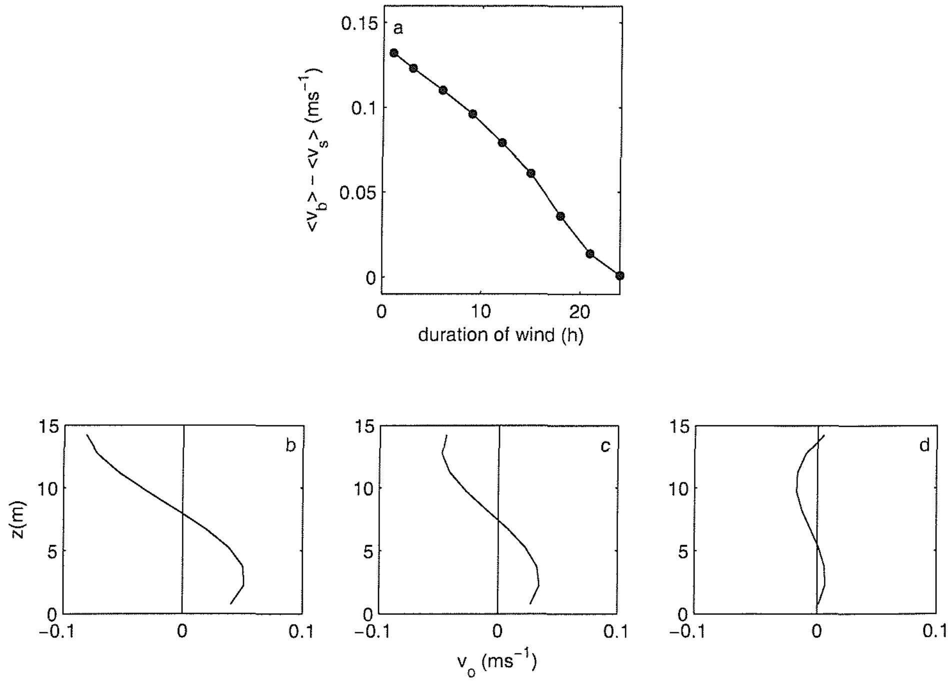

Figure 5.16: **Effects of a landward wind of different duration on the modelled gravitational circulation, with (a) the bottom-surface shear of the 25-h averaged velocity $< v_b > - < v_s >$ for different duration of wind (1 to 24 hours), and vertical profiles of the 25-h mean velocity $< v >$ for wind of (b) 1 hour (experiment C1), (c) 12 hour (experiment C5) and (d) 24 hour duration (experiment C9). The dots in (a) show the time of duration of the wind for each numerical experiment with wind stress of 0.18 $\mathrm{N\,m^{-2}}$. Depths are in metres above the bottom and negative velocities represent out of the estuary flow in (b,c,d).**

less than 5×10^{-3} $\mathrm{m\,s^{-1}}$ for every 12 additional hour of wind (from **D1** to **D5** and from **D5** to **D9** - Fig. 5.17b,c,d). The 25-h vertically integrated N_z remains lower than 4×10^{-3} $\mathrm{m^2\,s^{-1}}$ for all seaward wind experiments. Neither stratification or Richardson number change, except at the surface cell, which may indicate the limitation of the TCS in allowing an increase of stratification due to the high background N_z.

The non-tidal bottom-surface velocity difference decreases for winds perpendicular to the estuary (experiments **E1** to **E9**)(Fig. 5.18). The non-tidal shear for the nine different persistence periods shows a steeper reduction for winds between 6 and 18 hours, with $< v_b > - < v_s >$ decreasing from 0.13 to 0.08 $\mathrm{m\,s^{-1}}$ for this 12 hour increase. For wind duration between 1 and 6 the wind stress causes a variation in the non-tidal shear of

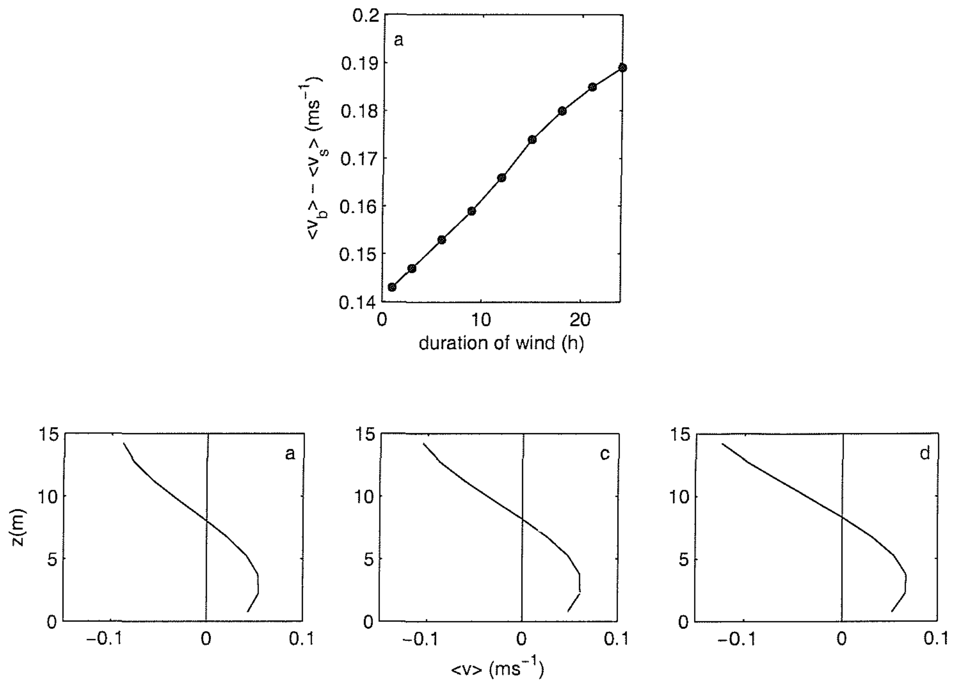

Figure 5.17: **Same as Fig. 5.16 for experiments D1 to D9, with steady seaward wind of τ_w = 0.18 N m^{-2}.**

less than 2×10^{-3} m s^{-1} for each hour of wind added (Fig. 5.18a). It also seems that for wind duration longer than 18 hours the effects of wind-induced mixing on reducing the non-tidal velocity tends to a limit of the wind duration, when gravitational circulation does not respond to longer winds.

Transverse winds have little effect on the bottom 25-h mean velocity. $< v_b >$ varies from 0.04 m s^{-1} in **E1** to 0.03 m s^{-1} in **E5** and to 0.02 m s^{-1} in **E9**. $< v_s >$ varies from -0.08 m s^{-1} in **E1** to -0.06 m s^{-1} in **E5** and -0.04 m s^{-1} in **E9** (Fig. 5.18b,c,d). This difference on the vertical distribution of the wind-induced shear can be confirmed by a progressively higher values at the surface cell as the period of wind increases. Instead of the stronger changes in the surface cell associated with longer exposure to parallel winds, the non-tidal velocity profiles have a more homogeneous variation for the transverse wind experiments. This lower surface variability is caused by the absence of the strong wind-induced water movement into or out of the estuary associated to parallel winds to the estuary. Thus the experiments with transverse winds reflect the estuary response to an

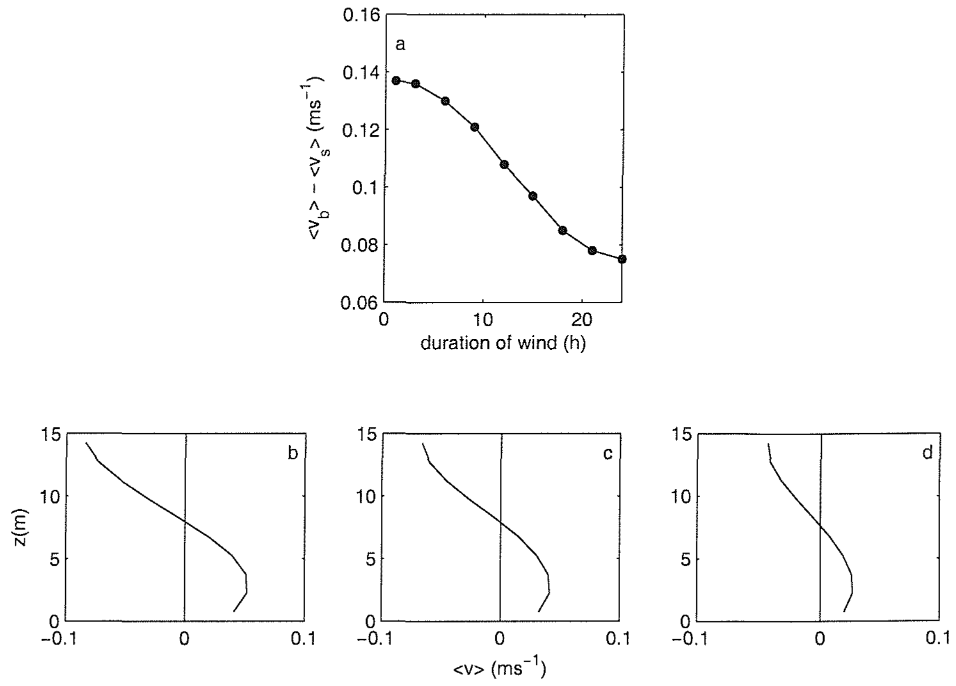

Figure 5.18: **Same as Fig. 5.16 for experiments E1 to E9, with steady transverse wind of τ_w = 0.18 N m^{-2}.**

addition of mixing energy at the surface alone, without any additional effects of wind-driven currents parallel to the horizontal density gradient.

The increase on the turbulent mixing due to longer duration of wind action is confirmed by the increase of the vertically averaged 25-h mean N_z from the background value of 2.5×10^{-3} m^2 s^{-1} for **A1** to 10^{-2} m^2 s^{-1} for **E1**, and to 2×10^{-2} m^2 s^{-1} for **E9**.

5.6 Discussion

The 1-D hydrodynamical model presented in this chapter was partially successful in reproducing the main fluctuations of the mixing processes in Southampton Water. The output of the eddy viscosity at the bottom cell follows both the spring-neap and the semi-diurnal tidal characteristics, allowing the investigation of the modulation of the gravitational circulation on these time scales.

For the longitudinal density gradient of 2.5 × 10^{-4} kg m^{-4} and typical weak neap currents (experiment **A1**) the long-term variability of the fluctuation of the tidally-induced mixing resulted in a spring-neap modulation of the gravitational circulation. The larger bed friction at the spring tide generates enough mixing to affect the full development of the gravitational flow. With the weakening of the tidal currents towards the neap tide, gravitational circulation increases towards its maximum value, that is limited by the background N_z. This feature remains until the tidal currents strengthen towards the following spring tide. Quantitatively, the modelled non-tidal flows were higher than these observed throughout the whole period, particularly at spring tide. Typical bottom-surface difference of the observed/modelled gravitational currents for weak neap tide was 0.15/0.18 m s^{-1}, while for spring tide was 0/0.07 m s^{-1}.

For the lower longitudinal density gradient of 1 × 10^{-4} kg m^{-4} the modelled gravitational circulation was reduced by a factor of more than three. The much simpler formulation of the density-driven flow described by Hansen and Rattray (1965) indicates a linear relation between gravitational circulation and longitudinal density gradient. This results in a reduction of the mean velocity profile of the same order of magnitude of the TCS model applied here. As noted above in the data/model comparison at the spring tide of the experiment **A1**, the model indicated the presence of a steady mean circulation while the observed surface and bottom gravitational flow varied around zero (see Fig. 3.6b). It seems that the model developed a background signal of the gravitational circulation, which is possibly related to the TCS limitations to treat strong stratification-strong mixing conditions. The gravitational flow was reduced to zero when TCS was removed from the model and N_z assumed the spring tide mean value of 10^{-2} $m^2 s^{-1}$. As the model is very sensitive to stratification, the frictional coupling between the cells in the water column is rapidly reduced in response to an increase of stability (Sharples and Simpson, 1995).

The effects of the alternate stronger tidal currents at neap tides, following the monthly variability due to the interaction of the semi-diurnal harmonics M_2 and N_2, were also seen in the model results. In this scenario (experiment **B1**) there was no significant neap-spring difference in the gravitational circulation. This supports the inference from the observations that the stronger neap tides still supplied enough mixing energy to prevent increased gravitational flows.

Semi-diurnal variability of the tidal currents in Southampton Water allows investigation of the three different periods of low velocity with duration ranging from 30 minutes to 3 hours. The modelled bottom N_z responds to this tidal current variability in a few minutes. This very rapid shift in the turbulent mixing conditions caused a semi-diurnal modulation of the gravitational circulation, with an increase during the low current periods and a reduction associated to the stronger currents at the ebb, first and second floods. Semi-diurnal modulation was not observed at the weaker neap currents when N_z reached the constant background value (see Fig. 5.14). Effects of the semi-diurnal tidal currents on stratification was found by Sharples and Simpson (1995)

Although the modelled density output reflected the variability of the tidal currents, the absolute values of the bottom-surface density difference were one order of magnitude lower than observations. Using a level 2 TCS, Sharples and Simpson (1995) found that the variability of the stratification in the Liverpool Bay was strongly controlled by tidal stirring. A possible cause for this difference is that in the shallower Southampton Water the impact of the depth on the strength of the gravitational circulation is reduced (Simpson et al., 1990). These authors have shown in the equation 3 that the density-driven flow is proportional to h^5.

The modelled semi-diurnal modulation of the gravitational circulation does not agree with data. Observed gravitational circulation showed no short term modulation driven by tidal mixing. The lack of tidally-induced fluctuation of the observed gravitational circulation seemed to be related to the need of a longer period than few hours for turbulent mixing to overcome buoyancy and affect the mean flow.

The observations suggested that winds may be important both as a source of mixing, and as a source of buoyancy when wind stress was parallel to the horizontal density gradient. Model results have clearly shown the effects of different wind orientations. Model results indicated that parallel winds act in favor or in opposition to the surface seaward flow characteristic to the gravitational circulation. This water movement directed by winds is in agreement with the results obtained by Zheng and Weisberg (2004) on their 3-D model. However the model failed to simulate the total strength of the wind-induced mixing, as data showed a complete absence of the gravitational circulation when $\tau_W = 0.18\ \mathrm{N\,m^{-2}}$; i.e. the model wind stress. This failure is likely to be caused by the limitation of TCS in reproducing the vertical mixing in shallow partially-mixed estuaries with permanent stratification.

The effectiveness of the wind in mixing can be investigated assuming that, except the known tidal effect, wind mixing is the only force that causes changes in the gravitational circulation in the **E** series of experiments, as the **C** and **D** series (parallel wind) have the water movement in the surface cells largely influenced by wind. Thus the reduction of the gravitational flow showed in the transverse wind scenario may represent the effectiveness of the wind stress in the altering the circulation. By comparing the **E** scenarios with observations, the modelled downward transfer of turbulent momentum caused by wind stress accounts for half of the observed reduction of the gravitational circulation caused by parallel winds.

Seaward wind stress (experiments **C**) adds mixing by substantially introducing more vertical shear. It also aids the surface gravitational circulation outflow by moving water leeward. This less dense water flow causes an increase of the stratification and hinders the wind-driven mixing. Landward winds (experiments **D**) add mixing as well, and bring convective mixing at the surface, as the surface outflow is first slowed and then reversed. Thus these onshore winds prevent stratification by both mixing, and by a sort of reverse wind-driven straining.

Other wind-driven physical mechanisms which are not included in the model, such as local-generated waves (Araújo et al., 2001), wind-driven barotropic gradient (Janzen and Wong, 2002), lateral recirculation cells and coastal surges (Valle-Levinson et al., 2002), may also bring additional mixing.

Chapter 6

Conclusions and summary

The variability of the bi-directional mean flow consistent with the gravitational circulation was the main goal of this project. The hypothesis of different mixing processes modulating the gravitational circulation was tested by analysing 268 days of moored ADCP data and results from a simple 1-D mixing model. The unusual tide in Southampton Water characterises this partially mixed estuary as an ideal natural water body for this project. In addition to tidal mixing, the effects of non-tidal mechanisms on the modulation of the gravitational circulation were investigated. The main findings of this study are:

The spring-neap modulation

- The gravitational circulation was observed to vary on the spring-neap time scale in response to changes in tidal mixing. In particular, the gravitational flow increased when near-bed ebb tide velocities were below 0.4 $\mathrm{m\,s^{-1}}$. At the same time, the bottom-surface stratification was also modulated, typically between 2 - 3 $\mathrm{kg\,m^{-3}}$ at spring tides and 5 - 6 $\mathrm{kg\,m^{-3}}$ during weak neap tides. These results are consistent with the turbulent mixing effects on the gravitational flow observed by Linden and Simpson (1986) in their illustrative tank experiments.
- Results from the numerical experiments also showed the spring-neap modu-

lation of gravitational circulation and stratification, and were in quantitative agreement with the upper limit of near-bed tidal velocity required for a response in the gravitational circulation. However, the model overestimated the observed gravitational velocities and significantly underestimated stratification. A weak signal of gravitational circulation seems to persist as a background value. This result suggests that TCS does not work well in simulating gravitational flow in shallow partially mixed estuaries. The choice of a large background N_z is necessary to keep the model stable and to make the study of the mixing variability on the gravitational circulation possible, although some counter-effects are inevitable. Limiting the feedback between mixing and stratification might alter the responses of either (or both) gravitational circulation or stratification. The disagreement between model output and field observations may indicate the importance of mixing processes other than those explored by the model, such as internal mixing.

- Observations suggested that, approaching weak neap tides, stratification increased ahead of the onset of the gravitational circulation. Increasing stability aids the development of gravitational circulation. Model results did not show this behaviour though.

The semi-diurnal modulation

- In spite of the noticed irregular short term variability of the non-tidal velocity, no clear modulation of the gravitational circulation was observed following the semi-diurnal fluctuation of the tidal mixing. Contrary to the observations of Stacey et al. (2001), enhanced gravitational circulation was not associated with slack waters.

- Lack of response at low mixing periods could be the result of the possible requirement of water column stability as a precursor to increased density-driven flow. Field observations indicated that the duration of slack water (up to 2 hours) is not long enough for stratification to respond. For a given spring tide condition, stratification is affected by the stronger tidal mixing and may not be able to develop fast enough within the slack water periods.

The sequence of low mixing - stratification - inhibited mixing - gravitational circulation may require a longer time (one or two days) to operate than the semi-diurnal tide permits. At weak neap tides tidal currents are not strong enough to reduce the gravitational flow and no modulation could be seen either. This finding is consistent with the concept of the stratification precondition to enhance gravitational flow. Considering the results of Sharples and Simpson (1995), another possibility for the lack of semi-diurnal modulation is the limited depth of the estuary (10 - 18 m) compared to the depth of Liverpool Bay (40 m); Simpson et al. (1990) have shown that the strength of the impact of gravitational circulation is proportional to h^5. Another possibility is that the slack water signal may appear to the analysis as part of the shallow water tidal constituents in Southampton Water.

The non-tidal modulation

- Results showed that wind direction, intensity and persistence are important in determining wether or not gravitational circulation will be affected by wind stress. Along-estuary winds can exert locally-generated mixing more efficiently due to the longer longitudinal fetch and are able to move surface water leeward, which might enhance (offshore wind) or hinder (onshore wind) the surface gravitational flow. The critical wind intensity for those parallel winds was found to be approximately 8 $\mathrm{m\,s^{-1}}$ ($\tau_W = 0.18\ \mathrm{N\,m^{-2}}$), with no event of gravitational circulation seen even during the weakest neap tide when wind speeds exceeded this. While observed winds from NE-SW did not affect significantly the gravitational circulation, the model showed that persistent cross-estuary winds reduced the non-tidal velocity by half. Model results showed that the longer the wind persisted the more effective it was in altering the mean circulation. It seems that changes in the gravitational circulation caused by wind occur in a few hours, while those caused by bottom tidal friction take an order of tens of hours. Two possible causes for this quicker response to wind mixing can be drawn : (1) the shorter periods of high tidally-induced mixing (peak of tidal currents are shorter then 30 minutes) compared to strong winds (few hours, although highly variable); and (2) the surface water movement caused by wind stress, which may locally alter the longitudinal density gradient either strengthening or weakening the density-driven flow.

The long term modulation

- Low river discharge during the summer deployment caused a reduction of the longitudinal density gradient and was the reason for the absence of a well-defined, bi-directional, density-driven flow. Model results of the gravitational circulation for different density gradients agreed with these observations. Field observations indicate that the effects of rainfall variability on the net flow occur in both intra- and inter-annual time scales. In this case, the North Atlantic Oscillation - N.A.O., which affects rainfall in North Europe, will have an effect on the mean flow of the estuary.

The establishment of the gravitational circulation in this partially mixed estuary depends on having all the processes favouring the formation of the density-driven flow. Fluctuations of these processes determine the temporal variability of gravitational circulation in Southampton Water (Fig. 6.1).

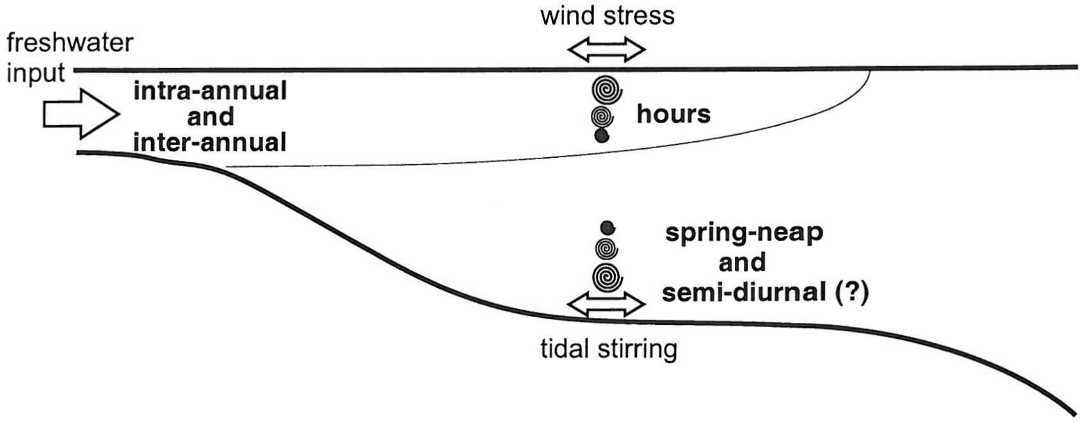

Figure 6.1: **Schematic summary of the temporal variability of the gravitational circulation in Southampton Water, indicating the mechanisms and the respective time scales of the modulation.**

Modulation of the net circulation controls the time scales of the transport of nutrients, organisms, sediments and pollutants through the water into and out of the estuary. The results discussed in this project will be useful for further studies on the ecology and environmental management of estuaries.

6.1 Further work

In this project data from a single sampling station at mid estuary was used. Any spatial variability of the longitudinal density gradient is critical for the extrapolation of the findings described here to the whole system. Some insights into this issue can be acquired by applying the model used here to conditions of tide and vertical and horizontal density gradients observed in the upper and lower estuary.

Some of the results shown in this study suggested that the onset of gravitational circulation was preceded by an increase of stratification. Although these results could not be conclusive, it seems that the increase of stratification may restrain mixing and allow the horizontal density gradient to drive the buoyancy flow. Further intensive field studies should be done during low wind, weak neap tide, when gravitational flow is more likely to occur. In addition to the measurements showed in this thesis, measurements of turbulent parameters and both vertical and horizontal density structure would lead to a better understanding of the mechanisms involved in the variability of the gravitational circulation.

The intra-annual and inter-annual fluctuations of the horizontal density gradient is an interesting approach to be taken within possible scenarios of climate change to be tested in the model. Positive N.A.O. (North Atlantic Oscillation) index results in wetter and warmer winters in northern Europe. Phases of the N.A.O. have been consistently more positive recently leading to greater rainfall during winter in the United Kingdom (Hurrel et al., 2003). This increase/decrease of rainfall on the water basin may cause a stronger/weaker density gradient, altering the gravitational flows.

Bibliography

M. Araújo, D. Dartus, P. Maurel, and L. Masbernat. Langmuir circulations and enhanced turbulence beneath wind-wave. *Ocean Modelling*, 3:109–126, 2001.

P. G. Baines and H. Mitsudera. On the mechanism of shear flow instabilities. *Journal of Fluid Mechanics*, 276:327–342, 1994.

D. Bourgault and D. E. Kelley. Wave-induced boundary mixing in a partially mixed estuary. *Journal of Marine Research*, 61:553–576, 2003.

H. Burchard and H. Baumert. The formation of estuarine turbidity maxima due to density effects in the salt wedge. A hydrodynamic process study. *Journal of Physical Oceanography*, 28(2):309–321, 1998.

H. Burchard, K. Bolding, T. P. Rippeth, A. Stips, J. H. Simpson, and J. Sundermann. Microstructure of turbulence in the northern north sea: A comparative study of observations and model simulations. *Journal of Sea Research*, 47:223–238, 2002.

D. Chen, S. G. Horrigan, and D.-P. Wang. The late summer vertical nutrient mixing in Long Island Sound. *Journal of Marine Research*, 46:753–770, 1988.

A. G. Davies. A model of the vertical structure of the wave and current bottom boundary layer. In A. M. Davies, editor, *Modelling Marine System*, pages 263–297. CRC Press, 1990.

R. K. Dewey, W. R. Crawford, A. E. Gargett, and N. S. Oakey. A microstructure instrument for profiling oceanic turbulence in coastal bottom boundary layers. *Journal of Atmospheric and Ocean Technology*, 4:288–297, 1987.

E. A. Driscoll, G. S. Janowitz, and L. J. Pietrafesa. Baroclinic driven estuarine flow: a perturbation approach. *Journal of Geophysical Research*, 103(12):27893–27903, 1998.

K. R. Dyer. Tidally generated estuarine mixing processes. In B. Kjerfve, editor, *Hydrodynamics of Estuary*, volume 1, pages 41–57. CRC Press, Boca Raton, 1988.

W. J. Emery and R. E. Thomson. *Data Analysis Methods in Physical Oceanography*. Pergamon, 634 p., 1997.

D. M. Farmer and J. D. Smith. Tidal interaction of stratified flow with a sill in Knight Inlet. *Deep-Sea Research*, 27:239–254, 1980.

N. Fisher, J. Simpson, and M. Howarth. Turbulent dissipation in the Rhine ROFI forced by tidal flow and wind stress. *Journal of Sea Research*, 48:249–258, 2002.

B. Galperin, L. H. Kantha, S. Hassid, and A. Rosati. A quasi-equilibrium turbulent energy model for geophysical flows. *Journal of the Atmospheric Sciences*, 45:55–62, 1988.

W. R. Geyer and J. D. Smith. Shear instability in a highly stratified estuary. *Journal of Physical Oceanography*, 17:1668–1679, 1987.

D. M. Goodrich, W. C. Boicourt, P. Hamilton, and D. W. Pritchard. Wind-induced destratification in Chesapeake Bay. *Journal of Physical Oceanography*, 17:2232–2240, 1987.

D. V. Hansen and M. Rattray. Gravitational circulation in straits and estuaries. *Journal of Marine Research*, 23:104–122, 1965.

J. W. Hurrel, Y. Kushnir, G. Ottersen, and M. Visbeck. An overview of the North Atlantic Oscillation. In J. W. Hurrel, Y. Kushnir, G. Ottersen, and M. Visbeck, editors, *The North Atlantic Oscillation: climate significance and environmental impact*, pages 1–36. American Geopyhsical Union, 2003.

C. D. Janzen and K.-C. Wong. Wind-forced dynamics at the estuary-shelf interface of a large coastal plain estuary. *Journal of Geophysical Research*, 107:3138, doi:10.1029/2001JC000959, 2002.

D. A. Jay. Internal asymmetry and anharmonicity in estuarine flows. In B. B. Parker, editor, *Tidal Hydrodynamics*, pages 521–543. John Wiley and Sons, 1991.

D. A. Jay and E. P. Flinchen. A comparison of methods for analysis of tidal records containing multi-scale non-tidal backgroud energy. *Continental Shelf Research*, 19: 1695–1732, 1999.

D. A. Jay and J. D. Musiak. Internal tidal asymetry in channel flows: origins and consequences. In C. Pattriaratchi, editor, *Mixing in estuaries and coastal seas*, volume 50 of *Coastal and estuarine studies*, pages 211–249. American Geopyhsical Union, Washington, 1996.

S. A. Kitaigorodskii. Methodological grounds of describing the aerodynamic roughness parameter of the sea surface. *Izvestiya Atmospheric and Oceanic Physics*, 39:203–207, 2003.

C. G. Koop and F. K. Browand. Instability and turbulence in a stratified fluid with shear. *Journal of Fluid Mechanics*, 93:135–159, 1979.

J. v. d. Kreeke and K. Robaczewska. Effects of wind on the vertical circulation and stratification in the Volkerak estuary. *Netherlands Journal of Sea Research*, 23(3): 239–253, 1989.

M. T. Landahl and E. Mollo-Christensen. *Turbulence and Random Processes in Fluid Mechanics.* Cambridge University Press, 154 p., 1986.

J. L. Largier. The internal tide over the shelf inshore of the Cape Point Valley, South Africa. *Journal of Geophysical Research*, 99(5):10023–10034, 1994.

M. Lesieur. *La Turbulence.* Presses Universitaires de Grenoble, 262 p., 1994.

R. Lewis. *Dispersion in Estuaries and Coastal Waters.* John Wiley and Sons, 312 p., 1997.

C. Li and J. O'Donnel. Tidally driven residual circulation in shallow estuaries with lateral depth variation. *Journal of Geophysical Research*, 102:27915–27929, 1997.

P. F. Linden and J. E. Simpson. Gravity-driven flows in a turbulent fluid. *Journal of Fluid Mechanics*, 172:481–497, 1986.

S. MacIntyre, K. Flynn, R. Jellison, and J. Romero. Boundary mixing and nutrient fluxes in Mono Lake, California. *Limnology and Oceanography*, 44:512–529, 1999.

L. Mahrt, D. Vickers, P. Frederickson, K. Davidson, and A.-S. Smedman. Sea-surface aerodynamic roughness. *Journal of Geophysical Research*, 108:3171, 2003.

D. Masson and P. F. Cummins. Fortnightly modulation of the estuarine circulation in Juan de Fuca Strait. *Journal of Marine Research*, 58:439–463, 2000.

T. Maxworthy. A note on the internal solitary waves produced by tidal flow over a three-dimensional ridge. *Journal of Geophysical Research*, 84:338–346, 1979.

G. L. Mellor and T. Yamada. A hierarchy of turbulence closure models for planetary boundary layers. *Journal of Atmospheric Science*, 31:1791–1806, 1974.

F. J. Millero and A. Poisson. International one-atmosphere equation of state of seawater. *Deep-Sea Research*, 28A:625–629, 1981.

H. O. Mofjeld and J. W. Lavelle. Setting the length scale in a second-order closure model of the unstratified bottom layer. *Journal of Physical Oceanography*, 14:833–839, 1984.

A. Munchow and R. W. Garvine. Dynamical properties of a buoyancy-driven coastal current. *Journal of Geophysical Research*, 98:20063–20077, 1993.

H. M. Nepf and W. R. Geyer. Intratidal variations in stratification and mixing in the Hudson estuary. *Journal of Geophysical Research*, 101(5):12079–12086, 1996.

A. L. New. Internal tidal mixing in the Bay of Biscay. *Deep-Sea Research*, 35(5):691–709, 1988.

A. L. New and K. R. Dyer. Internal waves and mixing in stratified estuarine flows. In J. Dronkers and W. v. Leussen, editors, *Physical process in estuaries*, pages 239–254. Springer-Verlag, Berlin, 1988.

A. L. New, K. R. Dyer, and R. E. Lewis. Predictions of the generation and propagation of internal waves and mixing in a partially stratified estuary. *Estuarine, Coastal and Shelf Science*, 22:199–214, 1986.

A. L. New, K. R. Dyer, and R. E. Lewis. Internal waves and intense mixing periods in a partially stratified estuary. *Estuarine, Coastal and Shelf Science*, 24:15–33, 1987.

R. A. Nunes and G. W. Lennon. Episodic stratification and gravity currents in a marine environment of modulated turbulence. *Journal of Geophysical Research*, 92(5):5465–5480, 1987.

R. A. Nunes-Vaz and J. H. Simpson. Turbulence closure modeling of estuarine stratification. *Journal of Geophysical Research*, 99(8):16143–16160, 1994.

R. A. Nunes-Vaz, G. W. Lennon, and J. R. d. S. Samarasinghe. The negative role of turbulence in estuarine mass transport. *Estuarine, Coastal and Shelf Science*, 28: 361–377, 1989.

C. B. Officer. *Physical Oceanography of Estuaries (and Associated Coastal Waters)*. John Wiley and Sons, 465 p., 1976.

H. W. Ou, R. C. Beardsley, D. Mayer, W. C. Boicourt, and B. Butman. An analysis of subtidal current fluctuations in the Middle Atlantic Bight. *Journal of Physical Oceanography*, 11:1383–1392, 1981.

B. B. Parker. The relative importance of the various nonlinear mechanisms in a wide range of tidal interactions. In B. B. Parker, editor, *Tidal Hydrodynamics*, pages 237–268. John Wiley and Sons, 1991.

J. Pedlosky. *Geophysical Fluid Dynamics*. Spring-Verlag, 710 p., 1987.

H. Peters. Spatial and temporal variability of turbulent mixing in an estuary. *Journal of Marine Research*, 57(6), 1999.

H. Peters. Observations of stratified turbulent mixing in an estuary: Neap-to-spring variations during high river flow. *Estuarine, Coastal and Shelf Science*, 45:69–88, 1997.

H. Peters and R. Bokhorst. Microstructure observations of turbulent mixing in a partially mixed estuary. Part I: Dissipation rate. *Journal of Physical Oceanography*, 30:1232–1244, 2000.

D. Prandle. Tides in estuaries and embayments. In B. B. Parker, editor, *Tidal Hydrodynamics*, pages 125–152. John Wiley and Sons., 1991.

D. W. Pritchard. The dynamic structure of a coastal plain estuary. *Journal of Marine Research*, 15:33–42, 1956.

D. W. Pritchard. Salinity distribution and circulation in the Chesapeake Bay estuary system. *Journal of Marine Research*, 11:106–123, 1952.

D. W. Pritchard. The equations of mass continuity and salt continuity in estuaries. *Journal of Marine Research*, 17:412–423, 1958.

D. T. Pugh. *Tides, Surges and Mean Sea-Level - a Handbook for Engineers and Scientists.* John Wiley and Sons, 472 p., 1987.

RDInstruments. *Broadband Acoustic Doppler Current Profiler.* Technical Manual, 1993.

J. Sharples. *Time Dependent Stratification in Regions of Large Horizontal Gradient.* Ph.D. Thesis, University College of North Wales, 137 pp., 1992.

J. Sharples and J. H. Simpson. Semi-diurnal and longer period stability cycles in the Liverpool Bay region of freshwater influence. *Continental Shelf Research*, 15:295–313, 1995.

J. Sharples and J. H. Simpson. Periodic frontogenesis in a region of freshwater influence. *Estuaries*, 16(1):74–82, 1993.

J. Sharples, J. H. Simpson, and J. M. Brubaker. Observations and modelling of periodic stratification in the upper York River estuary, Virginia. *Estuarine, Coastal and Shelf Science*, 38:301–312, 1994.

J. Sharples, C. M. Moore, and E. R. Abraham. Internal tide dissipation, mixing, and nitrate flux at the shelf edge of NE New Zealand. *Journal of Geophysical Research*, 106:14069–14081, 2001.

L. Shi and D. Purdie. M_2 tidally-induced water mass transport and water exchange in Southampton Water. In M. Collins and K. Ansell, editors, *Solent Science- a Review*, pages 199–204. Elsevier Science B.V., 2000.

J. H. Simpson and A. J. Souza. Semidiurnal switching of stratification in the region of freshwater influence of the Rhine. *Journal of Geophysical Research*, 100(4):7037–7044, 1995.

J. H. Simpson, J. Brown, J. Matthews, and G. Allen. Tidal straining, density currents, and stirring in the control of estuarine stratification. *Estuaries*, 13(2):125–132, 1990.

J. H. Simpson, W. G. Bos, F. Schirmer, A. J. Souza, T. P. Rippeth, S. E. Jones, and D. Hydes. Periodic stratification in the Rhine ROFI in the North Sea. *Oceanologica Acta*, 16(1):23–32, 1993.

J. H. Simpson, W. R. Crawford, T. P. Rippeth, A. R. Campbell, and J. V. S. Cheok. The vertical structure of turbulence dissipation in shelf seas. *Journal of Physical Oceanography*, 26:1579–1590, 1996.

S. D. Smith. Coefficients for sea surface wind stress, heat flux and wind profiles as a function of wind speed and temperature. *Journal of Geophysical Research*, 93:15467–15472, 1988.

M. T. Stacey, S. G. Monismith, and J. R. Burau. Observations of turbulence in a partially stratified estuary. *Journal of Physical Oceanography*, 29(8):1950–1970, 1999.

M. T. Stacey, J. R. Burau, and S. G. Monismith. Creation of residual flows in a partially stratified estuary. *Journal of Geophysical Research*, 106:17013–17037, 2001.

A. Stigebrandt. Vertical diffusion driven by internal waves in a sill fjord. *Journal of Physical Oceanography*, 6:486–495, 1976.

L. St.Laurent and C. Garrett. The role of internal tide in mixing the deep ocean. *Journal of Physical Oceanography*, 32:2882–2899, 2002.

S. A. Thorpe. Experiments on instability and turbulence in a stratified shear flow. *Journal of Fluid Mechanics*, 61:731–751, 1973.

R. J. Uncles and P. J. Radford. Seasonal and spring-neap tidal dependence of axial dispersion coefficients in the Severn - a wide, vertically mixed estuary. *Journal of Fluid Mechanics*, 98:703–723, 1980.

A. Valle-Levinson and K. M. M. Lwisa. The effects of channels and shoals on exchange between Chesapeake Bay and the adjacent ocean. *Journal of Geophysical Research*, 100:18551–18563, 1995.

A. Valle-Levinson and K. M. M. Lwisa. Bathymetric influences on the lower Chesapeake Bay hydrography. *Journal of Marine Systems*, 12:221–236, 1997.

A. Valle-Levinson, K.-C. Wong, and K. T. Bosley. Response to lower Chesapeake Bay to forcing from Hurricane Floyd. *Continental Shelf Research*, 22:1715–1729, 2002.

D. Wang and P. Müller. Effects of equatorial undercurrent shear on upper-ocean mixing and internal waves. *Journal of Physical Oceanography*, 32:1041–1057, 2002.

K.-C. Wong and R. W. Garvine. Observations of wind-induced, subtidal variability in the Delaware Estuary. *Journal of Geophysical Research*, 189:10589–10597, 1984.

K.-C. Wong and A. Valle-Levinson. On the relative importance of the remote and local wind effects on the subtidal exchange at the entrance to the Chesapeake Bay. *Journal of Marine Research*, 60:477–498, 2002.

L. Zheng and R. H. Weisberg. Tide, bouyancy, and wind-driven circulation of the Charlotte Harbour estuary : a model study. *Journal of Geophysical Research*, 109: doi:10.1029/2003JC001996, 2004.

M. Zhou. Influence of bottom stress on the two-layer flow induced by gravity currents in estuaries. *Estuarine, Coastal and Shelf Science*, 46(6):811–825, 1998.

Appendix A

Field work pictures

Pictures of the field work on board of the *R.V. Bill Conway* during deployments and recoveries of the mooring at the Cadland Buoy site in Southampton Water.

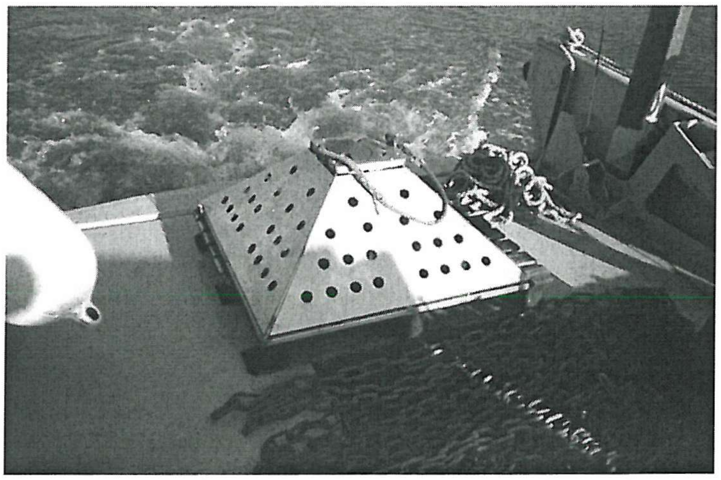

Figure A.1: **Pyramidal frame used for the moorings on the stern of the** ***R.V. Bill Conway*** **moments before the deployment. ADCP head can be seen on the top of the frame.**

Figure A.2: **Deployment of the frame from the stern of the boat.**

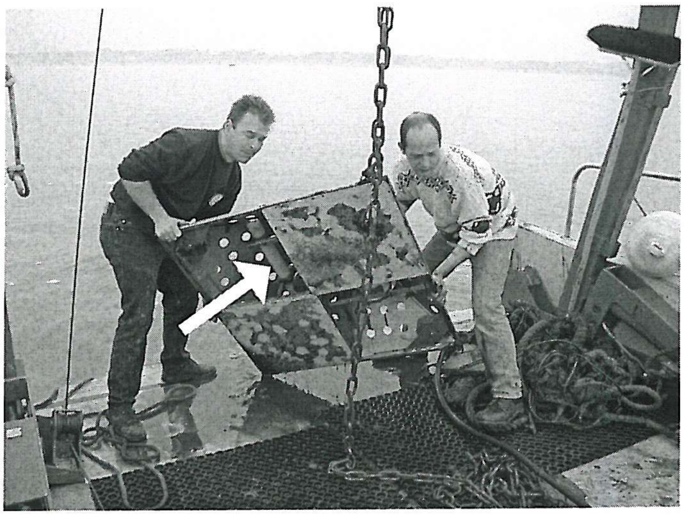

Figure A.3: **View of the bottom of the ADCP frame during recovering. White arrow shows the C-T logger attached in the frame.**

Figure A.4: **The surface C-T logger, showing the case, the chain and the weight.**

Figure A.5: **Attaching the surface C-T logger on the eye of the Cadland Buoy from the stern of the boat.**